JIMMA UNIVERSITY

JIMMA INSTITUTIVE TECHNOLOGY

FACULTY OF MECHANICAL ENGINEERING

Thesis Title: Numerical Modelling of Fatigue Behaviour for Rail-Wheel Rolling Contact Problem

A Thesis Submitted to Faculty of Mechanical Engineering, Jimma Institutive of Technology In partial Fulfillment of the Requirements for the Degree of Masters of Science in Mechanical Design

By

Goftila Gudeta

July, 2019

JIMMA UNIVERSITY

JIMMA INSTITUTIVE TECHNOLOGY

FACULTY OF MECHANICAL ENGINEERING

Thesis Title: Numerical Modelling of Fatigue Behaviour for Rail-Wheel Rolling Contact Problem

Prepared By: Goftila Gudeta

Main Advisor: Prof. Hirpa Lemu

Co-advisor: Dr.Ingr. Messay Alemu

Declaration

I hereby declare that the work which is presented in this thesis entitled "**Numerical Modelling of Fatigue Behaviour for Rail-Wheel Rolling Contact Problem**" is my original work, has not been presented for a degree in any other university; and that all sources of material used for this thesis have been duly acknowledged.

Goftila Gudeta _____ _____

Signature Date

This thesis has been submitted for examination with our approval.

Hirpa Lemu (Prof.) _____ _____

Principal Supervisor Signature Date

Messay Alemu (Dr.) _____ _____

Associate Supervisor Signature Date

Approval

Name: Goftila Gudeta

Degree Masters of Science

Title: Numerical Modelling of Fatigue Behaviour for Rail-Wheel Rolling Contact Problem

Examining Committee:

Chair:

Mr. Yohannis Dabasa _____

Principal Supervisor

Prof. Hirpa Lemu _____

University of Stavanger

Norway

Associate Supervisor

Dr. Messay Alemu _____

Jimma University

Ethiopia

External Examiner

Dr. _____ _____

Internal Supervisor

_____ _____

Date of Approval _____

ABSTRACT

The rail wheel fatigue failures are a serious problem that has been facing the international railway industries for more than two centuries. The railway industries have been spending millions of dollars annually for this problem. Rail wheel fatigue is rolling contact fatigue, which is caused by cyclic contact stress under rolling motion. Crack is formed due to this cyclic contact stress or small defect, and propagated to certain values at which fracture of rail wheel occurs. This fatigue crack propagation in railway wheels occurs under mixed mode (I, II and III) conditions. The aim of this study is to model and analysis fatigue behaviour of rail wheel rolling contact problem. In this study, both analytical and FE approaches have been used to predict the expected fatigue life of rail wheel. Extended finite element (X-FEM) in ABAQUS has been used for FE analysis. The results obtained from both approaches were compared and fatigue life of the rail wheel was predicted.

Three multiaxial fatigue models (S-J fatigue model, SWT fatigue model and F-S fatigue model) which can predict both the fatigue crack initiation life and fatigue cracking plane orientation are used to predict number of cycles to initiate the crack. All of these models are categorized under strain life approaches. The number of cycles for the crack initiation that obtained from the S-J, SWT and F-S fatigue models are 1×10^5, 5.78×10^5 and 1.32×10^5 respectively.

In order to determine the number of cycles to propagate the crack from the initial flaw to the critical crack length, the Liu mixed mode fatigue crack model was used. This model has the capability to consider non-proportionality required for a rail wheel fatigue crack modelling. The number of cycles for crack propagation which obtained from both analytical and FE results are 2052 and 2020 respectively. This number of cycles are the life of the wheel from the initiated crack grow up to the critical length of the crack. After the critical length, the crack will propagate rapidly.

Keywords: wheel-rail contact, Cyclic plasticity, Fatigue life, Crack initiation, Crack growth

ACKNOWLEDGEMENT

Above all I am extremely thankful and grateful to almighty God who has blessed me to be what I am today. Next, my genuine gratitude to my principal supervisor, Prof. Hirpa Lemu (University of Stavanger, Faculty of Science and Technology, Norway), for providing me the necessary guidance, continuous supervision, cooperation and motivation during this study. His supervision has made me a researcher and motivated me for future work. I feel extremely lucky for being a part of his research group. Then, I wish to express heartfelt thanks to my associate supervisor, Dr. Messay Alamu (Faculty of Mechanical Engineering, Jimma University), for his proficient supervision provided during my study. He played a huge role in the completion of this thesis. Working with him has been a great learning experience to me both professionally and personally.

I bestow my genuine thanks to others who supported me during this study for their ever-remarkable kind support and assistance. Finally, I would like to express my special thanks to my family, for their encouragement, patience, and endless support during this study.

CONTENTS

LIST OF FIGURES

LIST OF TABLES

NOMENCLATURES

ω	Angular velocity of the wheel
a_i	Backstress component tensor
$\boldsymbol{a}$	Backstress tensor
μ	Coefficient of friction
da/dN	Crack-growth rate
K_c	Critical stress intensity (fracture toughness)
n'	Cyclic hardening exponent
R	Cyclic loading stress ratio
$\boldsymbol{S}$	Deviatoric stress tensor
σ_{eff}	Effective stress
E*	Equivalent young's modulus
N_f	Fatigue life
A	Geometric coefficient of the Hertz contact theory
n	Hertz theory's constant
a_i	Initial crack size
c_{ij}	Kalker's creep and spin coefficients
ε_a	Load cycle local strain amplitude
ξ	Longitudinal creepage
a	Longitudinal semi-axis of contact patch
v_o	Longitudinal velocity of the vehicle
α_I	Material dependent additional hardening coefficient
σ_{ult}	Material ultimate tensile strength

σ_o	Material yield strength
$\sigma_{\max}$	Maximum axial stress
P_o	Maximum contact pressure
$\Delta\gamma_{\max}$	Maximum shear strain range
$\tau_{\max}$	Maximum shear stress
σ_{mean}	Mean stress
$\sigma_{\min}$	Minimum axial stress
K_{ic}	Mode I critical stress intensity (fracture toughness)
σ	Normal stress
$\Delta\sigma$	Normal stress range
C	Paris Law Crack-Growth Constant
m	Paris Law Crack-Growth Exponent
ε_p	Plastic Strain
$P(x,y)$	Pressure Distribution in the Contact Patch
R_{ij}	Radius of Curvature
r_o	Rolling radius of the wheel
$\tau_{f'}$	Shear fatigue strength coefficient
b_o	Shear fatigue strength exponent
G	Shear modulus
τ	Shear stress
τ_a	Shear stress amplitude
$\Delta\tau$	Shear stress range
M_z	Spin moment
b	Strain life constant
c	Strain life constant
K	Stress intensity factor
K_I	Stress intensity factor of mode I crack

K_{II}	Stress intensity factor of mode II crack
K_{III}	Stress intensity factor of mode III crack
ΔK	Stress intensity factor range
ΔK_{th}	Stress intensity factor threshold value for fatigue crack growth
F_y	Tangential force in lateral direction
F_x	Tangential force in longitudinal direction/ traction force
δ	Total displacement of two bodies
ε_t	Total strain
$\Delta\varepsilon_{von}$	Von Mises strain range
C	Walker crack-growth constant
γ	Walker material constant
F_n	Wheel load (normal force)
E	Young's modulus

CHAPTER 1

INTRODUCTION

In this chapter, a brief introduction of rail wheel fatigue failure problems is presented first. The statement of problem, objective, and scope and limitation of the study are explained afterwards. The thesis outline is provided at the end of this chapter.

1.1 Problem Background

Railway engineering plays a crucial role in solving transportation problems and to interconnect cities and countries. However, the train accidents have been facing many countries and making a train out of service and cause enormous injury, economic losses and a series of disasters. These accidents are due to train derailment, which is mainly caused by rail-wheel fatigue failure. Studying fatigue failure was originated from the railway's problems about 200 years ago. However, the main cause of failures in different industries, components, and railways is still fatigue.

On 3 June 1998, the Eschede train disaster occurred in Germany, when a high-speed train derailed and crashed into a road bridge, and then causing a carriage to strike the support of an over-bridge. Figure 1.1 shows the disaster caused by derailment of the train on June 1998 in Germany, in which 101 people died and around 100 were injured (Bayissa and Dhanasekar, 2011). The cause of the derailment was identified as fracture of wheel and the railroad company and the wheel manufacturer were accused.

On 17 October 2000, train accident occurred at Hatfield, north of London, (UK). The high-speed train carrying 182 passengers derailed when taking 1460 m radius curve, four were killed and 70 suffered injuries, four of them seriously. The cause of the derailment was identified as a fractured rail and then detailed inspections have been made of the tracks throughout the Britain. More than 200 sites where cracks were visible on the surface of the rails were identified (Alemi et al., 2017).

Figure 1.1 Eschede train disaster

On July 11, 2012 eastbound Norfolk Southern Railway Company (NS) freight train 186L809 derailed. The derailment occurred on the NS Lake Division and within the city limits of Columbus, Ohio. The probable cause of the derailment, as identified by the National Transportation Safety Board, was a broken rail that exhibited evidence of rolling contact fatigue (Moës et al., 1999). Several studies show that train accidents occurring in the world are due to the catastrophic failure of rail-wheel. The rail wheel contact parameters (materials, climatic conditions, load history, etc.) are commonly used in the analysis of the rail wheel failure. These parameters are the chief inputs of rail vehicle simulations, investigation of the rail-wheel deformations, determination of the service life, safety against the derailment (Özdemir, 2016).

Rail wheel damage mechanisms such as plastic deformation, fatigue and wear are significantly decrease the service life of rail-wheel and cause derailment of the train. Plastic deformation gradually occurs when the train wheel passes over the rail repeatedly. Plastic deformation in rail wheel is the non-reversible material disfigurement, which is mainly caused by high traction load. Recently, higher train speeds and axle loads have increased the contact stresses between the rail and wheel, thereby shifting the main rail-wheel damage mechanism from wear to fatigue. The rail-wheel fatigue problem is referred to as rolling contact fatigue, is caused by cyclic loading during the rolling conditions. During operational life, rail wheel typically experiences millions of load cycles from the passage of train wheels (Khoa Duy, 2015). When rail wheel is subjected to cyclic stresses, it may fail at stresses levels much lower than its yield stress. Fatigue failure has been progressively more violent especially in the components that are subjected to cyclic loading.

Despite its long history over many decades and the advances being made towards the safety of train and railway, catastrophic fatigue failures still occur frequently around the world due to rail-wheel fatigue. For instance, the annual number of broken rails was identified to be approximately 770 per year between 1969 and 2000 in United Kingdom (Sehitoglu and Jiang, 1992). In the Europian Union alone, 2 billion Euros per year is expensed for this problem (Yan and Fischer, 2000). For years 2004-2007, 44.7% of train accidents were caused by Wheel-set faults when compared to other mechanical components of the train (Sladkowski and Sitarz, 2005). Between 50 and 90 percent of all mechanical failures can be believed as a result of fatigue failure. Fatigue failure can occur without any obvious warning. Therefore, analyzing the rail wheel failure becomes a necessary.

1.2 Statement of the Problem

Fatigue has been a serious problem facing railway industries for a long period of time. It causes failure of rails, wheels, axles, and other parts of train. Failures of these components again lead to train derailments and cause enormous injury and economic problems.

Several researchers have proposed different methods in order to combat the challenges. However, the problem is still facing the world. Some have proposed, traditional failure criteria, which depends on maximum stress or strain energy density, but these can't justify failures of many structures occurred at stress levels lower than the ultimate strength of the material.

Ethiopian government is also expanding the railway transportation system for the country. Annually, Ethiopian Railway Corporation is also losing a million of birr for maintenance. Therefore, it is important to study the rail wheel fatigue failure, which was a challenging railway industry.

Therefore, the objective of this study is to address the problem of rail wheel fatigue failure by predicting the more precise fatigue life time of rail wheel. Numerical modelling and FE modelling will predict the more accurate expected fatigue life time of the rail wheel under high cyclic fatigue.

1.3 Objective of the Study

1.3.1 General objective

Investigating fatigue failure mechanism and predicting the total expected life of the rail-wheel using analytical and numerical approaches.

1.3.2 Specific objectives

- Numerical modelling of rail-wheel rolling contact problem
- Developing constitutive cyclic plasticity model for the rail wheel material
- Modelling crack initiation and propagation under rolling contact fatigue using analytical and FEM.

1.4 Scope and Limitation

This study focuses on predicting the fatigue life of rail wheel under cyclic load. This is can be achieved by using both analytical and FE approaches for modelling the fatigue behavior of rail wheel contact problem. For analytical approaches, different fatigue models from the previous studies are used. For numerical approaches, different computational tools are used. The XFEM in ABAQUS is used to simulate crack propagation and determine the effect of fatigue under cyclic load. Finally, the results of the analytical analysis and FE analysis will be compared. Due to lack of sufficient laboratory and expensive material cost, the results are not verified by experimental results.

1.5 Research Methodology

To address the above-mentioned objectives, analytical and numerical methods will be used since the rail-wheel contact is largely influenced by the contact stresses i.e. Hertzian contact theory for normal contact problem, analytical study of the Hertzian theory will be studied in order to be able to compare with numerical studies. In the same manner, Kalkers theory and Polach's theory are used for analytical study of tangential contact problem. The commercial CAE tool ABAQUS will be employed both for contact stress analysis and study of fatigue problem. In the last mentioned in particular, a 3D model will be developed in ABAQUS.

1.6 Structure of the Thesis

After this introduction section, the thesis is divided into 7 chapters. The content of each chapter is briefly outlined as follows.

Chapter 2 contains a review of relevant literature on rolling contact fatigue, where the theory of normal and tangential contact problem, rail-wheel failure mechanism, classification of fatigue failure and rolling contact fatigue mechanism are reviewed. This review highlights recent research and discovery on rail-wheel contact mechanism, and provides the theories and methods to analyze the rail wheel contact problems.

The detailed investigations of rail wheel contact problems are presented in chapter 3, where the rail wheel contact problems are discussed under two categories: normal and tangential contact problems. Hertzian contact theory is used to solve normal contact problem, and Kalker's linear theory and Polach's tangential theory are used to solve the tangential contact problem. Analytical methods are used to calculate contact area, pressure distribution, surface traction forces, etc.

Chapter 4 provides rail wheel cyclic plasticity modelling, in which material response to cyclic load are discussed. The constitutive material model, which provides a mathematical equation of the stress-strain response for the elasto-plastic deformation of the rail wheel material, are discussed in this chapter.

It is well known that fatigue life has two phases i,e. fatigue crack initiation and crack growth. Modelling techniques of these fatigue phases are discussed in the chapter 5. Among the available modelling techniques, the models used by Sehitoglu and co-workers (Sehitoglu and Jiang, 1992), Smith and co-workers (Smith et al., 1970), and Fatemi and Socie (Fatemi and Socie, 1988) are presented to predict the predict the number of cycles to crack initiation. Liu and Mahadevan models are used to model mixed mode fatigue crack growth.

Chapter 6 presents finite element modelling of rail wheel rolling contact problem, in which material properties, loading definitions, boundary conditions, meshing, etc. are described in detail. Finally, the results and discussion are presented in chapter 7, followed by conclusion and suggested future works that appear in chapter 8.

CHAPTER 2

LITERATURE SURVEY

In this chapter, overview of up to date theoretical, numerical and experimental investigations in rail-wheel contact mechanics is presented. An overview of rail wheel contact mechanism is first presented. A normal and tangential contact problem, rail-wheel damage mechanism, fatigue failure classification and rolling contact fatigue mechanism are discussed.

2.1 Rail-Wheel Contact Mechanics

2.1.1 General overview of contact mechanics

Contact mechanics deals with the deformation of solids which come into contact at the interface. This contact of two solid bodies can be either conformal (complete) contact or non-conformal (incomplete) contact (Barber, 2018). Conformal or complete contact occurs when the surface of the two un-deformed bodies in contact conforms (i.e. fit exactly or closely together), share a common shape and make a contact area size is large without requiring any deformation. Flat slider bearings and journal bearings are examples of conforming contact. Non-conformal or incomplete contact occurs when two bodies come into contact at one or more points, lines and their surfaces don't fit each other before the load is applied and contact area size is very small compared to the size of the bodies after the load is applied. The stresses are highly concentrated in the region close to the contact area. Ball bearings, rail-wheel and roller bearings are examples of non-conforming contact (Johnson, 1974).

2.1.2 Rolling contact problem

The rail-wheel contact problem can be categorized into two district sections, the normal contact problem and the tangential contact problem (Shackleton, 2009). In the normal contact problem;

the size, shape and position of the contact patch and the normal pressure distribution within the contact patch are determined from the rail-wheel geometry and normal load.

In the tangential contact problem; the longitudinal creep force F_x, lateral creep forces F_y, and the rotating creep moment M_z are determined. The shear stresses, which exists the between contacting surfaces, are also determined under tangential contact problem. The contact modelling of rail-wheel is described in depth next chapter.

In 1974, Johnson (Johnson, 1974) gives an overview of the classical contact problem and its implications. According to the author, the contact problem is greatly influenced by the material behaviour of the contacting bodies. The wheel-rail material behavior, which has to be considered directly within the contact problem, also influences the damage behavior of wheel and rail.

2.2 Normal Contact Problem

The normal contact problem is mainly determined by using Heinrich Hertz theory. Hertz's elastic theory has been frequently used by many researchers in most of rail wheel contact modelling. The contact zone geometry and the normal pressure distribution in contact patch can be determined by using this theory (Vo, 2015).

Hertizian elastic contact theory

The theory of hertizian contact was proposed by Heinrich Hertz in 1882. He studied the pressures, stresses and deformations that occur when two curved elastic bodies are come into contact. This theory relates the circular contact area of a sphere with a plane (or more generally between two spheres) to the elastic deformation properties of the materials (Clayton, 1996; Johnson, 1974). This theory is the basis for studying rail-wheel rolling contact conditions.

Still many researchers are widely using this theory for contact problems. However, there are some limitations on this theory. Friction and the surface interaction like Van der Waals interaction, was not considered in this theory. The following basic assumptions were used in this theory for calculating the contact parameters: the contact stresses, the distributed pressures and the deformation (Munidasa et al., 2013; Ramazan, 2017).

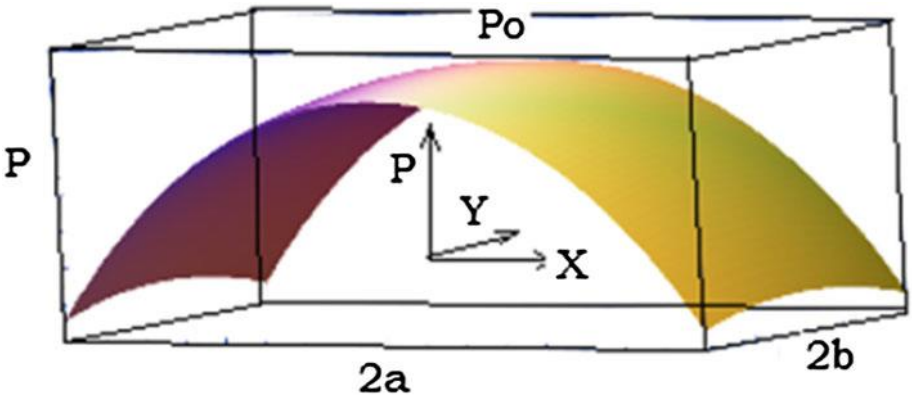

Figure 2.1 Pressure distribution across elliptical area

1. The material of the contacting bodies must be linearly elastic, homogeneous, and isotropic.
2. The radii of curvature are constant within the contact patch
3. The size of contact area should be much smaller than the size and the radii of curvature of the bodies in contact. In other words, the contacts between the two bodies are a non-conforming contact.
4. The bodies are considered as perfectly smooth; i.e. frictionless contact.

Hertzian contact stresses are the localized stresses that develop as two curved surfaces come in contact and deform slightly under the imposed loads. This amount of deformation is dependent on the modulus of elasticity of the material in contact. It gives the contact stress as a function of the normal contact force, the radii of curvature of both bodies and the modulus of elasticity of both bodies.

Depending on the above assumptions, Hertz proposed the solution for the determination of contact area and pressure distribution between two bodies in contact as shown in Figure 2.1. When two elastic nonconforming bodies are pressed together, then the contact area becomes elliptical in shape with a semi axis ‘a’ and a semi-minor axis ‘b’ and this yields the semi-ellipsoid contact pressure over contact area (Srivastava et al., 2014).

2.3 Tangential Contact Problem

The tangential contact problem is one of the rail-wheel contact problems, which has been attracting the attention of many researchers for the last many decades. The rail- wheel tangential contact problem consists of the relation between the tangential stresses/forces and the relative motion between the rail and wheel. This relative motion between the wheel and the rail is called slip.; For

the dry frictional contact between the rail and the wheel, the tangential contact problem is independent of the vehicle speed. In such cases, the tangential forces depend on the relative motion (slip), therefore, it is called creepage, rather than the real slip (Burgelman, 2016).

Starting from the early studies up to the date, the behavior of a wheel set running on the rail could not be considered as a ‘‘pure rolling’’ motion (Bosso et al., 2013). The motion between the rail and wheel exhibits small sliding at the contact surface. This small sliding can be described as a pseudo-sliding or micro-creepages; the forces caused by this creepage is called Creep forces. The tangential forces are transmitted between the rail and wheel during tractive, steering and braking and generate creepages due to the deformation of the contacting materials in and close to the contact patch (Shackleton, 2009).

The relative motion between two contacting surfaces can be described by defining the longitudinal creepage (Bosso et al., 2013), which is given in Eq. (2.1) as:

$$\xi = \frac{V_o - \omega r_o}{V_o} \tag{2.1}$$

Where; V_o is the longitudinal velocity of the vehicle, ω is the angular velocity of the wheel, r_0 is the rolling radius of the wheel

In a first stage (when the phenomena are governed by elastic deformation), the traction force is directly proportional to the creepage; the law can be expressed by Eq. (2.2)

$$F = c\xi \tag{2.2}$$

Where, c is an appropriate constant depending on the geometry and the normal load.

When the force approaches the saturation of the friction force, the trend becomes non-linear; at this stage, in a portion of the contact area, a loss of adhesion (localized slip) is generated. Further increasing the traction force causes the proportion of sliding to increase until it reaches the limit set by Coulomb’s law, which is illustrated in Figure 2.2 a and b.

$$F = \mu N \tag{2.3}$$

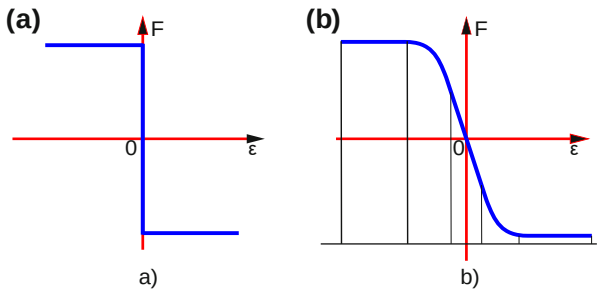

Figure 2.2 a) Coulomb friction force, and b) Rail-wheel friction force

2.4 Rail-Wheel Failure Mechanism

In this section, various investigations on the fundamental failure mechanism of rail wheel are briefly described. The rail-wheel materials may respond to the cyclic loading in different ways which result in a lot of damage occurrences (Vo, 2015). The rail wheel damage modes can be categorized into three: 1, Plastic deformation, 2, Wear and 3, Fatigue failures/Rolling contact fatigue.

2.4.1 Plastic deformation in rail-wheel contact

The rail wheel contact forces develop the stresses which lead the material behavior into elastic or plastic deformation. The developed stresses due to cyclic load usually occur in the elastic-plastic areas and leading this area to failure. In rail wheel contact, plastic deformation gradually occurs when the train wheel passes over the rail repeatedly. Plastic deformation in rail wheel is the non-reversible material disfigurement, which is mainly caused by high traction load. During operational life, rail wheel typically experiences millions of load cycles from the passage of train wheels. The behavior of material subjected to repeated loading during rolling or siding is governed by the strain, stress, wear and temperature change (Khoa Duy, 2015). The maximum contact pressure that the rail wheel material withstands under elastic deformation is called the shakedown limit.

The response of a material due to cyclic loading in a rolling contact/sliding contact depends on the magnitude of applied load and can be categorized into four categories: 1. perfectly elastic, 2. elastic shakedown, 3. plastic shakedown, and 4. ratcheting which are illustrated in Figure 2.3, where point A , B, C, D, and E shows fatigue limit, yield stress, elastic shake down, plastic shake down and ultimate strength of the material respectively (after Karttunen, 2015).

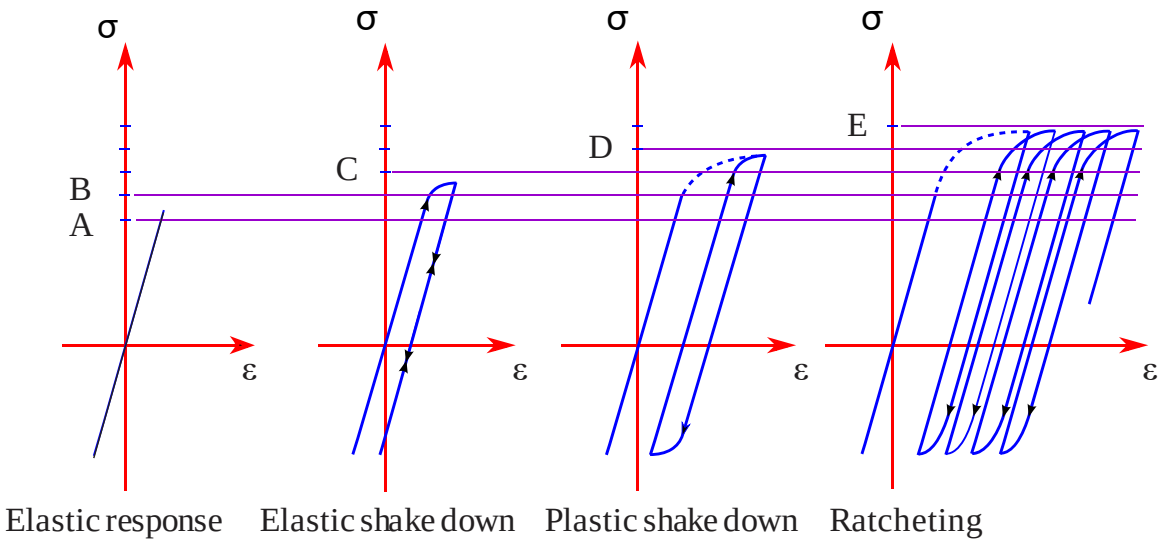

Figure 2.3 Material response to cyclic loading

1. **A perfectly elastic behavior-** if the maximum stress does not exceed the yield stress (elastic limit) of the materials in contact.
2. **Elastic shakedown behavior –** If the stress exceeded the elastic limit, but less than elastic shake down of the material, the material will deform during each cycle. During this process, material will accumulate protective residual stresses and harden. Due to the residual stresses and strain hardening, the steady state behavior after some load cycles is perfectly elastic again (Munidasa et al., 2013).
3. **Plastic shakedown behavior** -If the stress exceeds the elastic shakedown limit of the material, there will be plastic flow during each cycle. When the stress is less than the plastic shakedown limit, the cycle of plastic stress-strain (hysteresis) loop is closed without any accumulated plastic deformation. Consequently, the failure will occur by low cycle fatigue (LCF). This behavior is sometimes called cyclic plasticity, and the corresponding load limit is called the ratcheting threshold (or plastic shakedown limit).
4. **Ratcheting behavior –**When the stress exceeds plastic shakedown limit, the cycle of plastic stress-strain loop is open and there will be accumulation of the plastic strain. This process is called ratcheting.

In 2002, Daves and Fischer (Daves and Fischer, 2002) studied the effect of the surface roughness on the development of the stress and plastic zone by using 2D finite element modelling. In this investigation, the plastic deformation of rough surfaces (in case of friction) was greater than the

result obtained from friction less contact. In addition, a high plastic zone was developed from a few cycles of rolling contact with a rough surface.

In 2013, Munidasa and co-workers (Munidasa et al., 2013) investigated the rail wheel surface ratcheting due rolling contact. Authors used elastic-plastic finite element for studying the effect of friction on surface ratcheting and for modelling material behavior. According to this study, Surface ratcheting and fatigue are the main cause of material wear under normal operating condition. They also used a surface ratcheting model to predict wear in rail-wheel contact.

2.4.2 Wear in rail-wheel contact

Wear is the loss of material on the contacting surface. This phenomenon occurs whenever the contact surfaces come into sliding on each other. A material can wear by a number of different mechanisms or modes. How a material wears depends on the nature of the material and the other elements of the tribo-system which include environmental conditions and whether any contaminants are present, for example, wear debris and, in the case of the wheel-rail contact, friction modifiers, friction enhancers like sand, leaves, etc.(Lewis and Olofsson, 2009a; Vo, 2015)

In recent decades, various studies have been carried out in order to investigate the wear behavior of the rail-wheel.

In 2004, Telliskivi and Olofsson (Telliskivi and Olofsson, 2004) studied wear behavior depending on the linear wear law for different creepages. They calculated mass loss from rail surface due to tractive forces. The more rail material was worn away when the creepage was higher.

Tao and co-workers (Tao et al., 2016) investigated the effect of a contact model on the wheel wear simulation in 2016. The authors used Hertz theory and Kalker's contact as a reference to determine wheel wear. They concluded from their investigation that the wheel wear predicted using analytical models was deviated from the result obtained by Kalker's CONTACT. However, the difference is relatively small for curving cases, particularly Hertz method.

2.4.3 Fatigue failures in rail-wheel contact

When any components are subjected to cyclic stresses, it may fail at stresses levels much lower than its yield stress. Such failure phenomena that involves a gradual cracking of the component is

known as fatigue failure. Fatigue failure has been progressively more violent especially in the components that are subjected to cyclic loading. Nowadays, fatigue accounts for more than 90 percent of all service failures. There are three fundamental factors which can cause fatigue failure (Verma, 2011). These are:

- maximum tensile stresses of adequately high value,
- large enough variation or fluctuation in the applied stress, and
- adequately large number of cycles of the applied stress.

Fatigue failure is common in rail-wheel when micro cracks is initiated on the surface or subsurface of rail and wheel, and grow under the effect of a cyclic loading. Finally, fatigue leads rail wheel to catastrophic failure. Fatigue and wear are the main causes of rail-wheel failures. Wear is a fairly harmless, but costly, form of deterioration. On the other hand, fatigue failures cause unexpected fractures (break-off of large part) in wheels, which is the main causes of rail damage and train derailment. The fracture due to fatigue is the main factors contributing towards rail-wheel failures. Such failures are very harmful to human life besides huge economic loss. The fracture due to fatigue is the main factors contributing towards rail-wheel failures (Ekberg, 2000; Wirtu et al., 2011).

After repeated rolling compaction, plastic deformation layer will be formed and accumulated on the surface of rail-wheel. After the plastic deformation reaches certain value on this surface, micro cracks are generated and then further grow into macro cracks, and eventually propagate into a critical point where fractures can occurs (Peng and Jones, 2013). When the crack is propagated due to cyclic load, the process is called fatigue crack propagation. Fatigue failure of rails and wheels can lead to the rail-wheel fracture and a derailment. The crack is developed from a small flaw and propagated to the critical size. Generally, Crack propagation can be caused by cyclic loading.

Guagliano and Vergani (Guagliano and Vergani, 2005) studied the rolling contact failure. They used a semi-analytical stress analysis approach in order to get the stress- strain responses. A fatigue- ratcheting damage model was used for predicting the life time of a rolling component.

According to their study, the Bainitic steel shows longer lives than Hadfield steel under the same contact loading.

Patel and co-workers (Patel et al., 2013) investigated fatigue life of bolted rail joint bars. They developed 3-D Finite element model for estimating fatigue life and endurance strength at the section, both the static and dynamic loads were applied Depend on beam on elastic foundation theory, joint bar bending stresses was calculated by the finite element model and compared with the engineering approaches, which estimated the tensile reverse bending stress. The finite element model for the wheel over the joint calculates stresses that are higher than the engineering approach. The results showed that the engineering approach provides reasonable estimates for vertical bending only. However, the finite element analysis captures the combined effect of vertical and lateral bending.

Roundi and Gharad (Roundi and Gharad, 2014) studied fatigue behavior of train wheel under different cases of loading. Three cases of loading was applied to the model and finite element was used to get the form of nodal solution. The study showed the fatigue of the train wheel was characterized by the lifespan, coefficient, safety and damage result.

Kotoula (Kotoula, 2015) developed a model of crack path for 2-D crack primary suited in railway wheel under rolling contact fatigue. The authors used Plank and Kuhn criterion to identify whether the crack will twist or follow mode I (tensile mode) path or mode II (shear mode). If the probability of controlling crack growth by the mode I is more, the maximum tensile stress range criterion will be used to predict the direction of crack growth.

2.5 Classification of Fatigue Failures of Rail-wheel

In general, rail wheel fatigue failures can be categorized into two groups which are surface-induced and subsurface-induced fatigue failures, which is the consequence of crack nucleation (initiation) and propagation. The cracks initially develop at the subsurface often result from the metallurgical defects. In addition, the travelling intensity (number of load cycles) and the axle load are two other main reasons causing surface-initiated cracks. Surface induced fatigue in rails can be the cause for

the formation of the head checking or squat and subsurface fatigue can result in the tache ovule and shelling formation (Lewis, 2009).

2.5.1 Surface-induced fatigue failures

Surface-induced failures are a result of gross plastic deformation of the rail-wheel material close to the running surface (Ekberg, 2000). After repeated rolling compaction, plastic deformation layer will be formed and accumulated on the surface of rail-wheel. After the plastic deformation reaches certain value on this surface, micro cracks are generated and then further grow into macro cracks, and eventually propagate into a critical point where catastrophic failure can occurs (Peng and Jones, 2013). When loading exceeds a certain level, surface induced cracks will occur higher cracking frequencies and exceed appropriate levels. For rolling contact problem, surface induced fatigue cracks are mainly initiated by ratcheting. When the crack is propagated due to cyclic load, the process is called fatigue crack propagation. The fatigue failure which resulted from the initiated crack on the surfaces of wheel and rail is called surface-induced fatigue failures. The typical appearance of surface-induced fatigue failure is shown in Figure 2.4 (Lewis, 2009).

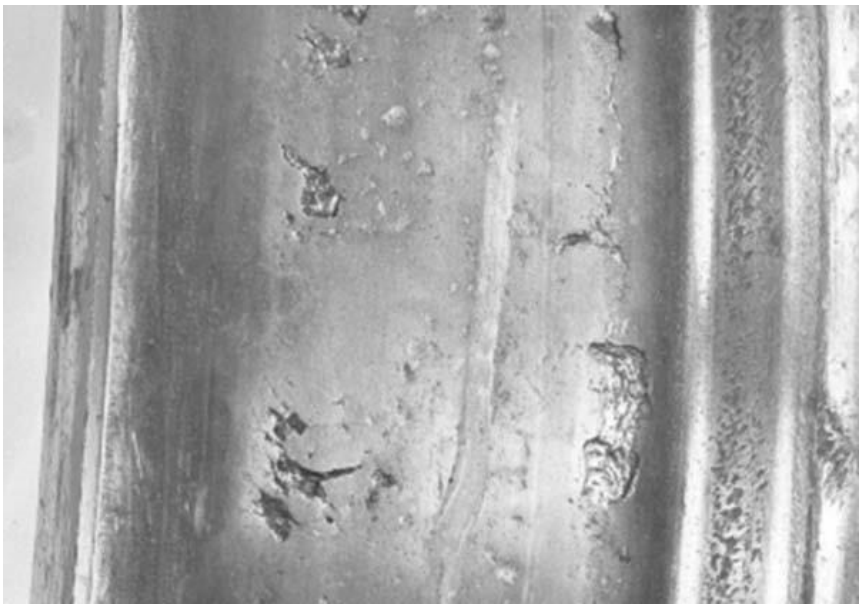

Figure 2.4 Wheel surface fatigue damage

2.5.2 Sub-surface induced fatigue failures

In 2005, Guaglino and Vergani (Guagliano and Vergani, 2005) investigated sub-surface cracks in railway wheels. They performed the experiment on photo-elastic fringes for the approval of the results. The authors presented that in both the wheels and the rails, cracks can turn back towards the surface leading to the formation of a detached flake (spalling), which is very common in rail wheel contact conditions. This fatigue failure is caused from cracks induced below the surface. The initiation may occur due to a macroscopic material defect and can also initiated in a 'virtually defect-free' material. After initiation, the cracks may develop at the depth of 10 to 30 mm based on material properties. If a crack finally grows towards the surface of the rail-wheel, a large piece of the wheel tread will break loose. Such type of fatigue failures is the more dangerous than surface-induced fatigue failures (Ekberg and Sotkovszki, 2001).

In 2013, Peng and Jones, studied fatigue crack propagation in a rail wheel and discussed that fatigue crack in railway wheels is initiated at a subsurface and occurs under mixed mode (Peng and Jones, 2013). The values of the stress intensity factor of the mode I and mode II for the tested loading angles were obtained by finite element analysis.

2.6 Research Gap

Several researchers have proposed different methods in order to combat the fatigue failure. Some have proposed, traditional failure criteria, which depends on maximum stress or strain energy density, but these can't justify failures of many structures occurred at stress levels lower than the ultimate strength of the material. Others have proposed a uniaxial fatigue models, in which the loading mode is only in one axis. However, this can describe the loading condition of the rail wheel contact problem. Some of the researchers also proposed the multiaxial fatigue modelling, which depends on the proportional loading conditions. In fact, this also can't justify the loading condition of the rail wheel since the rail wheel loading condition is non-proportional. This suggests a need for methods that can effectively predict the occurrence of RCF cracks. Effective predictions require computational tools and mathematical model that can accurately simulate the rail wheel material behaviour under a non-proportional loading condition. Therefore, the objective of this study is to address this problem of rail wheel fatigue failure.

CHAPTER 3

RAIL WHEEL CONTACT MODELLING

In this chapter, the rail wheel contact problems are discussed under two categories; namely 1, normal contact problem and 2, tangential contact problem. For solving the normal contact problem, the commonly used analytical method, which is Hertzian elastic theory, is presented. Among tangential contact theory, Kalker's linear theory and Polach's tangential theory are discussed for solving the tangential contact problem.

3.1 Rail Wheel Contact Overview

When the wheel and rail brought into contact, the applied forces will be distributed over the contact area, which in most cases is very small compared with the size of the wheel and rail. Thus, the rail wheel contact is a non-conformal contact in which the rail and wheel come into contact at one point. At this point there will be small contact patch where the applied forces are transmitted vertically along z-axis as normal pressure and horizontally along X and Y-axis as tangential shear stresses. The main goal of analyzing such contacts is to calculate the magnitude of stresses and deformations, both at the contact interface and in the interior of the bodies. The size and shape of the contact area can also be calculated.

The wheel and rail have relative motions with respect to each other at the contact interface and the stress is acting in the normal direction due to normal load (F_z) and in the tangential direction due to tangential forces (braking and traction (F_x), guiding or parasite (F_y) (Ivan Y., 2008). In order to simplify the rail wheel contact problems, we can consider it as partly a normal contact problem and partly as a tangential contact problem. Both contact problems are dependent on each other, but

in order to solve separately Hertzian elastic contact theory is used for normal contact problem and Kalker's Linear theory and Polach's tangential theory are used for the tangential contact problem.

3.2 Rail-Wheel Contact Geometry

The interface between the wheel and the rail is of special importance. The rail-wheel contact profile, shown in Figure 3.1, can be divided into the wheel flange, which contacts the rail at the gauge corner in curves or turnouts, and the wheel tread, which contacts the rail top (Burgelman, 2016). As illustrated in Figure 3.2, there are three possible regions of rail wheel contact; namely region A, region B and region C.

Region A: Region A defines the contact between the field sides of both rail and the outer tread of the wheel. This contact is least likely to occur here and if it does, high contact stress is induced and yields wear and rolling contact fatigue.

Region B: This region is showing the contact between the central region of the rail crown and wheel tread. This contact is usually made in this region when a vehicle negotiates tangent or mildly curved tracks. This contact is associated with high contact stresses, low lateral creep forces with more significant longitudinal creep forces.

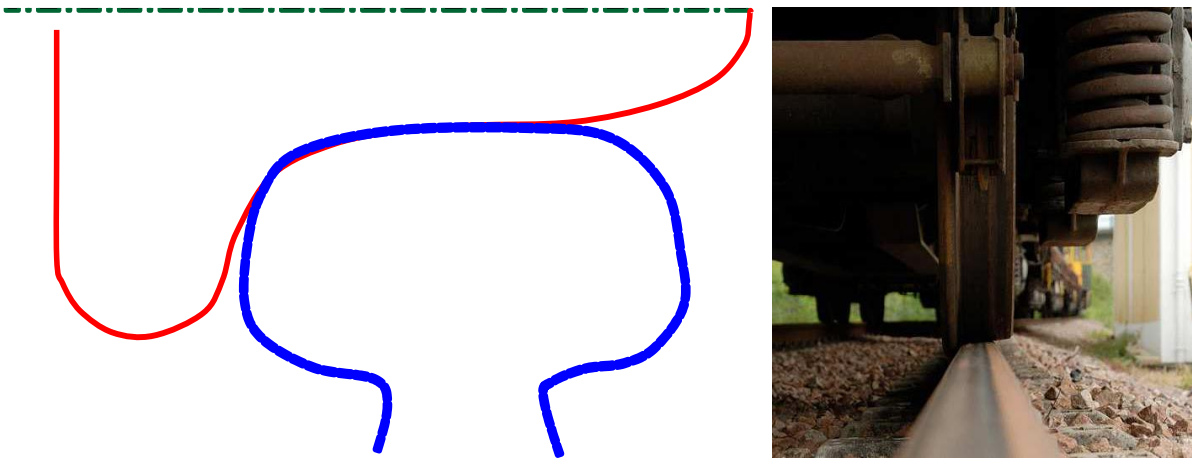

Figure 3.1 Profiles of a wheel and rail

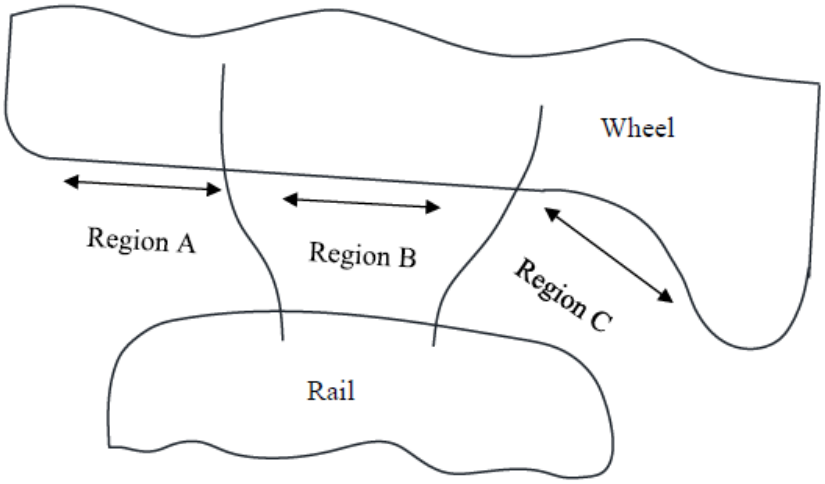

Figure 3.2 Rail-wheel contact zones

Region C: Region C defines the contact between the gauge corner of the rail and and the flange throat of the wheel. High lateral creep forces are produced in this region due to high angle of attack associated with the contact in the gauge corner. The contact patch is smaller than that of region B and high contact stresses can occur in this contact area. Two parts of contact can occur simultaneously in the region of B and C.

3.3 Normal Contact Problems of Rail-Wheel

In the normal contact problem; the shape and size of the contact patch, the pressure distribution and contact stresses are determined from the geometry of the rail and wheel and the normal load. In case of the quasi-identity implication, the normal contact problems can be solved separately from the tangential problems, which means the tangential stresses have no effect on the normal pressures distribution (Ulrich, 2016).

The most commonly used analytical method for solving the normal contact problems is the Hertzian contact theory in which the contact surfaces of both bodies are non-conformal. In Hertzian contact theory, the contact patch of the rail-wheel is assumed to be elliptical in shape. The contact patch and pressure distribution can be calculated based on Hertz's assumption.

Initially, two bodies are brought into contact at a single point without transmitting any forces as shown in Figure 3.3, which is adopted from (Ayasse and Chollet, 2006). The tangent plane which is common for both contacting surfaces is placed at the point of contact and the Cartesian

coordinate system (x,y,z) is also placed at this contact point (origin 'o'), with the *z* axis perpendicular to the tangent plane, and the x-y axis defines the tangent plane.

In order to determine the rail wheel contact parameters under normal contact problem, the four main curvature of half spaces $R_x^{(w)}$,$R_y^{(w)}$, $R_x^{(r)}$ and, $R_y^{(r)}$, are illustrated in Figure 3.4, where $R_x^{(w)}$ and $R_y^{(w)}$ are the radii of curvature of the wheel along x and y axis, and $R_x^{(r)}$ and, $R_y^{(r)}$ are the radii of curvature of the rail along x and y axis respectively.

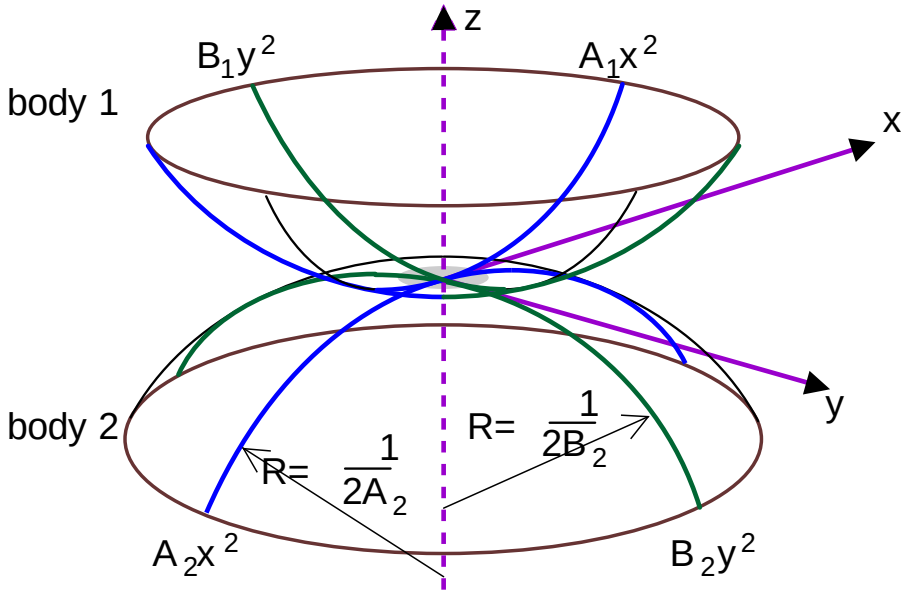

Figure 3.3 Hertzian Contact of two elastic bodies

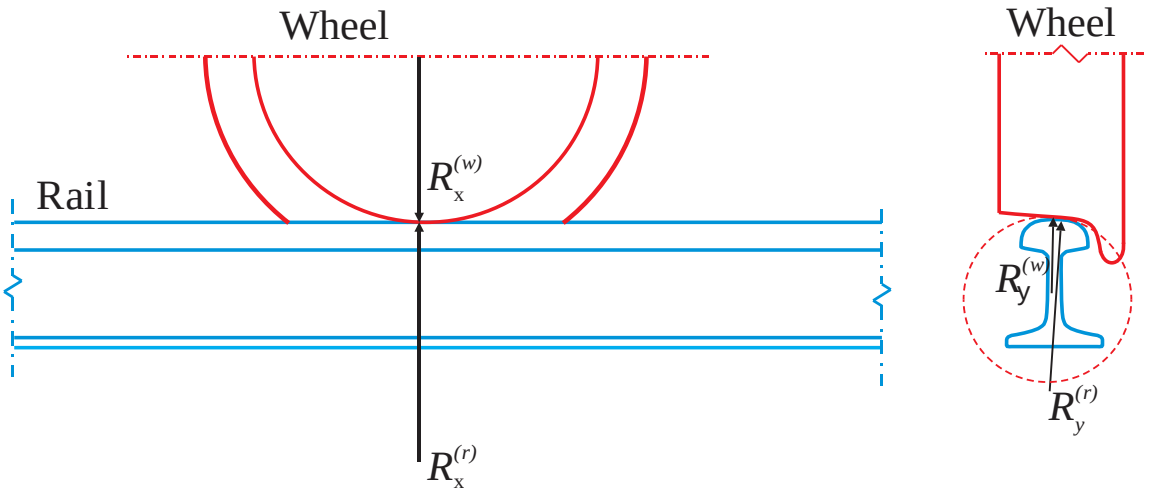

Figure 3.4 Wheel–rail configuration showing different principal relative radii of curvature

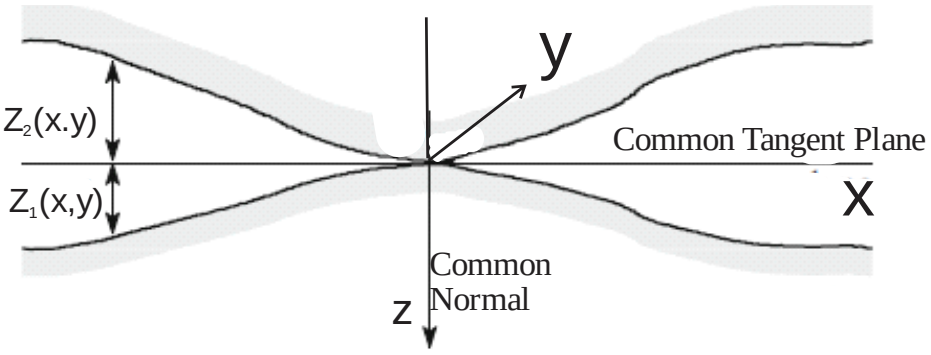

Figure 3.5 Illustration of normal distance between two elastic body

The two elastic bodies shown in Figure 3.5 meet each other at point 'o', where the normal distance between them is zero. The surface of these elastic bodies near the point of contact 'o', before the load is applied, can be defined by function of second order polynomials $Z^{(1)}(x,y)$ and $Z^{(2)}(x,y)$ (Ayasse and Chollet, 2006).

$$Z^{(1)}(x,y) = A^{(1)}x^2 + B^{(1)}y^2 \qquad (3.1)$$
$$Z^{(2)}(x,y) = A^{(2)}x^2 + B^{(2)}y^2$$

The surface of rail and wheel shown in Figure 3.6 which meet each other at point 'o' can be defined in the same manner with Eq. (3.1) by function $Z^{(w)}(x,y)$) and $Z^{(r)}(x,y)$, where;

$$Z^{(w)}(x,y) = A^{(w)}x^2 + B^{(w)}y^2 \qquad (3.2)$$
$$Z^{(r)}(x,y) = A^{(r)}x^2 + B^{(r)}y^2$$

Where, $A^{(w)}, B^{(w)}, A^{(r)}, and\ B^{(r)}$ coefficients are positive constants and the superscripts (w), (r) represents the bodies of wheel and rail respectively.

$$A^{(w)} = \frac{1}{2R_x^{(w)}}; B^{(w)} = \frac{1}{2R_y^{(w)}}; A^{(r)} = \frac{1}{2R_x^{(r)}}; B^{(r)} = \frac{1}{2R_y^{(r)}} \qquad (3.3)$$

For the elliptical bodies, the vertical separation distance (gap function) can be defined as (Barber, 2018a)

$$d(x,y) = \frac{x^2}{2R_x} + \frac{y^2}{2R_y} \qquad (3.4)$$

Where R_x and R_y are the principal radii of curvature of the surface.

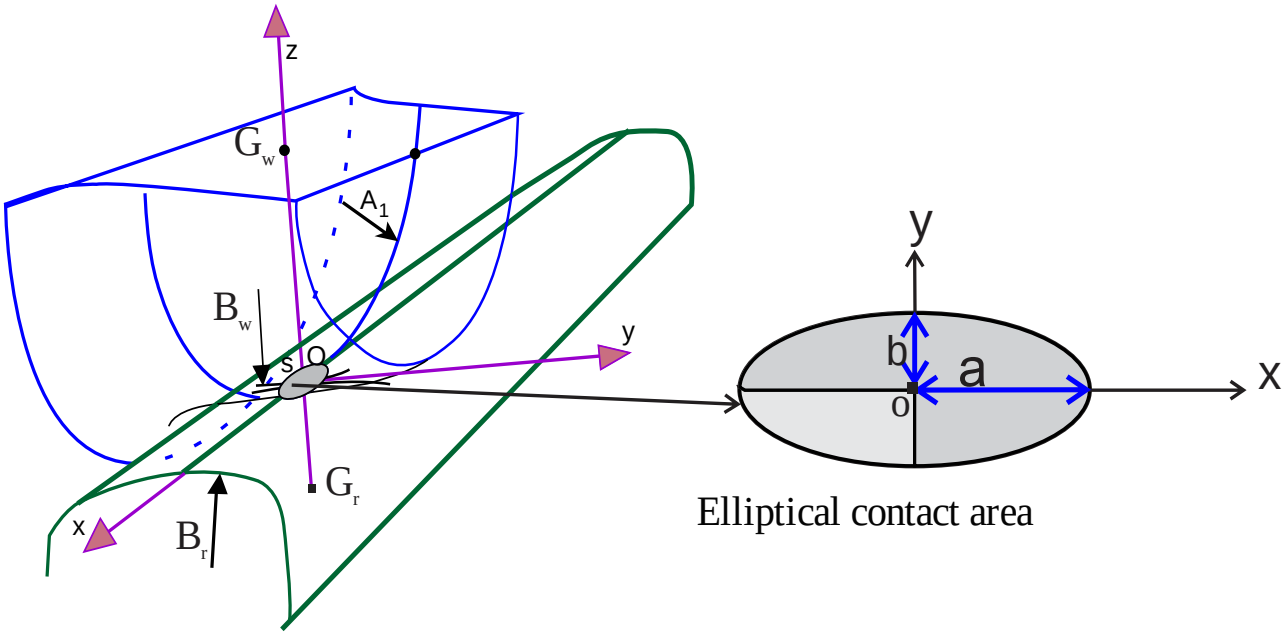

Figure 3.6 Elliptical contact in the railway case

In rail wheel case Figure 3.4, the vertical separation distance that would occur if the surfaces of the body placed in contact with a tangent plane is described by the sum of two distances.

$$d(x,y) = Z^{(w)}(x,y) + Z^{(r)}(x,y) = Ax^2 + By^2 \tag{3.5}$$

Where, $A = A^{(w)} + A^{(r)}$ and $B = B^{(w)} + B^{(r)}$. For rail-wheel case, $A^{(r)}$ is neglected because the radius of the rail is assumed to be infinite: the rail is straight.

From Eq. (3.4)and (3.5), we obtain

$$d(x,y) = Ax^2 + By^2 = \frac{x^2}{2R_x^{(w)}} + \frac{y^2}{2R_y^{(w)}} + \frac{y^2}{2R_y^{(r)}} \tag{3.6}$$

From Eq. (3.4), $\frac{1}{R_x}$ and $\frac{1}{R_y}$ are composite radii, which can be defined as

$$\frac{1}{R_x} = \frac{1}{R_x^{(w)}} = 2A$$

$$\frac{1}{R_y} = \frac{1}{R_y^{(w)}} + \frac{1}{R_y^{(r)}} = 2B \tag{3.7}$$

Note that, $R_x^{(w)}$ is not the actual rolling radius of the wheel, but is an effective rolling radius. $R_x^{(w)}$ is defined in terms of wheel conicity γ and rolling radius R_o. $R_x^{(w)}$ is differs from the actual rolling radius of the wheel and can be determined as (Ayasse and Chollet, 2006):

$$\frac{1}{R_x^{(w)}} = \frac{\cos\gamma}{R_0} \tag{3.8}$$

The difference between $R_x^{(w)}$ and R_0 is less than 0.5% when the values of the wheel conicity γ is between 0 and 5 degrees (Keylin, 2012). The effect of the conicity in determining the contact patch dimension 'a' and 'b' can be ignored since its influence is very small (e.g. for the wheel conicity of 5°, $\cos\gamma = 0.9962$). Therefore, in this study, $R_x^{(w)}$ and $R_y^{(r)}$ are assumed to be the rolling radius of the wheel and the radius of the rail head respectively.

i. Elliptical contact area of rail-wheel

The wheel-rail contact conditions can be defined by the general case of an elliptic contact area, which are illustrated in Figure 3.6 (Ayasse and Chollet, 2006). The semi-axes 'a' and 'b' of the contact ellipse and the reduction distance 'δ', between the bodies centers (penetration) are dependent on material properties, the rail wheel geometry and the prescribed force, and also given by Eq. (3.9) up to (3.11).

$$a = m\left(\frac{3}{4}\frac{F_n}{E^*}\frac{1}{A+B}\right)^{\frac{1}{3}} \tag{3.9}$$

$$b = n\left(\frac{3}{4}\frac{F_n}{E^*}\frac{1}{A+B}\right)^{\frac{1}{3}} \tag{3.10}$$

$$\delta = r\left(\left(\frac{3}{4}\frac{F_n}{E^*}\right)^2\left(A+B\right)\right)^{\frac{1}{3}} \tag{3.11}$$

Where,

$$\frac{1}{E^*} = \frac{1-\nu_w^{\,2}}{E_w} + \frac{1-\nu_r^{\,2}}{E_r} \tag{3.12}$$

Hence, with E_w, E_r and v_w, v_r being the modulus of elasticity and Poisson's rations of the wheel and rail respectively; m and n are coefficients for semi-axis lengths of ellipse, which was tabulated by Hertz as a function of the ratio g= $\frac{n}{m}$.

The geometrical dependency is defined by using an intermediate parameter, angle 'θ' and determined by Eq.(3.13):

$$\cos\theta = \frac{|B-A|}{A+B} \tag{3.13}$$

$$A+B = \frac{1}{2}\left(\frac{1}{R_x^{(w)}} + \frac{1}{R_x^{(r)}} + \frac{1}{R_y^{(w)}} + \frac{1}{R_y^{(r)}}\right) \tag{3.14}$$

$$B-A = \frac{1}{2}\sqrt{\left(\frac{1}{R_x^{(w)}} - \frac{1}{R_y^{(w)}}\right)^2 + \left(\frac{1}{R_x^{(r)}} - \frac{1}{R_y^{(r)}}\right)^2 + 2\left(\frac{1}{R_x^{(w)}} - \frac{1}{R_y^{(w)}}\right)\left(\frac{1}{R_x^{(r)}} - \frac{1}{R_y^{(r)}}\right)\cos(2\psi)} \tag{3.15}$$

Where, ψ is the angle between the radius of the wheel and rail.

Knowing an intermediate parameter θ, the Hertzian non-dimensional coefficients, m, n and r can be found by using pre-calculated table (see **Table 3-1**).

There is another method of determining m and n values. Analytical approximation of $\frac{n}{m}$ and mn values being the function of $\frac{A}{B}$ ratio are given by Eq. (3.16) and Eq. (3.17) (Ayasse and Chollet, 2006):

$$\frac{b}{a} = \frac{n}{m} \approx \left(\frac{A}{B}\right)^{0.63} \tag{3.16}$$

$$(mn)^{\frac{3}{2}} \approx \left(\frac{1+\frac{A}{B}}{2\sqrt{\frac{A}{B}}}\right)^{0.63} \tag{3.17}$$

Table 3-1 Hertz coefficients for $A/B < 1$

$\theta°$	90	80	70	60	50	40	30	20	10	0
$g = \frac{n}{m} = \frac{b}{a}$	1	0.7916	0.6225	0.4828	0.3652	0.2656	0.1806	0.1080	0.047	0
m	1	1.128	1.285	1.486	1.754	2.136	2.731	3.816	6.612	∞
n	1	0.8927	0.8000	0.7171	0.6407	0.5673	0.4931	0.4122	0.311	0
r	1	0.9932	0.9726	0.9376	0.8867	0.8177	0.7263	0.6038	0.428	0

The exponent 0.63 is a compromise (Ayasse and Chollet, 2006). When $\frac{A}{B}$ ratio approaches to one, the exponent would be two thirds rather than 0.63, but the 0.63 is better for describing the slender ellipse, and the deviation results from the tabulated values are not more than 5% for $\frac{b}{a}$ ratio between $\frac{1}{25}$ and 25.

From Eq. (3.16), solving for 'n' values,

$$n = m\left(\frac{A}{B}\right)^{0.63} \tag{3.18}$$

Then substituting in Eq. (3.17), and solving m,

$$m = \sqrt{\left(\frac{1+\frac{A}{B}}{2\sqrt{\frac{A}{B}}}\right)^{0.42}\left(\frac{A}{B}\right)^{-0.63}} = \left(\frac{A}{B}\right)^{-0.315}\left(\frac{1+\frac{A}{B}}{2\sqrt{\frac{A}{B}}}\right)^{0.21} \tag{3.19}$$

While the wheel material has Young's modulus (E) of 206 GPa, the rail material has 200 GPa. The Poisson's ratio for both parts is 0.3.

Then, solving n,

$$n = \left(\frac{A}{B}\right)^{0.315}\left(\frac{1+\frac{A}{B}}{2\sqrt{\frac{A}{B}}}\right)^{0.21} \tag{3.20}$$

ii. Pressure distribution in the contact patch

The contact pressure distribution in an elliptical contact area has a semi-ellipsoidal form, as shown in Figure 3.7 [After (Shahzamanian Sichani, 2016)]. Once the curvatures around the point of contact are known, the contact area can be defined by the Eq. (3.21)

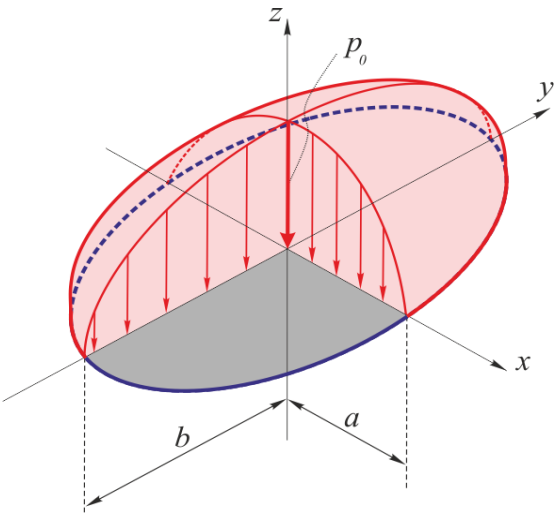

Figure 3.7 Hertzian contact patch and pressure distribution

$$C = \left\{ (x, y) : \left(\frac{x}{a}\right)^2 + \left(\frac{y}{b}\right)^2 \leq 1 \right\} \tag{3.21}$$

The contact pressure distribution applied over the contact area becomes be semi-elliptical.

$$P(x, y) = P_0 \sqrt{1 - \left(\frac{x}{a}\right)^2 - \left(\frac{y}{b}\right)^2} \tag{3.22}$$

Where $P(x, y)$ is the pressure distribution, P_o is the maximum contact pressure developed at the center of the contact area, a and b are half-width of contact patch in the x and y direction respectively.

The normal load F_n, applied on the wheel in relation to the normal pressure is given Eq. (3.23):

$$F_n = \iint p(x, y) dx dy \tag{3.23}$$

By substituting Eq. (3.22) in Eq. (3.23) and integrating, we obtain

$$F_n = \frac{2}{3} P_0 \pi a b \tag{3.24}$$

From Eq. (3.24), the maximum contact pressure P_0, developed at the center of the contact area (x=0 and y=0) becomes

$$P_o = \frac{3F_n}{2\pi a b} \tag{3.25}$$

By substituting Eq. (3.25) in Eq. (3.22)

$$P(x,y) = \frac{3}{2\pi a b} F_n \sqrt{1 - \left(\frac{x}{a}\right)^2 - \left(\frac{y}{b}\right)^2} \tag{3.26}$$

3.4 Tangential Contact Problem of Rail-Wheel

The rail-wheel normal contact problem is described in Section 3.3 and the rail-wheel tangential contact problem is described in this section. The tangential contact problem comprises of the creep forces and the relative motion between the rail and the wheel. In order to solve the tangential contact problem, first the creepages and the tangential contact forces are clearly defined inside the contact area and calculated depending on the creepage components and the normal pressure distributions (Ulrich, 2016), then Kalker's linear theory (Kalker, 1990) and Polach's tangential theory are used to analyze the tangential contact problem of rail wheel.

3.4.1 Creepages

When the motion between the wheel and rail is not a pure rolling, the wheel slides or spins over the rail. The relative slips between the rail and wheel is creepages. The slip between the rails and the wheels arises longitudinal creep and tangential (tractive) creep forces, which is called friction forces. There are three components of the sliding motion; longitudinal direction (in moving direction or x-axis), lateral direction (transversal or y-axis)) and rotational (z-axis). The creep forces are greatly influenced by the creepage and spin in all three components of the sliding motion, which is based on the sliding velocities and angular velocity. Creep forces are defined as a function of creepages and spin (Orvnäs, 2005; Shevtsov, 2008). .

The contact area between the rail and wheel can be categorized into stick (completely no slip) and slip regions. At lower values of creepages, the relationship with the creep force can be regarded as

linear, thus linear coefficients are used to calculate the creep forces shown in Figure 3.8. From this figure, it is clearly shown that when the tractive force increases, the stick region decreases and the slip region increases, and resulting rolling and sliding contact between the rail and wheel. When the tractive force reaches the maximum value, the stick region disappears and the complete contact area is in the region of pure sliding. At higher values of creepage, the relationship with the traction forces become nonlinear. The maximum level of the traction force depends on the slip features of the contact patch. This can be determined by the coefficients of fiction, μ and normal forces, N in the contact patch.

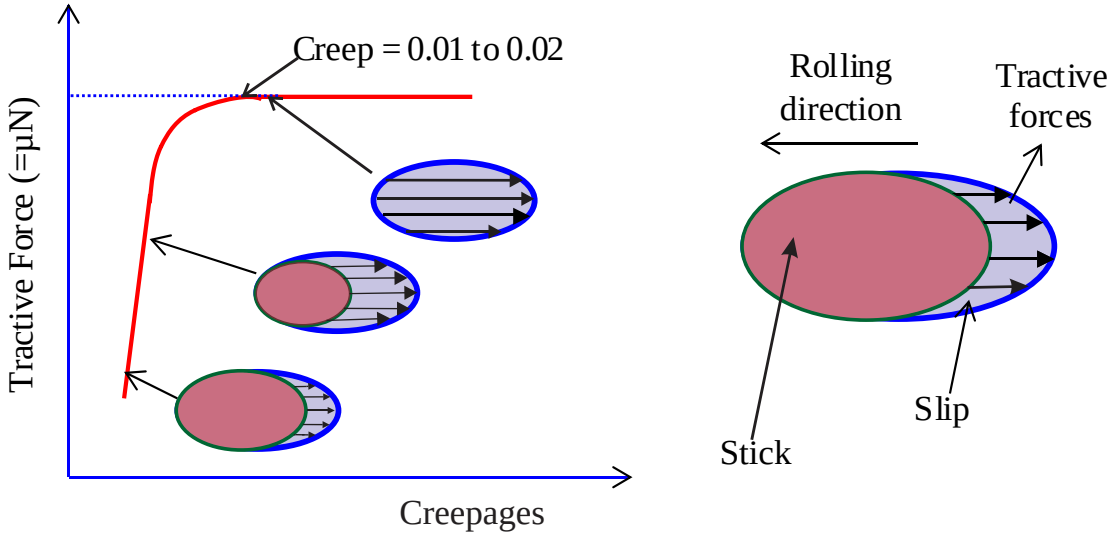

Figure 3.8 Relationship between traction force and creep in the rail-wheel contact

(Adapted from (Munidasa et al., 2013))

Creepage in the longitudinal, ξ is defined as the ratio of the creep velocities in longitudinal direction (v_{long}) to the rolling velocity ($v_{rolling}$, or vehicle mean velocity). The creepage lateral direction, η is the ratio of creep velocity in lateral direction to the rolling velocity of the vehicle. Spin (ϕ) is defined as the ratio of the angular sliding velocity (Ω) to the rolling velocity. Eq.(3.27)-(3.29) are defining the longitudinal, lateral and spin creepages respectively.

$$Longitudinal\ creepage, \xi = \frac{v_{long}}{v_{rolling}} = \frac{v_x^{(w)} - v_x}{v_{rolling}} \tag{3.27}$$

$$Lateral\ creepage, \eta = \frac{v_{lat}}{v_{rolling}} = \frac{v_y^{(w)} - v_y}{v_{rolling}} \tag{3.28}$$

$$Spin\ creepage, \phi = \frac{\Omega_n}{v_{rolling}} = \frac{\Omega_z^{(w)} - \Omega_z}{v_{rolling}} \tag{3.29}$$

Where, $v_x^{(w)} = \omega_o R_o$ is actual forward velocity of the wheel; $\upsilon_x = \omega R_{roll}$ is pure rolling forward velocity of the wheel; R_{roll} is the rolling radius; $v_{rolling}$ is the forward velocity of the vehicle due to rolling (the forward velocity of the wheel set); $v_y^{(w)}$ is actual lateral velocity of the wheel; v_y, is pure rolling lateral velocity; $\Omega_z^{(w)}$ is angular velocity of the wheel; and Ω_z is angular velocity of the rail.

3.4.2 Kalker's linear theory

Kalker linear theory (Kalker, 1990) presented that the creep forces and spin moments are defined as a function of the two creepages (lateral and tangential), spin, dimensions of the contact ellipse, and the normal forces. The relationship between the two creepages, spin and creep forces and spin moments. For small values of creepages, the creep forces can be determined from the linear coefficients since the relationship can be considered as linear. However, for large values of creepages the relationship becomes highly non-linear (i.e. the creep forces approach saturation value) and the creep forces can be determined from the normal forces and friction coefficients.

The longitudinal creep force F_x, the lateral creep force F_y, and the rotating creep moment M_z, which develop between the rail and wheel can be determined by Eq. (3.30) (Shabana et al., 2007; Shevtsov, 2008).

$$\begin{bmatrix} F_x \\ F_y \\ M_z \end{bmatrix} = -Gab \begin{bmatrix} c_{11} & 0 & 0 \\ 0 & c_{22} & \sqrt{ab}c_{33} \\ 0 & -\sqrt{ab}c_{23} & c_{33} \end{bmatrix} \begin{bmatrix} \xi \\ \eta \\ \phi \end{bmatrix} \tag{3.30}$$

Where, a and b are contact ellipse semi-axes, G is the combined shear modulus of rigidity of the rail and wheel materials, C_{ij} are called Kalker's creep and spin coefficients, i,j ∈ {1, 2, 3}, ξ, η and ϕ are the longitudinal, lateral, and spin creepages at the point of contact, respectively. Kalker

tabulated the creep and spin coefficients C_{ij} , being functions of Poisson's ratio and the ratio of the contact ellipse semi-axes (Kalker, 1990; Lewis and Olofsson, 2009).

The combined modulus of rigidity for the rail and wheel can be obtained using Eq. (3.31)

$$\frac{1}{G}=\left(\frac{1-v_w^2}{G_w}+\frac{1-v_r^2}{G_r}\right) \tag{3.31}$$

Where, G_r and G_w are the shear modulus; υ_r and υ_w are the Poisson's ratios of the rail and the wheel respectively. The value of shear modulus for both the rail and wheel used in this thesis are 21 GPa (Ma and Markine, 2015); then substituting in Eq. (3.31), the value of combined modulus of rigidity for the rail and wheel was found to be 11.6 GPa.

The polynomial approximation the creep and spin coefficients C_{ij} , as a function of $\frac{b}{a}$ ratio of the contact ellipse are given in Eq (3.32)-(3.34). Their values are not far from π for the $\frac{b}{a}$ ration approaches to 1 (Ayasse and Chollet, 2006).

$$C_{11}=3.2893+\frac{0.975}{b/a}-\frac{0.012}{\left(b/a\right)^2} \tag{3.32}$$

$$C_{22}=2.4014+\frac{1.3179}{b/a}-\frac{0.02}{\left(b/a\right)^2} \tag{3.33}$$

$$C_{23}=0.4147+\frac{1.0184}{b/a}+\frac{0.0565}{\left(b/a\right)^2}-\frac{0.0013}{\left(b/a\right)^3} \tag{3.34}$$

For small values of creep and spin, Kalker's linear theory is sufficient to determine the creep forces and spin moments. However, for large values of creep and spin, Kalker's linear theory is not applicable since it does not involve the friction forces' saturation effect, i.e., it does not prove that $F_{lat}\leq\mu$ (Shevtsov, 2008).

In this study, the rail is assumed to be straight and, thus only pure longitudinal creepage is considered. Therefore, lateral creepage and spin creepage are ignored.

3.4.3 Polach's tangential theory

Polach‟s tangential theory is three-dimensional contact model based on the integration of shear stress in the contact interface which compute the traction force (Polach, 1999). The proposed method is based on hertz elliptical contact area. It assumes that the elliptical contact is divided to stick and slip regions. Polach‟s theory also considered the relationship between creepage and Coefficients of friction.

$$Q = \int \int \tau dx dy \tag{3.35}$$

The maximum tangential stress at any arbitrary point is

$$\tau_{max} = \mu\sigma \tag{3.36}$$

Where, σ is a normal stress.

From the Figure 3.9 (Vo, 2015), it is clearly shown that as the tangential stress achieves its maximum value, sliding phenomena will happen. The tangential traction force is described by Polach theory. Only longitudinal creep is considered in this thesis, since the wheel is assumed to be set to move on a straight-line having wheel tread-rail head contact.

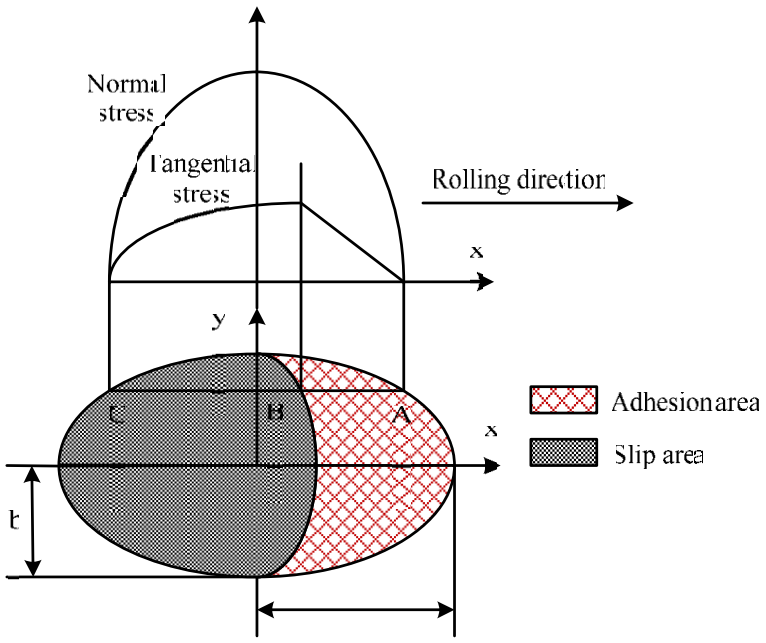

Figure 3.9 Polach's normal and tangential stress distribution

$$Q = \frac{2\mu F_n}{\pi}\left(\frac{\varepsilon}{1+\varepsilon^2} + \arctan\varepsilon\right) \tag{3.37}$$

Where, F_n wheel load, μ is coefficient of friction, ε is gradient of the tangential and is obtained by Eq. (3.38)

$$\varepsilon = \frac{2}{3}\left(\frac{G\pi abc_{ij}}{F_n\mu}\right) \tag{3.38}$$

G is the modulus of rigidity given by,

$$G = \frac{E}{2(1+\nu)} \tag{3.39}$$

And c_{ij} is the longitudinal creepage coefficient given by Eq (3.32), the longitudinal creepage is calculated as 0.001.

$$c_{ij} = c_{11} \times \xi \tag{3.40}$$

C_{11} is Kalker‟s creep coefficient, it is found from the Kalker‟s creep coefficient table or from Eq. (3.32).

CHAPTER 4

CYCLIC PLASTICITY MODELING OF RAIL WHEEL

In this chapter, the theory of plasticity, which discusses about the material response under monotonic tensile loading and cyclic loading, is presented first. Then, the characteristics of the elasto-plastic deformation, which includes cyclic hardening/softening, cyclic mean stress relaxation, and ratcheting are discussed. Finally, the constitutive model, which defines the stress-strain response of rail wheel material under cyclic load in mathematical ways, is discussed.

4.1 Theory of Plasticity

When a typical metal is subjected to loading, it undergoes recoverable elastic deformation and unrecoverable plastic deformation. To understand elasto-plastic deformation of metals, studying material behaviour under monotonic tensile loading and cyclic loading is essential. Constitutive models, which simply describe the stress–strain response of the material in mathematical ways has a great role in plasticity modelling.

4.1.1 Material behavior under monotonic tensile loading

The relationship between stress and strain for typical materials in multiaxial stress states has been an extension of the observations made under monotonic tensile loading test. A study of material response under monotonic tensile loading is a significant step to understand the mechanism of material response. When a typical material subjected to a monotonic tensile loading, both elastic and plastic responses can be observed. Up to the yield stress, all the strains are elastic and the relationship between stress and strain can be expressed by Hooke's law, in which the stress and strain are proportional to each other, between point O and A in Figure 4.1. Point A in this figure, is the limit of the elastic response of the material.

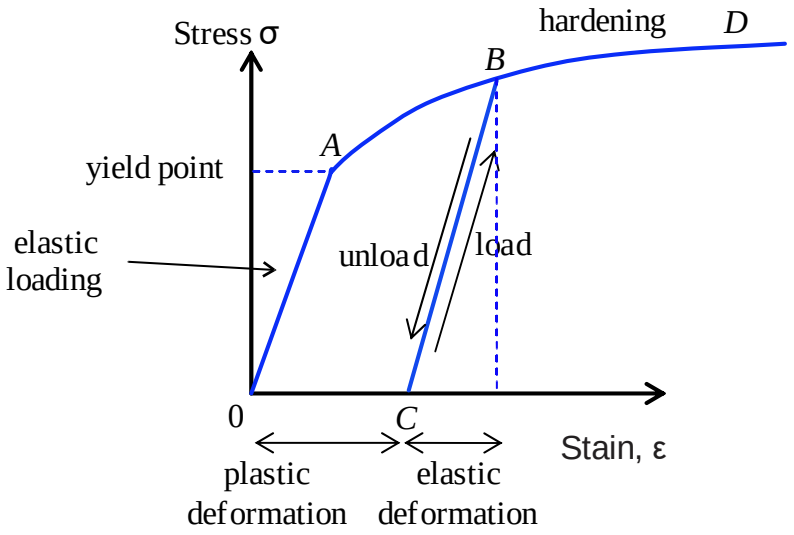

Figure 4.1 Idealized stress-strain curve for uniaxial tensile test.

After yield stress is achieved, the material undergoes permanent plastic deformation which results plastic strain and thus the elasto-plastic law covers the relationship between stress increment and now a combination of elastic and plastic strain increment. If the load is reduced, the unloading response of material is firstly a straight-line BC, which is basically parallel to OA, which is shown in Figure 4.1. Further increases in load are generally required to keep the plastic flow and an increase in displacement; this phenomenon is known as strain-hardening. However, the material plastic behaviour is not simple. The stress remains constant at the yield point once yield is occurred for an elastic- plastic material. For elastic-plastic material with hardening, the plastic deformation is influenced by the continuously increase of the stress after the yield point is reached (Pun, 2014).

4.1.2 Material behavior under cyclic loading

The responses of a material under cyclic loading can be categorized into four different levels, purely elastic, elastic shakedown, plastic shakedown (cyclic plasticity) and ratcheting (which are illustrated in Figure 4.2). First, a material response elastic behavior when the amount of applied load is lower than its elastic limit. If the amount of applied load exceeds the elastic limit, a plastic flow, which occur in the first loading cycles, will create residual stresses and strain-harden the material. This hardening process will resist plastic flow that occurs in subsequent loading cycles and enable the component to *shakedown* to perfectly elastic state again: so, called the *elastic shakedow*n. As the component is loaded further beyond the elastic shakedown limit and the stress-strain path forms a closed loop, *plastic shakedown* is achieved. Finally, plastic deformation will start to accumulate under cyclic loading when a stress level exceeds the plastic shakedown limit

or ratcheting threshold. If accumulation of plastic deformation continues for each cycle load, the material behaviour is considered to be *ratcheting*. The rate of strain accumulation continuously decreases with increasing number of cycles, indicating material response towards a steady state. The loop traced by the unloading and reloading is called a hysteresis loop (Ringsberg, 2000; Tangtragulwong, 2012).

The rail-wheel material undergoes cyclic plasticity due to higher loading and unloading conditions and this leads to plastic deformation, which impossible to prevent. Under cyclic loading, the rail-wheel material shows a complex mechanical response with plastic deformation. The ratcheting response of the rail steel is important as it leads to surface and subsurface damage accumulation. In the framework of cyclic plasticity, many advanced elastoplastic constitutive models have been developed to predict cyclic deformation of the rail steel and a number of these cyclic models have been included with finite element software packages (Athukoralaa et al., 2017).

In Figure 4.2 (which is adapted from (Cvetkovski, 2012)), (a) shows purely elastic loading (below the elastic limit), (b) shows initial strain hardening and elastic shakedown, (c) Initial strain hardening and plastic shakedown, and (d) shows cycle dependent creep, i.e. ratcheting, build-up of plastic strain with each load.

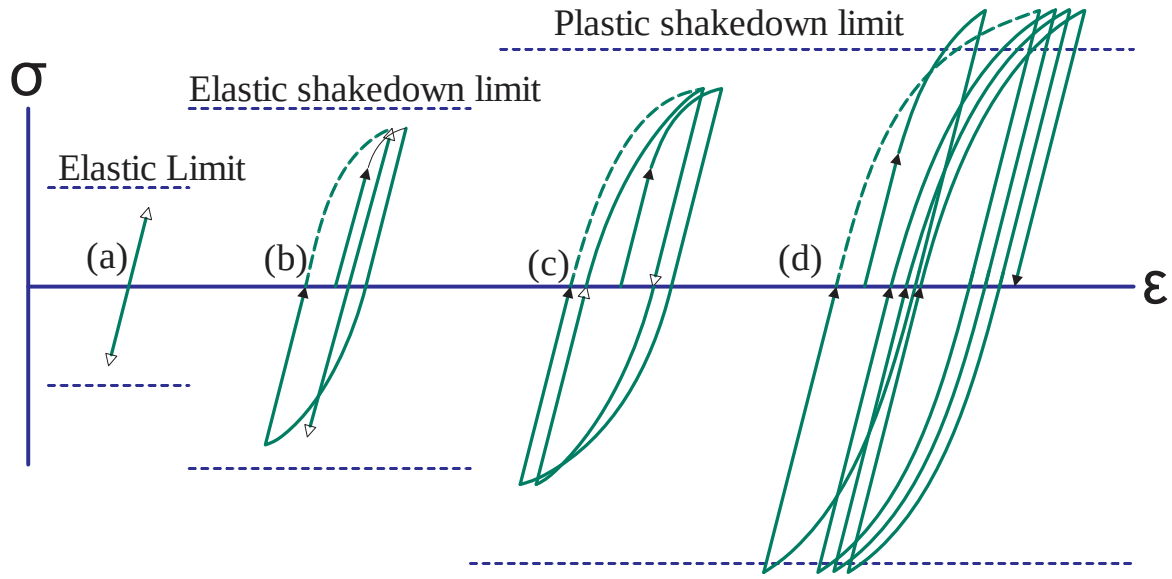

Figure 4.2 Material response to cyclic loading

4.2 Cyclic Elastoplastic Deformation

Since the rails and wheels are often subjected to cyclic stresses, it is very essential to study the cyclic stress–strain response of the materials. The material response depends on the test control modes and prior history of deformation. There are two types of cyclic load testing modes. These are the strain (deformation)-controlled and the stress (load)-controlled. These control modes are often used to investigate ratcheting behavior of the material. These two distinctive controlled modes are frequently used to examine the cyclic elastoplastic deformation of ductile materials in experiment. Under these controlled modes, different cyclic stress–strain responses are observed. The essential features of elasto-plastic deformation include cyclic hardening or softening or stable, cyclic mean stress relaxation, and ratcheting (Kang and Kan, 2017).

4.2.1 Cyclic hardening/softening feature

As clearly shown in Figure 4.3, the deformation characteristics of material under uniaxial strain control mode can be described from the relationship between the number of loading cycles N, and stress amplitude σ_a, (Jerome Pun, 2014). Under the symmetrical uniaxial strain-controlled cyclic loading conditions as shown in Figure 4.4 ‘a’ and ‘b’, the peak and valley strains do not change with the increasing number of cycles since they are prescribed as the controlled mode, while the responding peak and valley stresses may vary during the cyclic loading (Halama et al., 2012). Properties of cyclic hardening and softening depend on microstructure and stress amplitude of materials.

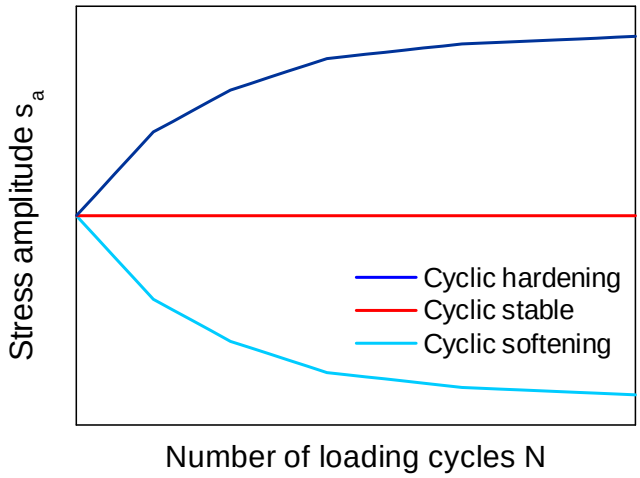

Figure 4.3 Deformation characteristic of materials subjected cyclic loading

The stress amplitude, σ_a in each cycle can be determined as:

$$\sigma_a = \frac{1}{2}(\sigma_{\max} - \sigma_{\min}) \tag{4.1}$$

Where, σ_{max} is maximum axial stress and $\sigma_{\min}$ is minimum axial stress.

- **Cyclic softening:** The responding stress amplitudes decrease with the number of loading cycles N (as shown in Figure 4.3 and Figure 4.4a].
- **Cyclic hardening**: the responding stress amplitudes of the materials increase with the number of loading cycles N (as shown in Figure 4.3 and Figure 4.4b).
- **Cyclic stabilizing**. The responding stress amplitudes do not change with the cyclic number N (as shown in Figure 4.3)

There are changes of the stress response and physical properties in the material at the beginning phase of cyclic loading due to micro structural changes. Cyclic hardening and softening effect relate to hardening and softening of material response or increasing and decreasing of resistance against material deformation under cyclic loading. Until the saturated state is reached, the intensity usually decreases as the number of loading cycles increase.

4.2.2 Mean stress relaxation

Under the asymmetrical strain-controlled cyclic loading conditions (i.e., the applied mean strain ε_{mean} is not zero), the responding mean stress may decrease with the increasing number of cycles and such phenomenon is called mean stress relaxation. The mean stress can be fully or partially relaxing with continuous cyclic loading and the rate of mean stress relaxation is dependent on the magnitude of the plastic strain amplitude.

This phenomenon can be observed by illustrating the relationship between the mean stress σ_m, in each loading cycle and the cyclic number *N*. The mean stress can be calculated as:

$$\sigma_{mean} = \frac{1}{2}(\sigma_{max} + \sigma_{min}) \tag{4.2}$$

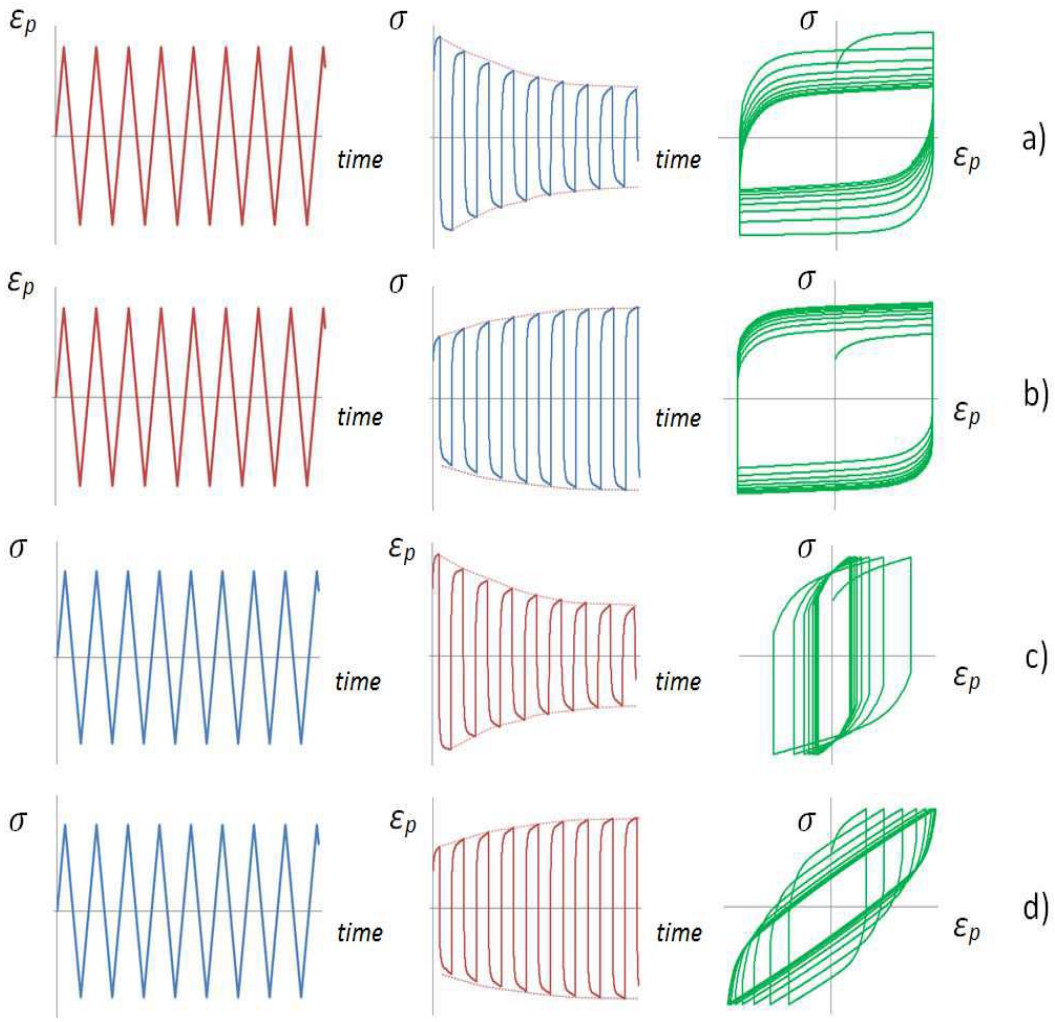

Figure 4.4 Uniaxial fatigue test material response

4.2.3 Ratchetting

Ratcheting is simply defined as an accumulation of plastic strain with cycles. Under the stress-controlled cyclic loading conditions, the peak and valley stresses do not change with the increasing number of cycles since they are prescribed as the controlling factors, while the responding peak and valley strains may vary during the cyclic loading, especially for the cases with nonzero mean stresses. During the stress-controlled cyclic loading with nonzero mean stress, a cyclically accumulation of inelastic deformation will occur in the materials mainly in the direction of mean stress if the applied stress level is high enough (e.g., higher than the yield strength of the materials), which is called as ratchetting. Ratcheting deformation occurs in such a way that the hysteresis loops produced for subsequent cycles translate towards higher plastic strain direction (Divya Bharathi, 2015; Kang and Kan, 2017; Pun, 2014).

Under unsymmetrical stress-controlled cyclic loading, the induced cycle of plastic stress-strain (hysteresis) loops never close and the strain gradually accumulates, i.e. strain ratcheting occurs (see Figure 4.5).

Generally, the hardening/softening behavior of a material under stress-controlled cyclic loading can be measured by the ratcheting strain and the ratcheting strain rate. Ratchetting strain is defined as the increment of peak strain (or mean strain) after each cycle (Kang and Kan, 2017).

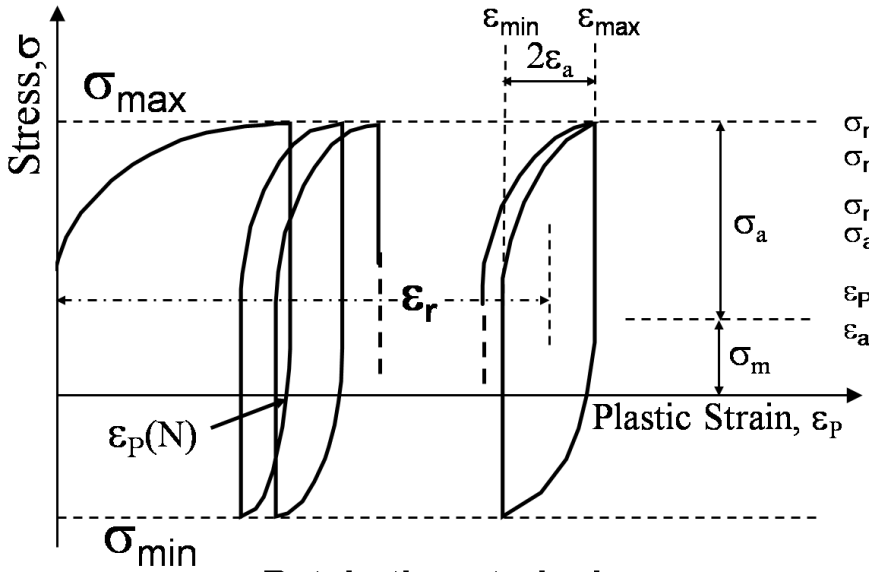

Figure 4.5 Schematic illustration of ratcheting

Due to the unclosed hysteresis loop produced under asymmetric stress cycling, the axial ratcheting strain ε_r and the torsional ratcheting strain γ_r in each cycle are defined as,

$$\varepsilon_r = \frac{1}{2}(\varepsilon_{\max} + \varepsilon_{\min}) \tag{4.3}$$

$$\gamma_{mean} = \frac{1}{2}(\gamma_{\max} + \gamma_{\min}) \tag{4.4}$$

Where; ε_r is ratcheting axial strain, ε_{max} is maximum axial strain at a particular cycle, $\varepsilon_{\min}$ is minimum axial strain at the cycle, $\gamma_{\max}$ is maximum of shear strain, and $\gamma_{\min}$ is minimum of shear strain.

Ratcheting strain rates are then defined as $\frac{d\varepsilon_r}{dN}$ and $\frac{d\gamma_r}{dN}$ which are the increment of ratcheting strains ε_r and γ_r per cycle. The ratcheting behavior of the materials under different loading conditions can be shown by the curve of ratcheting strain and ratcheting strain rate versus number of loading cycles N. When a material subjected to stress-controlled cyclic loading, three possible types of ratcheting behavior can be observed from the curve of ratcheting strain versus number of loading cycles as shown in Figure 4.6 (Jerome Pun, 2014)].

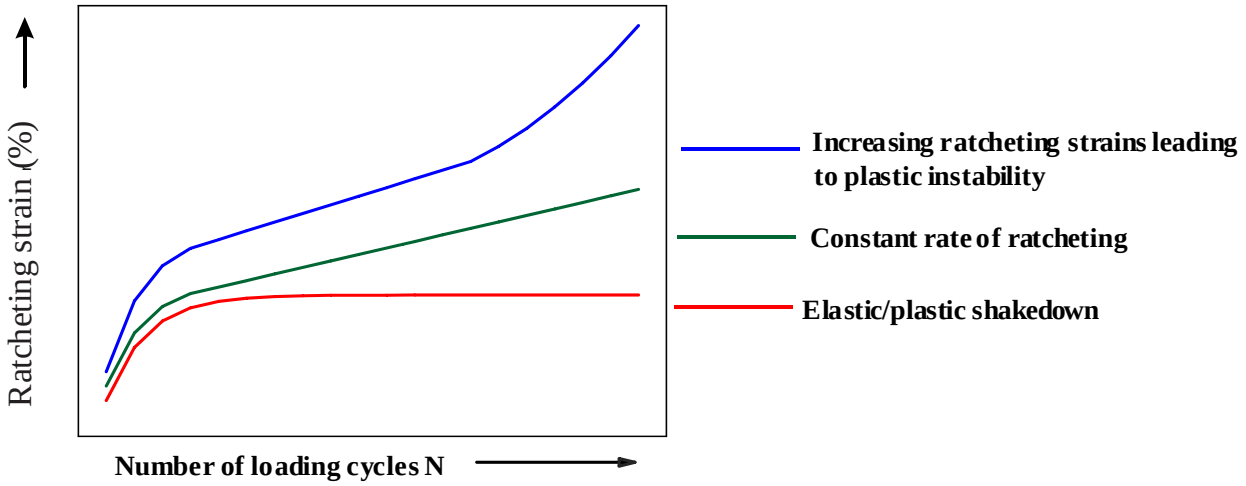

Figure 4.6 Ratcheting behavior when subjected to stress-controlled loading

The first type of ratcheting behavior is that the decreasing ratcheting strain rate leading to elastic/plastic shakedown under cyclic loading. This reveals that there is no further ratcheting takes place as shown in the red line in Figure 4.6. The second type is known as constant rate of ratcheting. The ratcheting strain increases with the number of loading cycle while the ratcheting strain rate decreases with the increase of cyclic number and finally reaches a stabilized value as illustrated by the green line in Figure 4.6.

The third type is the most unstable type of ratcheting behavior and can lead to large ratcheting strains, plastic instability and fracture due to the increasing/changing ratcheting strain rate throughout the fatigue life of the material as illustrated by the blue line in Figure 4.6. In general, this type of ratcheting behavior leads to a very low number of cycles to failure, which is known as very low cycle fatigue. Recent studies have already shown that the ratcheting behavior is significantly influenced by the loading conditions. For example, a material can have a constant

rate of ratcheting under relatively low cyclic loading conditions but have the plastic instability behavior under high cyclic loading conditions (Kang and Gao, 2002)

Under stress-controlled cyclic loading tests, the deformation characteristics of the material can also be investigated by observing the relationship between the strain amplitude ε_a in each cycle and the cyclic number *N*. If the strain amplitude increases with the cyclic number, the material softens under stress cycling. In contrast, the material hardens under stress cycling if the strain amplitude decreases with the increase of the cyclic number. The strain amplitude, ε_a is defined by,

$$\varepsilon_a = \frac{1}{2}(\varepsilon_{\max} - \varepsilon_{\min}) \tag{4.5}$$

4.3 Constitutive Modeling

Constitutive model defines the stress –strain response of material in mathematical ways, which is also called plastic model. Depending on the variables used and the extent to which the material model represents real behaviour, they can vary from simple elastic material behaviour to complex plastic material behaviour. FE software incorporates any of these constitutive models and during the analysis, the constitutive equations define the stress-strain behaviour of each element depending on the material model selected, the material parameters and the load applied (Munidasa et al., 2013).

The theory of plasticity includes four fundamental concepts: the decomposition of strain, yield criterion, plastic flow rule, and strain hardening rule. Yield criterion identifies when yield is initiated. Plastic flow rule defines the direction of plastic strain or plastic strain increment. Strain hardening rule defines how the yield surface evolves during plastic loading. These fundamental concepts are described in the following sections.

4.3.1 Strain decomposition

Figure 4.7 shows an idealized stress-strain behavior which might be obtained from a purely uniaxial tensile test. Initially, when the material is subjected to loading, it exhibits elastic behavior which means an increment of strain $d\varepsilon$ causes a proportional increment of stress $d\sigma$ where the proportionality constant is defined as the modulus of elasticity, E. When the stress reaches a certain threshold limit σ_y (named 'yield stress'), plasticity occurs. If a further increment of strain induces

an increment of stress compared to the perfect plastic behavior, the phenomena is called hardening because the stress is increasing relative to perfect plastic behavior.

If the loading is reversed, the material stops to deform plastically and shows a linearly decreasing stress with strain such that the slope of this part of the stress–strain curve again becomes the modulus of elasticity, E, shown in Figure 4.7 (After (Dunne and Petrinic, 2005)). Once a stress reaches zero value, (provided the material remains elastic on full reversal of the load, the strain that has not been recovered is the plastic strain, ε^p and the recovered strain is the elastic strain, ε^e. Therefore, the total strain can be decomposed in the elastic strain and plastic strain as follows:

$$\varepsilon = \varepsilon^e + \varepsilon^p \tag{4.6}$$

The stress value at a strain of ε is given by:

$$\sigma = E\varepsilon^e = E\left(\varepsilon - \varepsilon^p\right) \tag{4.7}$$

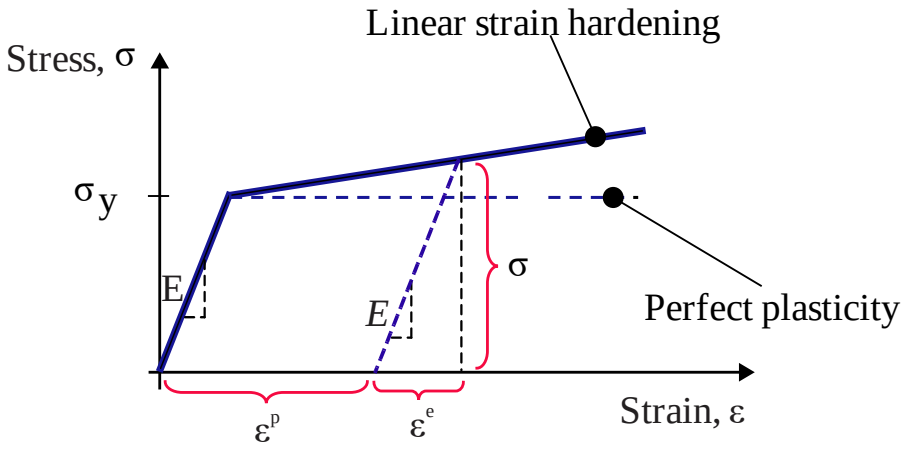

Figure 4.7 The classical decomposition of strain into elastic and plastic parts

4.3.2 Effective stress and plastic strain rate

The most commonly used effective stress is von-Mises stresses, sometimes called equivalent stress. Von-Mises described effective stresses in terms of principal stresses, or in terms of direct and shear stresses. In terms of principal stresses, the effective stress is defined as

$$\sigma_{eff} = \sqrt{\frac{1}{2}\left[(\sigma_1 - \sigma_2)^2 + (\sigma_2 - \sigma_3)^2 + (\sigma_3 - \sigma_1)^2\right]} \tag{4.8}$$

Where, σ_1, σ_2 and σ_3 are principal stresses.

In terms of direct and shear stresses, the effective stress is defined as

$$\sigma_{eff} = \sqrt{\frac{1}{2}\left[\left(\sigma_x - \sigma_y\right)^2 + \left(\sigma_x - \sigma_z\right)^2 + \left(\sigma_y - \sigma_z\right)^2 + 6\left(\tau_{xy} + \tau_{yz} + \tau_{xz}\right)\right]} \tag{4.9}$$

In cases of plane stress, Mohr's circle gives the maximum shear stress in that plane as half the difference of the principal stresses:

$$\tau_{\max} = \left(\frac{\sigma_1 - \sigma_2}{2}\right) \tag{4.10}$$

An effective plastic strain rate $\dot{p}$, is defined, similarly, as

$$\dot{p} = \frac{\sqrt{2}}{3}\left[\left(\dot{\varepsilon}_1^p - \dot{\varepsilon}_2^p\right)^2 + \left(\dot{\varepsilon}_2^p - \dot{\varepsilon}_3^p\right)^2 + \left(\dot{\varepsilon}_3^p - \dot{\varepsilon}_1^p\right)^2\right]^{\frac{1}{2}} \tag{4.11}$$

Stress and strain rate tensors in three dimensions are defined by means of second order tensors:

$$\sigma = \begin{pmatrix} \sigma_{11} & \sigma_{12} & \sigma_{13} \\ \sigma_{21} & \sigma_{22} & \sigma_{23} \\ \sigma_{31} & \sigma_{32} & \sigma_{33} \end{pmatrix} \tag{4.12}$$

$$\dot{\varepsilon} = \begin{pmatrix} \dot{\varepsilon}_{11} & \dot{\varepsilon}_{12} & \dot{\varepsilon}_{13} \\ \dot{\varepsilon}_{21} & \dot{\varepsilon}_{22} & \dot{\varepsilon}_{23} \\ \dot{\varepsilon}_{31} & \dot{\varepsilon}_{32} & \dot{\varepsilon}_{33} \end{pmatrix} \tag{4.13}$$

The plastic behavior of materials is often independent of a hydrostatic stress and this feature necessitates the study of the deviatoric stress. Any state of stress can be decomposed into a hydrostatic (or mean) stress σ_m I and a deviatoric stress s, according to

$$\begin{pmatrix} \sigma_{11} & \sigma_{12} & \sigma_{13} \\ \sigma_{21} & \sigma_{22} & \sigma_{23} \\ \sigma_{31} & \sigma_{32} & \sigma_{33} \end{pmatrix} = \begin{pmatrix} \sigma_m & 0 & 0 \\ 0 & \sigma_m & 0 \\ 0 & 0 & \sigma_m \end{pmatrix} + \begin{pmatrix} s_{11} & s_{12} & s_{13} \\ s_{21} & s_{22} & s_{23} \\ s_{31} & s_{32} & s_{33} \end{pmatrix} \tag{4.14}$$

With,

$$\sigma_m = \frac{\sigma_{11} + \sigma_{22} + \sigma_{33}}{3} \tag{4.15}$$

$$\begin{pmatrix} s_{11} & s_{12} & s_{13} \\ s_{21} & s_{22} & s_{23} \\ s_{31} & s_{32} & s_{33} \end{pmatrix} = \begin{pmatrix} \frac{1}{3}(2\sigma_{11} - \sigma_{22} - \sigma_{33}) & \sigma_{12} & \sigma_{13} \\ \sigma_{21} & \frac{1}{3}(2\sigma_{22} - \sigma_{11} - \sigma_{33}) & \sigma_{23} \\ \sigma_{31} & \sigma_{32} & \frac{1}{3}(2\sigma_{33} - \sigma_{11} - \sigma_{22}) \end{pmatrix} \quad (4.16)$$

This shows that the deviatoric stress is the difference between the stress and the mean stress, σ_m.

$$s_{ij} = \sigma_{ij} - \sigma_m I \quad (4.17)$$

(Dunne and Petrinic, 2005), described the effective stress and plastic strain rate interms of deviatoric stress:

$$\sigma_{eff} = \sqrt{\left(\frac{3}{2} s : s\right)} - Y = 0 \quad (4.18)$$

$$\dot{p} = \left(\frac{2}{3}\dot{\varepsilon}^p : \dot{\varepsilon}^p\right)^{\frac{1}{2}} \approx \left(\frac{2}{3}\dot{\varepsilon} : \dot{\varepsilon}\right)^{\frac{1}{2}} \quad (4.19)$$

(Dunne and Petrinic, 2005; Facheris, 2014) stated that the plastic deformation satisfies the incompressibility condition (i.e. the deformation takes place without volume change). Therefore, the sum of the diagonal components of the plastic strain rate is zero:

$$\dot{\varepsilon}_{11}^{pl} + \dot{\varepsilon}_{22}^{pl} + \dot{\varepsilon}_{33}^{pl} = 0 \quad (4.20)$$

4.3.3 Yield criteria

First it is important to establish criteria that will predict the onset of inelastic deformation in order to describe the relationship between the stress and plastic strain. Yield criteria defines the limit of elasticity and the beginning of plastic deformation under any possible combination of stresses. In the elastic region, all the deformation will be recovered once the applied stress is removed (i.e. unloading of stress to zero). However, once the yield condition is reached, some of the deformation will be permanent in the sense that it cannot be recovered even after the stress is removed completely. This part of the deformation is known as plastic deformation and the remaining deformation is recoverable upon removal of the stress and is known as elastic deformation.

Generally, yield criteria determine the stress level at which yielding is initiated. Plastic behavior of homogeneous, isotropic materials can be represented by a yield function:

$$F\left(\sigma_{ij},\sigma_{y}\right)=f\left(\sigma_{ij}\right)-\sigma_{y} \tag{4.21}$$

Where, $f\left(\sigma_{ij}\right)=\sigma_{eff}$, effective stress, which depends on the stress tensor and σ_{y} – material yield parameter.

Yield function divides the whole stress space into two: elastic and plastic domains**.** When the stress state is within the yield surface, material behavior is said to be elastic. Once the stress state is on the yield surface, plastic deformation will be produced.

Three possible cases of stress state can occur:

- $f\left(\sigma_{ij}\right)<\sigma_{y}$, (i. e. the equivalent stress is lower than material yield) In this case, $F\left(\sigma_{ij},\sigma_{y}\right)<0$. The stress state point is inside the yield surface and material behaves elastically (no plastic strains occur).
- $f\left(\sigma_{ij}\right)=\sigma_{y}$, the equivalent stress is equal to material yield (i.e. $F\left(\sigma_{ij},\sigma_{y}\right)=0$, plastic deformation or yielding). Stress state point lies on the yield surface.
- $F\left(\sigma_{ij},\sigma_{y}\right)>0$, plastic behavior of material occurs. However, this option is not possible since equivalent stress can never exceed the material yield because plastic strains would in that case develop instantaneously in order to reduce the stress to material yield. Thus, stress state point can only lie **on** the yield surface, so if the stress state tends to move outside the surface, the yield surface "moves" along. This behavior is described by hardening rule (Basan, 2016).

Therefore, the yield criterion is defined as: $F\left(\sigma_{ij},\sigma_{y}\right)\leq 0$

It is well known that von-Mises and Tresca yield criteria are the two commonly used yield criteria for predicting the onset of yielding in ductile materials. For this thesis, the yield is assumed to be independent of hydrostatic pressure.

A. Von-Mises yield criterion

(Von Mises, 1913) proposed the most commonly used yield criterion for ductile materials. This yield criterion states that plastic yielding occurs when the distortion energy per unit volume reaches the distortion energy per unit volume in a uniaxial tensile test at the yield point (Behravesh, 2013). The von Mises yield criteria (also called von-Mises equivalent stress) in terms of principal stresses can be defined as:

$$\sqrt{\frac{1}{2}\left[(\sigma_1-\sigma_2)^2+(\sigma_2-\sigma_3)^2+(\sigma_3-\sigma_1)^2\right]}=\sigma_y \tag{4.22}$$

According to this criterion, the yield function is can be described in terms of deviatoric stress:

$$F\left(\sigma,\sigma_y\right)=\sqrt{\frac{3}{2}s:s}-\sigma_y \tag{4.23}$$

B. Tresca yield criterion

The Tresca yield criterion was developed to predict the onset of yielding in metal materials. (Tresca, 1869) stated that plastic deformation begins when the maximum shear stress $\tau_{\max}$ reaches half of the yield stress for the material. In the case of uni-axial tensile loading, where σ_1 equals the applied tensile stress and $\sigma_2 = \sigma_3 = 0$. Yielding will occur when σ_1 reaches the yield stress σ_y for the material being tested. Generally, Tresca yield criterion in terms of principal stresses can be stated as:

$$\tau_{\max}=\frac{1}{2}(\sigma_1-\sigma_3)=\frac{1}{2}\sigma_y \tag{4.24}$$

Where σ_1 and σ_3 are the maximum and minimum principal stresses for Eq. (4.24).

4.3.4 Flow rule

The material starts to deform plastically, when the yield surface is reached. Upon further loading, the deformation produces plastic flow. The flow rule determines how the material deforms plastically after reaching the yield surface. The kinematic hardening models assume associated plastic flow:

$$\dot{\varepsilon}^{pl}=\dot{\bar{\varepsilon}}^{pl}\frac{\partial F}{\partial \sigma} \tag{4.25}$$

Where, $\dot{\varepsilon}^{pl}$ is the rate of plastic flow and $\dot{\bar{\varepsilon}}^{pl}$ is the equivalent plastic strain rate. The evolution of the equivalent plastic strain is obtained from the following equivalent plastic work expression:

$$\dot{\bar{\varepsilon}}^{pl} = \sqrt{\frac{2}{3}\dot{\varepsilon}^{pl} : \dot{\varepsilon}^{pl}} \tag{4.26}$$

which yields $\dot{\bar{\varepsilon}}^{pl} = \sqrt{\frac{2}{3}\dot{\varepsilon}^{pl} : \dot{\varepsilon}^{pl}}$ for isotropic Mises plasticity. The assumption of associated plastic flow is acceptable for metals subjected to cyclic loading as long as microscopic details, such as localization of plastic flow occurring as a metal component ruptures due to cyclic fatigue loads (Systèmes, 2007).

4.3.5 Hardening rules

The rule which describe the condition for establishing the subsequent yielding behavior once the initial yielding has occurred is known as hardening rule. In short, it describes how the yield surface changes with plastic deformation. A point in stress space never lie outside of the yield surface as described in section 4.3.3, it follows that the yield surface has to change its size or position (even shape) for further yielding to occur. Based on the developed stress under loading, the material can undergo kinematic hardening and/or isotropic hardening (Munidasa et al., 2013).

A. Isotropic hardening

Isotropic hardening rule assumes that the yield surface remains the same shape but expands uniformly in all direction during plastic deformation (as shown on Figure 4.8) In other words, the yield surface expands without translation under plastic loading. In isotropic hardening the tensile and compressive yield strength are initially the same and remain constant if the yield surface is symmetric about the stress axes and remains constant. This implies that the isotropic hardening model cannot model the Bauschinger effect in which the yield stress in compression is significantly reduced when it is unloaded from tensile state (Athukorala, 2016). Therefore, isotropic hardening rule is not appropriate hardening rule to model materials subjected to cyclic loading.

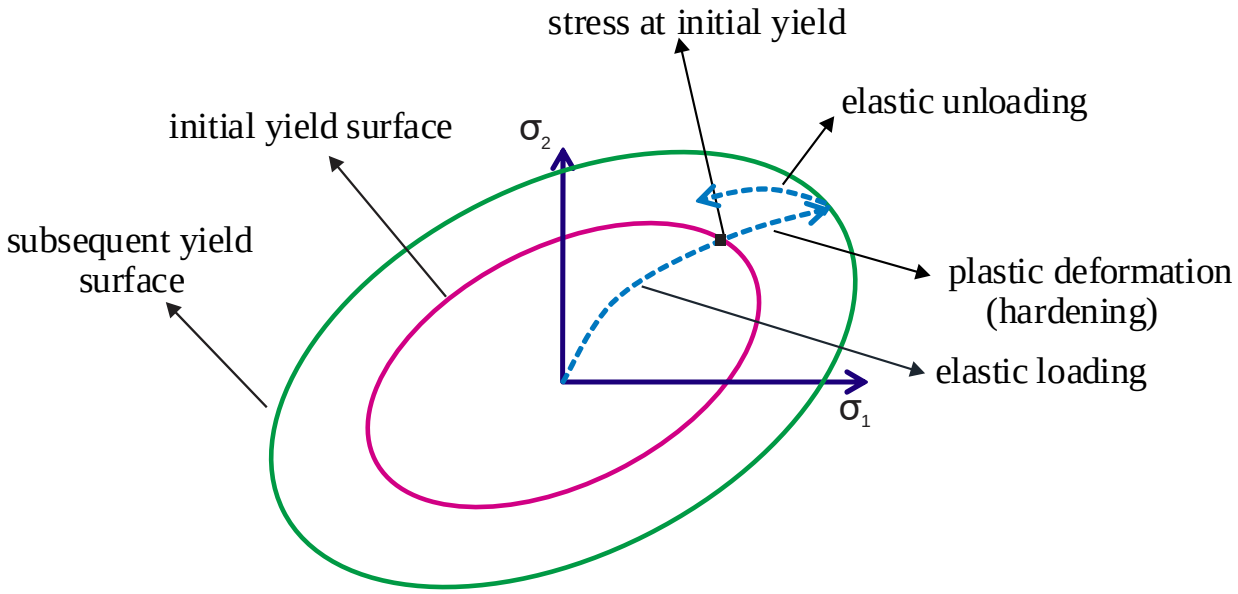

Figure 4.8 Isotropic hardening yield surface

B. Kinematic hardening

In the kinematic hardening rule, the yield surface translates its position in the stress space without changing its shape and size during the plastic flow (see Figure 4.9). This hardening rule was proposed to account the Bauschinger effect observed during loading and unloading. The use of kinematic hardening rules involves the modification (shifting) the stress tensor σ with the so-called back-stress (or translation) tensor α, in the yield function. Thus, the yield function becomes $F\left(\sigma-\alpha,\sigma_y\right)$. Depending of the evolution of the back-stress tensor, a few kinematic hardening models exist.

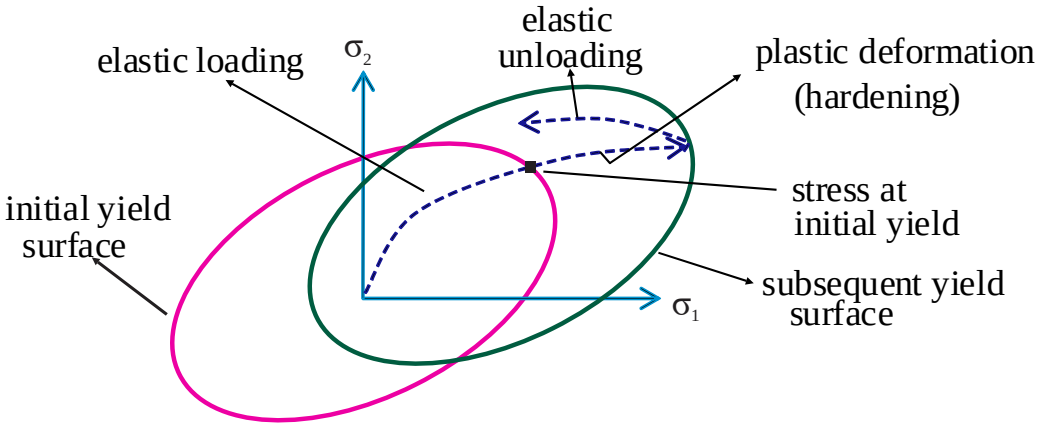

Figure 4.9 Kinematic hardening yield surface

i. Linear Kinematic Hardening Model

Linear kinematic hardening models are among the first-developed constitutive models and were a simplification during the early days of plasticity theory and modelling (Munidasa et al., 2013). One of the most known linear kinematic hardening model is Prager rule. (Prager, 1956) developed a linear kinematic hardening model for evolution of the back stress, $\underline{a}$, in which the yield surface translates along the plastic strain increment tensor, $\underline{\varepsilon}^p$. The constitutive equation for this hardening rule is of the form.

$$d\underline{a} = c_p . d\underline{\varepsilon}^p \tag{4.27}$$

This rule described the linear changes in yield surface in the stress-strain plane during the uniaxial loading and unloading process. Due to its linear behaviour, this Linear kinematic hardening model produces the closed hysteresis loops, which is not appropriate for the realistic behaviour of the ratchetting phenomenon. Therefore, it is not suitable to model the ratcheting behaviour of the material subjected to cyclic loading like rail and wheel contact.

ii. Nonlinear Kinematic Hardening Models

In order to minimize the difference between material behaviour in the plastic region in linear models and practical scenarios, nonlinear hardening models were developed.

a) ***Armstrong-Frederick Rule (A-F Rule)***

Armstrong-Frederick proposed the first nonlinear kinematic hardening rule, which is characterized by the ability to retain the strain history. This rule introduces a recall term as per Eq. 2-27 and is therefore capable of modelling ratchetting under cyclic loading. For this reason, the Armstrong-Frederick rule is the basis for most of the recent plasticity models and the advancements thereof. The recall term which incorporates the fading memory effect of the strain path makes the rule nonlinear in nature, i.e.

$$d\underline{a} = \frac{2}{3} C . d\underline{\varepsilon}^p - \gamma \underline{a} . dp \tag{4.28}$$

where C and γ are material parameters and dp (the recall term to retain the strain history) defined as

$$dp = \left[\frac{2}{3} d\underline{\varepsilon}^{p} . d\underline{\varepsilon}^{p} \right]^{\frac{1}{2}} \tag{4.29}$$

The capability of keeping the strain history enhances the model's realism relative to the experimental behaviour of the materials in the plastic range. Moreover, this is the first kinematic hardening model which is capable of describing the Bauschinger effect as in Figure 2-10. That is, if a load specimen is loaded under uniaxial tension beyond the yield stress and then unloads and reloads under uniaxial compression, the new yield stress in compression is going to be smaller in magnitude than the original yield stress in tension.

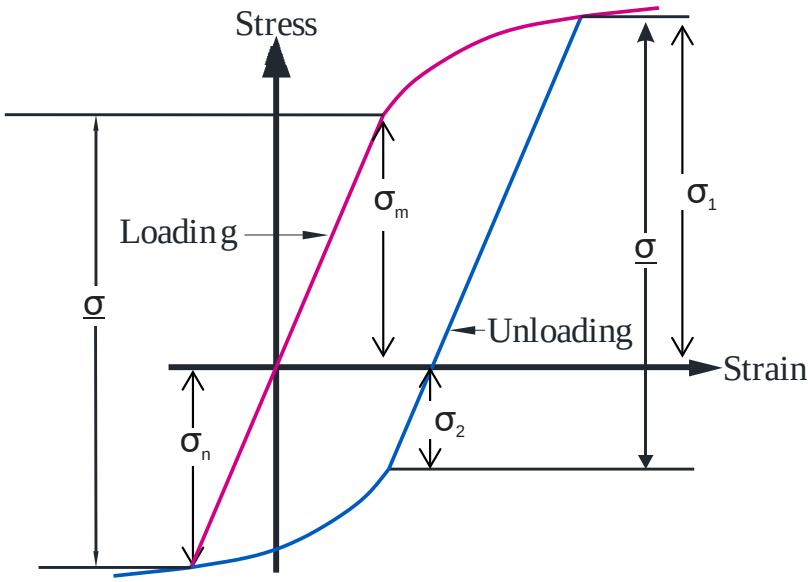

Figure 4.10 Stress-plastic strain A-F rule under uniaxial loading.

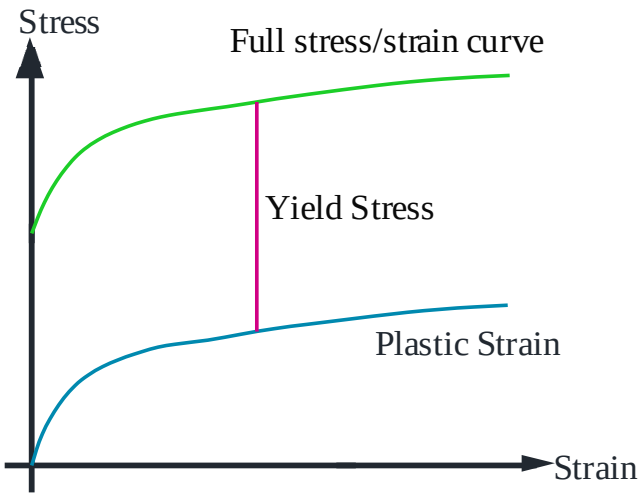

Figure 4.11 Stress-strain representation of A-F rule.

From the Figure 4.10, $\sigma_m > \sigma_n$ and $\sigma_1 > \sigma_2$. Which means yield stress tension is greater than yield stress compression. This rule has a distinct advantage over the linear models because it identifies the difference between the loading and unloading paths. Due to the recall term, it produces changes in shape between forward and reverse loading paths. Therefore, the loop does not close as per the linear models and results in ratchetting material behaviour under cyclic loading.

Even though there are some doubts about the accuracy of the predicted results from the A-F rule, modification to this model by several researchers has been widely used for developing constitutive equations for describing material plasticity behaviour.

b) Chaboche model

The Chaboche nonlinear kinematic model is the first of many modified versions of the Armstrong-Fredric (A-F) rule (Munidasa et al., 2013). For the Chaboche plasticity model, the von-Mises equivalent stress is the yield criterion, which is defined as:

$$\sqrt{\frac{2}{3}\left(S-\alpha^{dev}\right):\left(S-\alpha^{dev}\right)}-\sigma^{o}=0 \tag{4.30}$$

Where, S is the deviatoric stress tensor, α^{dev} is the deviatoric component of the back-stress tensor and σ^{o} is the yield stress.

(Chaboche, 1991) proposed nonlinear isotropic kinematic hardening rule with one back-stress term consists of two components.

The first component is the nonlinear kinematic hardening part, which describes a translation of yield surface in stress space, observed as the *Bauschinger effect* in cyclic loading tests, through the backstress tensor (α). The second component is the isotropic hardening part, which describes the uniform change of a yield surface as a function of plastic deformation. These two hardening components together will predict a cyclic material hardening, and a ratcheting and its decaying rate.

The isotropic hardening rule of the plasticity model defines evolution of the yield surface size (σ^0) as a function of the equivalent plastic strain (ε^{-pl}). This can be defined by exponential law as follows:

$$\sigma^0 = \sigma\big|_0 + Q_\infty \left(1 - e^{-b\varepsilon^{-pl}}\right) \tag{4.31}$$

Where, σ^0 is the yield stress at zero plastic strain, Q_∞ is the maximum change in size of the yield surface, and b is the rate at which size of the yield surface changes as the plastic straining develops.

The nonlinearity of the kinematic hardening component is introduced through a recall term, which is added to a purely kinematic term (the linear *Ziegler hardening law*). The nonlinear kinematic hardening rule with a back-stress term in temperature-independent condition is:

$$d\underline{a} = \sum_{i=1}^{3} d\underline{a}_i = \sum_{i=1}^{3} \left(\frac{2}{3} C_i . d\underline{\varepsilon}^p - \gamma_i \underline{a}_i . dp \right) \tag{4.32}$$

Here, where dp is accumulated plastic strain, and C_i (for i=1,2,3) and γ_i (for i=1,2,3) are material constants: those need to be calibrated in using stress- and strain-controlled data.

4.3.6 Material model parameters for FE model

The objective of this section is to identify a suitable material model parameter for the rail-wheel finite element model. An elastic-plastic material subjected to cyclic loading are modelled by coupled isotropic and kinematic hardening models (Systèmes, 2007). In rail-wheel contact which subjected to cyclic loading, the material is expected to exhibit nonlinear isotropic/kinematic hardening plasticity behaviour.

In this thesis, the nonlinear kinematic cyclic hardening model, which incorporated with nonlinear isotropic hardening, was selected to define material plasticity. In the model, there are various

material parameters ($Q\infty$, b, σ_{virgin}, C and γ) that need to be optimized. The material model parameters value that are optimized by (Schleinzer and Fischer, 2001) are used in this thesis for FE modelling. These material parameters are summarized in Table 4-1.

Table 4-1 Material model parameters for the rail-wheel

Material parameters	Values
σ_{virgin} (MPa)	379
Q_∞ (MPa)	189
$\gamma_1, \gamma_2, \gamma_3$	55, 600, 2000
b_m	500
C_1, C_2, C_3 (MPa)	24750, 60000, 200000

CHAPTER 5

RAIL WHEEL FATIGUE LIFE MODELLING

This chapter presents the approaches of predicting fatigue life of the rail wheel. The fatigue life of the rail wheel is the sum of the crack initiation life and propagation life. The finite element (FE) model is used to identify the area in which the probability of crack initiation is high based on the stress/strain distribution. Three fatigue model approaches have been used to determine crack initiation life. These fatigue models use the stresses and strains from the finite element model as an input. A fatigue overview and rolling contact fatigue are first presented. Then, the fatigue crack initiation and propagation life modelling are presented.

5.1 Fatigue Overview

Fatigue failure is a progressive failure of materials or components subjected to a cyclic stress, which is very dangerous because it occurs at stress level which is normally lower than the ultimate or yield stress of materials. It is estimated that 50% to 90% of components' failures are due to fatigue (Sladkowski and Sitarz, 2005). In order to predict the material resistance to fatigue failure, it is necessary to carry out the fatigue analysis.

There are three approaches of analyzing the fatigue life: 1) strain Life approach, 2) stress life approach and 3) fracture mechanics approach. Strain life mainly deals with the occurrence of a smaller number of fatigue cycle which is called low-cycle fatigue based on crack initiation. It also works for high cyclic fatigue. Whereas the stress life depends upon the total life and has nothing to do with the crack initiation. In case of stress life approaches, the material behaviour is predominantly assumed to be elastic and the material endures a high number of cycles so its application is restricted to high cyclic fatigue analysis. The third fatigue analysis approach is fracture mechanics, it is based on the crack initiation and its propagation up to sever effect and complete time taken to grow this crack up to critical condition is find out and this time taken is

called fatigue life. The concept of fatigue and fracture mechanics is purely based on empirical theory and formula, though it allows for prediction of life and design pledge, life prediction or optimization of design may be improved using fracture mechanics. In this chapter, fatigue crack initiation using strain life approaches and crack growth modelling using fracture approach are discussed in detail.

5.2 Rolling Contact Fatigue Model

The fatigue problem of rail wheel is often referred to as rolling contact fatigue and is caused by repeated contact stress during the rolling motion. To study the fatigue failure mechanism of rail wheel, considering the loading conditions to which the rail wheel may be subjected under rolling contact condition is very important. In wheel-rail rolling contact conditions, both the wheel and rail are subjected to nonproportional multiaxial stress state in which the direction of the principal stresses and strains change continuously during a passage of the wheel over the rail. The change in the orientation of principal stress axes permits more grains to align in their most favorable orientations for slip and increases the interaction between slip systems. This induces additional cyclic hardening of material with reduced fatigue life. Multiaxial fatigue models help to reduce the complexity involved in multi axial loading conditions (El-sayed et al., 2017; Srivastava et al., 2017). Therefore, a proper multiaxial fatigue model under non-proportional loading is required to analysis fatigue life of rail wheel.

In rail wheel rolling contact fatigue, damage is caused by changes in the material microstructure which results in crack initiation followed by crack propagation, under the influence of time dependent rolling and/or sliding contact loads. In general, rail wheel rolling contact fatigue process can be classified into three main stages, as shown in Figure 5.1 (After (Everaerts, 2017)..

1) Crack Initiation (nucleation); when micro-cracks are formed due to local accumulation of dislocations, high stresses at local points, plastic deformation around inhomogeneous inclusions or other imperfections in or under the contact surface;
2) crack propagation (crack growth): when the initiated cracks propagate and leads to final fracture. This stage causes permanent damage of mechanical element.
3) Failure (Fracture due to unstable crack propagation). After crack reaches critical dimension, one additional cycle causes sudden failure.

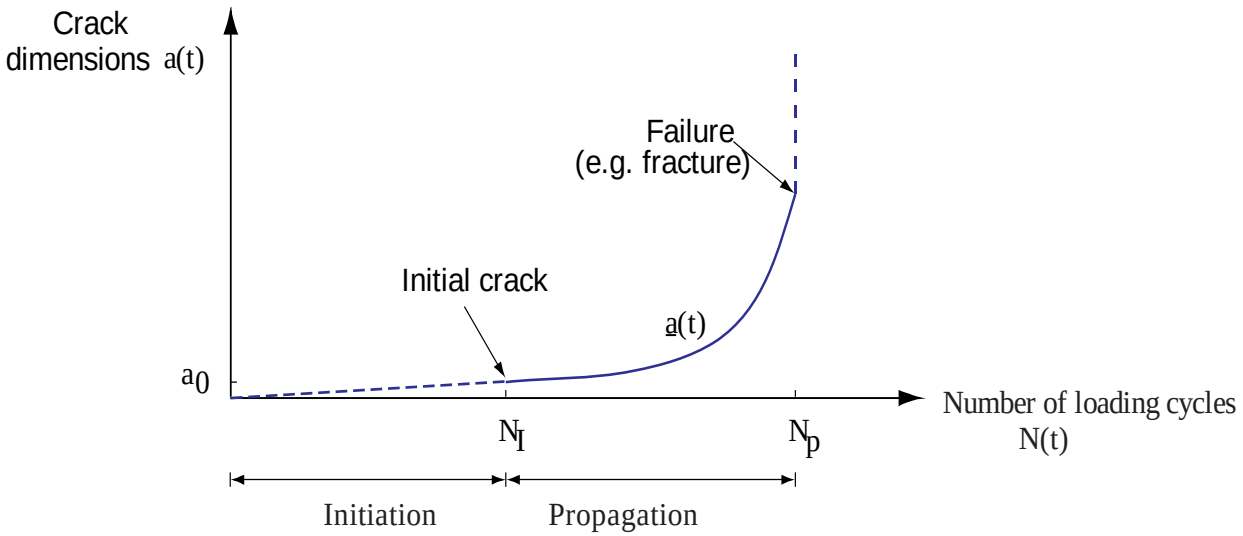

Figure 5.1 Three stages of fatigue crack growth schematically

Fatigue Life (N_f) is defined as the number of stress cycles or strain reversals that a material experiences prior to fracture. The total fatigue life of rail-wheel is the sum of the periods for crack initiation and the crack propagation. Mathematically, it can be expressed as

$$N_f = N_I + N_P \tag{5.1}$$

where N_f, N_I and N_p are the total fatigue life, number of cycles for crack initiation, and number of cycles for crack propagation, respectively.

5.3 Fatigue Crack Initiation Modelling

In this study, three multiaxial fatigue models which can predict both the fatigue crack initiation life and fatigue cracking plane orientation are used: (Sehitoglu and Jiang, 1992), (Smith et al., 1970), and (Fatemi and Socie, 1988). All of these models are categorized under strain life approaches.

5.3.1 Jiang and Sehitoglu model

In this study, a multiaxial fatigue model based on the energy–density and a critical plane approach, which was developed by (Sehitoglu and Jiang, 1992), was used. The critical plane approach is based upon the physical observation that fatigue cracks initiate and grow on certain material planes and the orientation of which is determined by both the stresses and strains at the critical location. In this criterion, both normal and shear components of stress

and strain, on the critical plane, contribute to the material fatigue. The model is expressed as,

$$FP = \langle \sigma_{\max} \rangle \frac{\Delta\varepsilon}{2} + J\Delta\tau\Delta\gamma \tag{5.2}$$

Where, $\langle\ \rangle$ denotes the McCauley bracket, $\langle \sigma_{\max} \rangle = 0.5\left(|\sigma_{\max}| + \sigma_{\max}\right)$; $\Delta\varepsilon$ is the normal strain range, $\sigma_{\max}$ is the maximum normal stress; $\Delta\gamma$ is the shear strain range, $\Delta\tau$ is the shear stress range and J is a material and load dependent constant. All the stress and strain quantities in Eq. (5.2) are on the critical plane (crack plane) where the fatigue parameter (FP) is maximum. Through a tensor rotation for the stresses and strains, $FP_{\max}$ and the corresponding critical plane are determined by surveying all the possible planes at a material point.

5.3.2 Smith-Watson-Topper (SWT) model

(Smith et al., 1970) proposed a multiaxial fatigue model for materials depending on the concept of critical plane. The main concept of this model is that the maximum normal stress σ_{nmax} and the normal strain amplitude $\frac{\Delta\epsilon}{2}$ acting at a critical plane are the driving forces of fatigue in materials. The critical plane is the plane in which the product of maximum normal stress ($\sigma_{n\max}$) and normal strain amplitude ($\frac{\Delta\varepsilon}{2}$) is maximum. The stress term in this model is used to describe multiaxial loading and non-proportional hardening. The mathematical description of this model is

$$FP_{SWT} = \sigma_{n\max} \frac{\Delta\varepsilon}{2} = f\left(N_i\right) \tag{5.3}$$

in which $f\left(N_i\right)$ is a function of the fatigue life N_i.

5.3.3 Fatemi-Socie (FS) model

(Fatemi and Socie, 1988), proposed a shear strain based multiaxial fatigue criteria that assumed the maximum shear strain amplitude acting at a material plane to be the driving force of the fatigue crack initiation. This model is a modification of the (Brown and Miller, 1973) model, which depended upon principal strains ε_1 and ε_3, to consider the effect of mean stress and non-proportional hardening by replacing the normal strain by the normal stress. This model can be described in mathematical form,

$$FP = \frac{\Delta\gamma_{\max}}{2}\left(1 + k\frac{\sigma_{n\max}}{\sigma_y}\right) = f\left(N_f\right) \tag{5.4}$$

Where, $\frac{\Delta\gamma_{\max}}{2}$ is the maximum shear strain amplitude, k is a material sensitivity factor, $\sigma_{n\max}$ is the maximum normal stress at the plane in which $\frac{\gamma_{\max}}{2}$ is maximum, σ_y is yield stress, and $f\left(N_f\right)$ is a function of the fatigue life.

In the original Fatemi and Socie (1988) modeling, critical plane was defined as the plane in which shear strain was maximum. This shows the critical plane depends on the maximum shear strain but not fatigue parameter. However, According to (Barros, 2018; Chu, 1995), the effect of the maximum strain/stress on the fatigue crack initiation should be considered for critical plane. Therefore, they defined the critical plane as the plane in which fatigue parameter is maximum. Thus, function of the fatigue crack initiation life can be described as:

$$f\left(N_f\right) = \left[\frac{\Delta\gamma_{\max}}{2}\left(1 + k\frac{\sigma_{n\max}}{\sigma_y}\right)\right]_{\max} \tag{5.5}$$

After the critical plane has been identified, the crack initiation life (N_I) can then be evaluated on the critical plane using Eq. (5.6) (El-sayed et al., 2017). This equation consists of two forms: tensile form and shear form. The formula that includes shear form is adopted to evaluate N_I if shear cracking governs the fatigue life. However, for material that exhibits tensile cracking, tensile form should be used. Both forms are given in Eq. (5.6).

$$FP_{\max} = f(2N_I) = \frac{(\tau_f^{'})^2}{G}(2N_I)^{2b} + \tau_f^{'}\gamma_f^{'}(2N_I)^{b+c}$$

$$FP_{\max} = \begin{cases} \dfrac{(\sigma_f^{'})^2}{E}(2N_I)^{2b} + \sigma_f^{'}\varepsilon_f^{'}(2N_I)^{b+c} \\ \dfrac{(\tau_f^{'})^2}{G}(2N_I)^{2b} + \tau_f^{'}\gamma_f^{'}(2N_I)^{b+c} \end{cases} \tag{5.6}$$

where $\sigma_f^{'}$, $\varepsilon_f^{'}$, $\tau_f^{'}$, $\gamma_f^{'}$, b and c are the material parameters.

5.4 Fatigue Crack Propagation Modelling

Fatigue crack propagation in railway wheel occurs as a due to cyclic loading conditions with cracks growing a given increment (Δa) in a given number of loading cycles (ΔN). When the crack size reaches a critical level, crack growth becomes unstable and failure occurs. According to linear elastic fracture mechanics (LEFM), the plastic deformation near the crack tip is controlled by the stress intensity factor range (ΔK_{eq}). The fatigue crack growth rate is typically represented with the nonlinear functional relationship (Shantz, 2010).

$$\frac{da}{dN} = \frac{\Delta a}{\Delta N} = f\left(\Delta K, R, K_{IC}, K_{th}, a....\right) \tag{5.7}$$

where da/dN is the crack growth rate per cycle, f is a non-negative function, ΔK is the range of the stress intensity factor, R is the ratio of the minimum to maximum applied loading, K_{IC} is the fracture toughness, K_{th} is the threshold stress intensity factor, and a is the crack length. Both fracture toughness K_{IC} and threshold stress intensity factor, K_{th} are material properties. The stress intensity factor (ΔK) is considered as the primary parameter, and is related to the applied loading, crack length, and geometry of the component. Fracture toughness (K_{IC}) is a material property that describes resistance of a material against the rapid or unstable crack growth. It may be obtained by test and used for determination of critical crack size (a_c) in wheel (Haidari and Tehrani, 2015; Shantz, 2010).

5.4.1 Modes of loading

A crack in a body may be subjected to three different types of loading, which are shown in Figure 5.2, Mode I is the tensile or opening mode, where the applied loading pulls apart the crack faces. Mode II is the sliding or in-plane sliding mode (faces are sheared backwards and forwards) and mode III is the tearing or anti-plane shear mode (faces are sheared sideways). In the rail wheel contact conditions, all of these three modes of loading may occur. Therefore, the rail-wheel is subjected to a mixed mode (mode I, mode II and mode III) multi-axial fatigue crack growth.

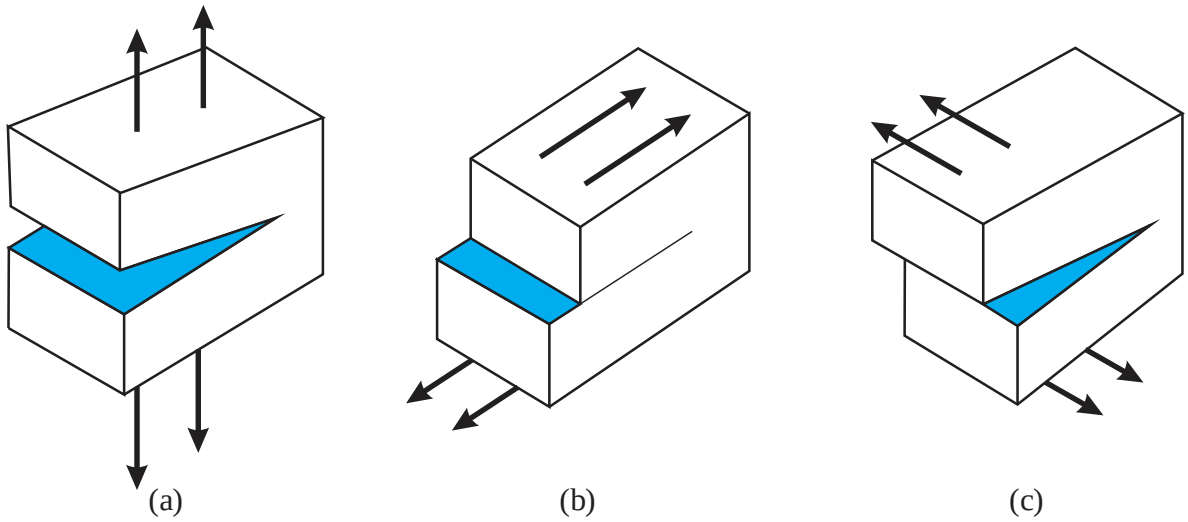

Figure 5.2 Illustration of the three fracture modes (a) mode I , (b) mode II and (c) mode III

Since crack growth is controlled by the stress field near the crack tip, accurate calculation of tress intensity factor plays an essential role in fracture mechanics. The stress intensity factor values at a crack tip subjected to remote loading conditions under different modes are given by Eq (5.8), (5.9) and (5.10) (Sura, 2011).

$$K_1 = \frac{2}{\pi}\sigma\sqrt{\pi a} \tag{5.8}$$

$$K_{II} = \frac{4}{\pi(2-\nu)}\sigma\sqrt{\pi a} \tag{5.9}$$

$$K_{III} = \frac{4(1-\nu)}{\pi(2-\nu)}\sigma\sqrt{\pi a} \tag{5.10}$$

Where, a = half crack size, *KI*, *KII*, and *KIII* are mode I, mode II, and mode III stress intensity factor values respectively, σ is the applied remote stress, and ν is the Poisson's ratio.

5.4.2 Mixed-mode fatigue crack growth

The rail-wheels subjected to non-proportional multiaxial loading conditions during cyclic loading (Liu et al., 2007). Thus, a mixed mode fatigue crack modelling approach which consider non-proportionality is required for railway wheel fatigue crack modelling. However, most of the existing mixed-mode crack growth modelling are limited to proportional loading and ignoring non-proportionality of loading condition. (Liu and Mahadevan, 2007) proposed a multiaxial fatigue model, which is appropriate for both proportional and non-proportional multiaxial loading

conditions, and has been validated by multiaxial fatigue experimental data. This modelling was used in this thesis.

5.4.2.1 Mixed mode equivalent stress intensity factor

The expression for a threshold mixed-mode crack model can be obtained by substituting Eq. (5.11) up to (5.13) in Eq. (5.14). A detailed derivation and explanation of the threshold mixed-mode crack model was outlined by (Liu and Mahadevan, 2007). The general fatigue limit criterion under multiaxial loading is expressed as

$$\sqrt{\left(\frac{\sigma_{a,c}}{f_{-1}}\right)^2+\left(\frac{\tau_{a,c}}{\tau_{-1}}\right)^2+A\left(\frac{\sigma^H{}_c}{f_{-1}}\right)^2}=B \tag{5.11}$$

Where, $\sigma_{a,c}$ is the normal stress amplitude on the critical plane, $\tau_{a,c}$ is the shear stress amplitude on the critical plane, $\sigma^H{}_c$ is the hydrostatic stress on the critical plane, f_{-1} is the tensile fatigue limit of a smooth specimen, t_{-1} is the shear fatigue strength of a smooth specimen, and *A* and *B* are material parameters.

According to (El Haddad et al., 1979) model, the fatigue limit can be described as a function of threshold stress intensity factor range and a fictional crack length *a*, which is shown in Eq. (5.12)-(5.13).

$$f_{-1}=\frac{\Delta K_{th,I}}{\sqrt{\pi a}} \tag{5.12}$$

$$\tau_{-1}=\frac{\Delta K_{th,II}}{\sqrt{\pi a}}\ \text{or}\ \tau_{-1}=\frac{\Delta K_{th,III}}{\sqrt{\pi a}} \tag{5.13}$$

Where, f_{-1} and t_{-1} are normal and shear fatigue limit, respectively and $K_{th,I}$, $\Delta K_{th,II}$ and $\Delta K_{th,III}$ are the threshold stress intensity factors for mode I, mode II and mode III, respectively.

(Liu and Mahadevan, 2007) expressed the equivalent mixed mode stress intensity factor range at the crack tip ΔK_{eq} in terms of the uni-modal stress intensity factor ranges and material properties, that is given in Eq.(5.14) (Haidari and Heidari, 2017; Haidari and Tehrani, 2015).

$$\Delta K_{eq} = \frac{1}{B}\sqrt{(K_I)^2 + \left(\frac{K_{II}}{s}\right)^2 + \left(\frac{K_{III}}{s}\right)^2 + A\left(\frac{K^H}{s}\right)^2} = f\left(\frac{da}{dN}\right) \tag{5.14}$$

The superscript "H" indicates the hydrostatic stress related term; s is related to material ductility, and expressed as the ratio of mode II and mode I fatigue crack threshold stress intensity factors. $s = \frac{K_{II,th}}{K_{I,th}}$. A larger value of *s* ($s > 1$) indicates tensile dominated failure and a smaller value of *s* ($s < 1$) indicates shear dominated failure.

Table 5-1 Material parameters for fatigue crack propagation prediction

Material Property	$s = \frac{t_{-1}}{f_{-1}} \le 1$	$s = \frac{t_{-1}}{f_{-1}} \ge 1$
γ	$\cos(2\gamma) = \frac{-2 + \sqrt{4 - 4\left(\frac{1}{s^2} - 3\right)\left(5 - \frac{1}{s^2} - 4s^2\right)}}{2\left(5 - \frac{1}{s^2} - 4s^2\right)}$	$\gamma = 0$
A	$A = 0$	$A = 9(s^2 - 1)$
B	$B = \left[\cos^2(2\gamma)s^2 + \sin^2(2\gamma)\right]^{1/2}$	$B = s$

For the commonly used cast iron for railroad wheels, it falls into the range $1/\sqrt{3} \le s \le 1$. For this thesis, the amount of "s" for railway wheel is assumed to be shear dominated and equal to 0.6. "A" and "B" are material parameters that can be determined by tension and shear fatigue limits and listed in Table 5-1 (Liu et al., 2006).

5.4.2.2 Fatigue crack growth rate

The crack-growth rate is used to describe the fatigue crack propagation behavior. A number of mathematical equations exist in the literature to express the relationship between fatigue crack growth rate, *da/dN* and stress intensity factor, *ΔK*. Some of them are proposed by Paris (Paris,

1961), Forman and co-workers (Forman et al., 1967) and Walker (Walker, 1970), and their equations are given in Eq. (5.15), (5.16) and (5.17) respectively.

$$\frac{da}{dN} = C\left(\Delta K\right)^m \tag{5.15}$$

$$\frac{da}{dN} = f\frac{C\left(\Delta K\right)^m}{\left(1-R\right)K_c - \Delta k} \tag{5.16}$$

$$\frac{da}{dN} = C\left(\frac{\Delta K}{\left(1-R\right)^{1-\gamma}}\right)^m \tag{5.17}$$

Where $\frac{da}{dN}$ is the crack growth rate, ΔK represents the stress intensity factor range, R is the stress ratio, and $C, m,$ and γ are material parameters. For this thesis, Walker model (Walker, 1970) is used to describe the relationship between the fatigue crack growth rate and stress intensity factor since it considers the effect of the stress ratio.

In case of mixed mode crack growth mode, all stress intensity factors for all modes are combined together using Eq. (5.14) and give the equivalent stress intensity factor, which may be correlated to mode I fatigue crack growth curve for fatigue life prediction. Eq.(5.17) can be rewritten as (Shantz, 2010):

$$\frac{da}{dN} = C\left(\frac{\Delta K_{eq}}{\left(1-R\right)^{1-\gamma}}\right)^m \tag{5.18}$$

Where, ΔK_{eq} is the equivalent stress intensity factor range for mixed-mode loading. From (Kim and Kim, 2002), the values of $C, m,$ and γ are 4.01×10^{-9}, 3.13185, and 0.8246 respectively for the rail wheel material. For mode I SIF, the stress ratio ranges between 0 and 1. However, for mode II and mode III SIFs, the stress ratio ranges between 0 and -1 depending on their locations (Haidari and Tehrani, 2015). In this study, the stress ratio of -1, -0.5, 0 and 0.5 were investigated to see the effect of the stress ratio on the crack growth rate. Figure 5.3 illustrates the crack growth rate for different stress ratio -1, -0.5, 0 and 0.5. The parameter used in this thesis is approaches to 0 and thus 0 is assumed to be the stress ratio used and applied in Eq. (5.18) .

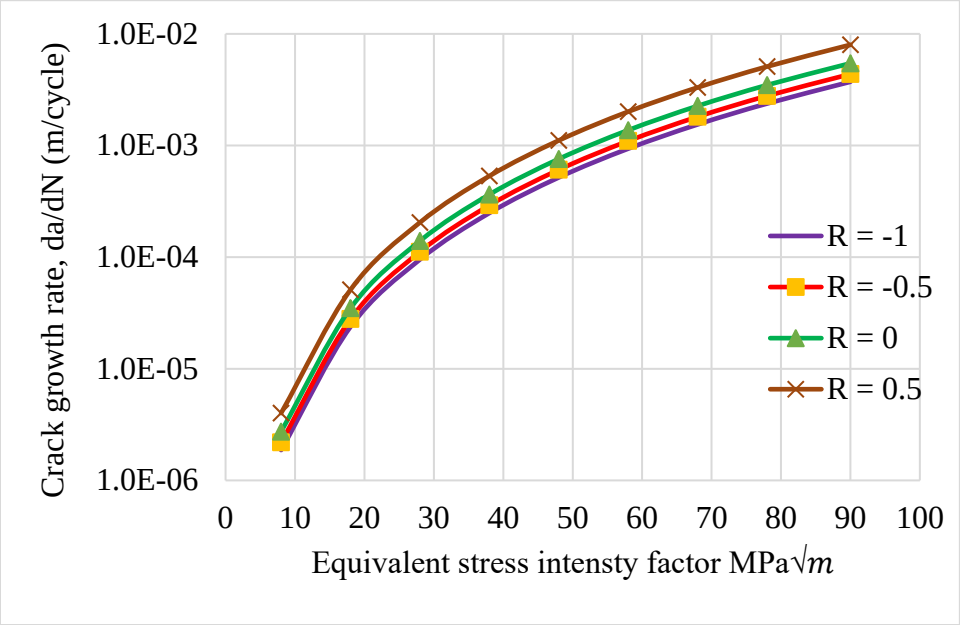

Figure 5.3 Fatigue crack growth rate Vs ΔK_{eq} for the selected stress ratio

5.4.3 Fatigue life calculations

When the stress ratio range is assumed to be zero, the Eq. (5.18) of (Walker, 1970) is reduced to Eq. (5.15) of the (Paris, 1961). Therefore, the fatigue crack propagation life can be easily calculated by using (Paris, 1961) equation. Integrating Eq. (5.15) (where $\Delta K = Y(a) * \Delta\sigma\sqrt{a}$) with the initial and final crack length as the limit of integration (Eq. (5.16)) and if the Y(a) doesn't change within the limits of integration, the fatigue life can be given by Eq. (5.17).

$$\Delta N = \int_{a_0}^{af}\left(\frac{1}{A\,(Y(a)\,\Delta\sigma\sqrt{a})^{m}}\right)da = \frac{1}{A\Delta\sigma^{m}}\int_{a_0}^{a_f}\left(Y(a)\sqrt{a}\right)^{-m}da \tag{5.19}$$

$$\Delta N = \frac{2}{(m-2)CY(a)^{m}\Delta\sigma^{m}}\left[\frac{1}{a_0^{(m-2)/2}} - \frac{1}{a_f^{(m-2)/2}}\right] \tag{5.20}$$

The a_i is the initial crack size, which can be determined by Eq. (5.21) (Fajdiga and Sraml, 2009)

$$a_i = \frac{1}{\pi}\left(\frac{\Delta K_{th}}{\Delta\sigma_f Y}\right)^2 \tag{5.21}$$

where Y is a geometry correction factor and depends on the crack configuration and ignoring it may be a non-negligible source of error (Haidari, and Heidari, 2017), $\Delta\sigma_f$ is the fatigue limit stress and is K_{th} the fatigue threshold stress intensity factor.

Assuming that final fracture occurs when the crack length reaches a critical crack size, which is $a_f = a_c$. The value of the critical crack length depends on the fracture toughness value and can be determined by Eq. (5.22). The threshold and fracture toughness values depend on the rail wheel material and can be determined experimentally. In this thesis, the considered value of K_{th} and K_{IC} for rail wheel material are 8.2 and 86.8 $MPa\sqrt{m}$ respectively (Barber, 2018b).

$$a_c = \frac{1}{\pi}\left(\frac{K_{IC}}{Y(a) * \Delta\sigma}\right)^2 \tag{5.22}$$

CHAPTER 6

6 FINITE ELEMENT MODELING OF WHEEL-RAIL CONTACT CONDITIONS

This chapter presents the three-dimensional finite element (FE) model used in rail wheel contact analysis and crack modelling. A 3D finite element model is needed to build a more realistic model of wheel-rail rolling contact problem. This model analyzes the 3D stress response in the contact region and sub surface crack initiation and growth. For computational efficiency, the finite element model is divided into two steps: global model and sub model. A three-dimensional finite element global model and sub model are generated in ABAQUS as shown in Figure 6.1 a) and b). The results from the global model analysis are considered as the input for the sub-model analysis.

A. Global model analysis

The wheel with 0.46 m of radius in longitudinal direction was modelled. The UIC-60E1 profile standard was used for rail dimensions. The length of the rail part was chosen to be 0.6 m because the two sleepers could be placed underneath the rail at the standard distances of 0.6m. In this study, the train is assumed to roll on a straight track; the contact patch is assumed to be located at the centre of the railhead. Appendix A and B contains the exact dimensions of the wheel and rail profile.

B. Sub-model analysis

The length of the rail part was chosen to be 0.08 m for the sub modelling. The FE sub-model to the desired orientation and boundary conditions from the global model was used for the contact analysis and crack modelling.

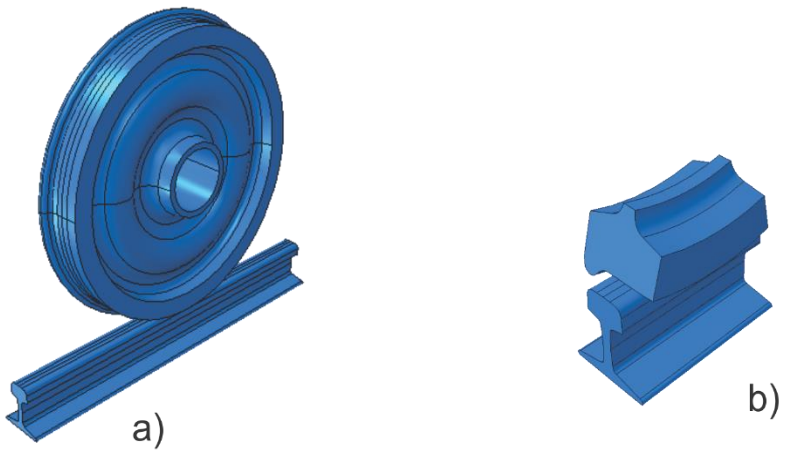

Figure 6.1 3-D finite element model of rail wheel: a) full model, b) sub model

6.1 Material Properties Used for the Contact Analyses

Linear elastic material properties of the rail wheel which are listed in Table 6-1 were used in investigation of normal and tangential contact problems. Additionally, the constitutive plasticity model of the rail wheel material, which was described in Chapter 4, are used to investigate the effect of the plastic deformations. The elasto plastic material parameters of the rail wheel which are given in Table 6-1 were used for the investigation (Vo, 2015).

Table 6-1 Rail wheel material properties for contact analysis

	Wheel	Rail
Poisson ratio	0.3	0.3
Young's modulus	206 GPa	200 GPa
Density	7,850 Kg/m^3	7,850 Kg/m^3

6.2 Load Definitions

Half of the axle load, which was called as wheel load, was used in this analysis. 85 kN was selected as the wheel load for the rolling contact modelling and crack modelling. The effects of different wheel loads were also investigated in the normal contact model. The load was applied at the center of the wheel. A reference point, where the load was applied, was created at the center of the wheel. In order to transmit the force from the reference point to the inner surface of the wheel, there should be a connection definition between them. In ABAQUS, the constraint option can be used to create such connection. This option contains different definitions like 'rigid body' and 'coupling' etc. (Özdemir, 2016; Systèmes, 2007). Figure 6.2 shows the coupling definition between a reference point and inner surface of the wheel for the sub-model.

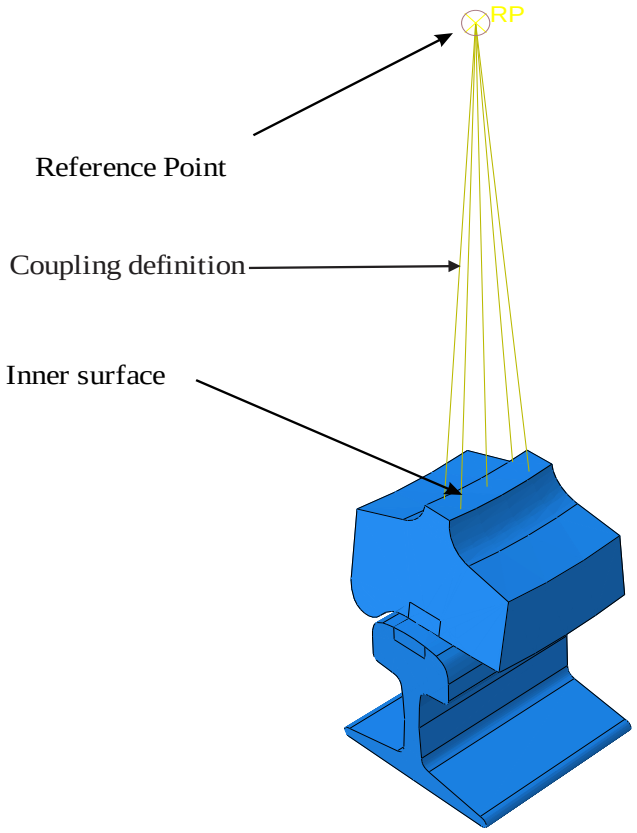

Figure 6.2 Coupling constraint between a reference point and inner surface of the wheel

6.3 Boundary Condition and Contact Definitions

The boundary conditions are applied to the bodies in order to restrict undesired displacements of the bodies in the analysis. In the normal contact model, the rail was fixed at the end of the right and left sides. Movement of the wheel part in the right and left directions and rotation around the vertical direction were constrained to keep wheel moving only in the vertical direction as illustrated

in Figure 6.3 for the global modelling. In case of sub-modelling all of the boundary conditions were fed into the cut portions of the sub model from the global modelling.

In the contact definitions, the wheel serves as the master surface and the rail serves as the slave surface for both the global and sub model (see Figure 6.4 for sub-model). In case of normal contact conditions, only normal contact parameters were applied. However, in case of the tangential contact conditions, wheel was free to move along the longitudinal directions and vertical directions.

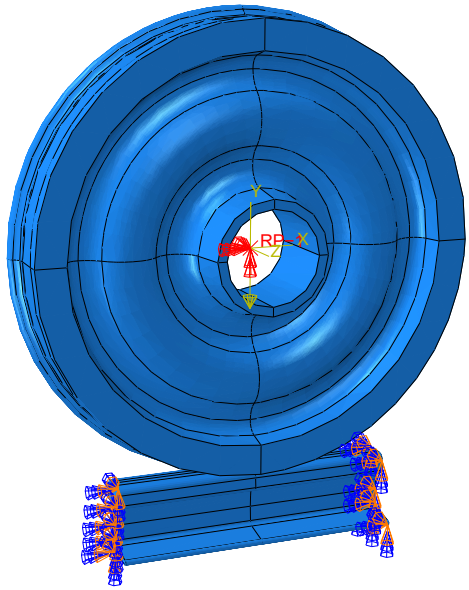

Figure 6.3 Boundary conditions applied to the global modelling

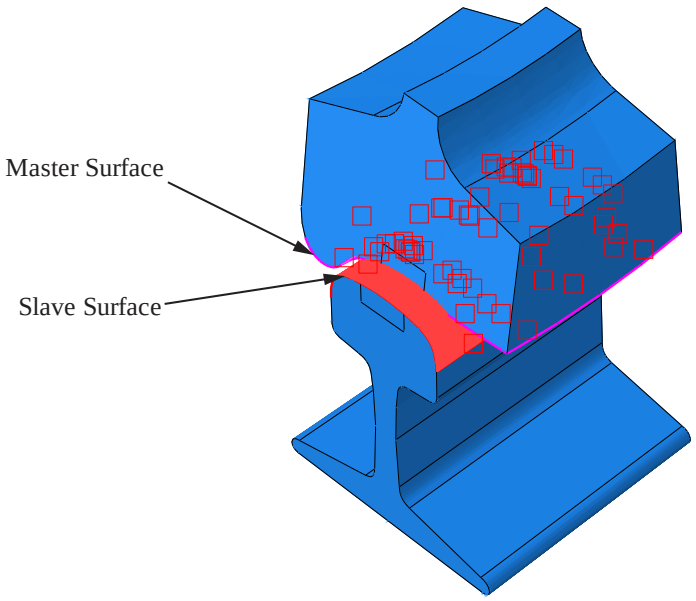

Figure 6.4 Master and slave surfaces in the contact definition

6.4 Meshing

The strategy of the meshing significantly influences the accuracy of the results and the duration of the simulations (Özdemir, 2016). A finer mesh is better in order to obtain more accurate results. However, the refinement extends the computation period. This is a drawback for the finite element models for bigger sizes. This is the reason for categorizing the FE model into global model and sub-model analysis. Therefore, the refinement process was only applied on the critical contact zones of the rail wheel in case of the sub-model analysis. In this study, the C3D8R (an 8-node linear brick, reduced integration, hourglass control) solid element was used for the analysis of the wheel-rail contact in both global and sub-model for two main reasons. First, the first-order element is better to give more precise pressure distribution in contact problem; and the second reason is it reduces computational time. Same type of the element was applied on all components of the assembly (see Figure 6.7). The structure of the element discretization in the bodies is coarse, but the element discretization in contact zone of the bodies is fine.

To describe the effect of element sizes on simulation results, the finite element sub-model was run with different mesh sizes (2, 1.6, 1.2, 1, 0.8 and 0.5 mm) at the contact zone under 85 kN wheel load. The mesh size at the contact surface was changed and maximum pressure levels were evaluated. It was observed that the finer mesh gives the higher pressure (see Figure 6.5). The pressure levels were converging with the element size ranges between 1.2 mm (1445 MPa) and 0.5 mm (1465 MPa). The difference between the pressure values of 1.2 mm and 0.5 mm was only

1.4%. Therefore, fine mesh (1.2 x 1.2 mm) was generated at the contact zone and coarse mesh (4 × 4 mm) was applied for those regions furthest from the contact surface to minimize the computation time for the FE sub model and course mesh 10 × 10 mm was applied for the FE global model. A total of 124,368 elements and 110,428 nodes, which is shown in Figure 6.6 , have been considered for a global model analysis and a total of 131,606 elements and 152,764 nodes, which is illustrated Figure 6.7, have been considered for a sub-model analysis. Table 6-2 shows detailed numbers of elements and nodes for the FE model.

Table 6-2 Detailed number of elements and nodes used in FE model

Part	**Element type**	**Number of elements**		**Number of nodes**	
		Global model	Sub-model	Global model	Sub-model
Wheel	C3D8R	93276	77076	82821	93055
Rail	C3D8R	31092	54530	27607	59709

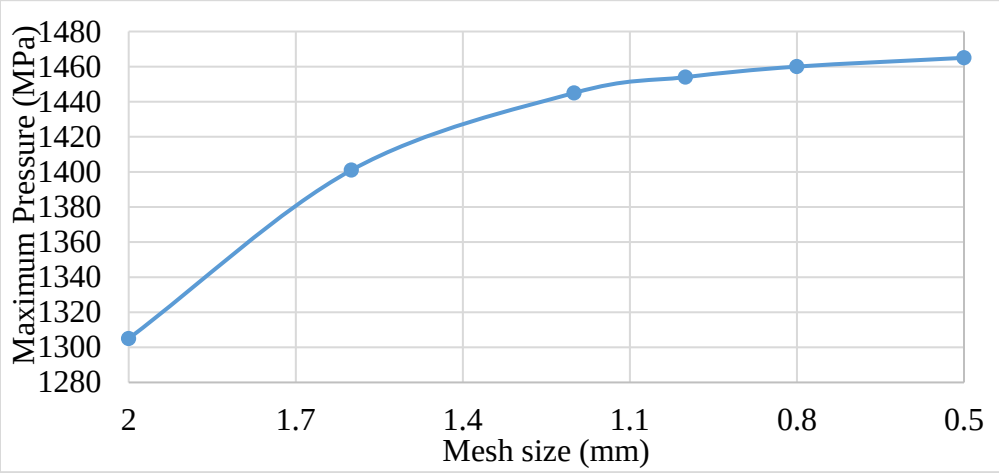

Figure 6.5 Maximum pressure levels for various element sizes in normal contact model

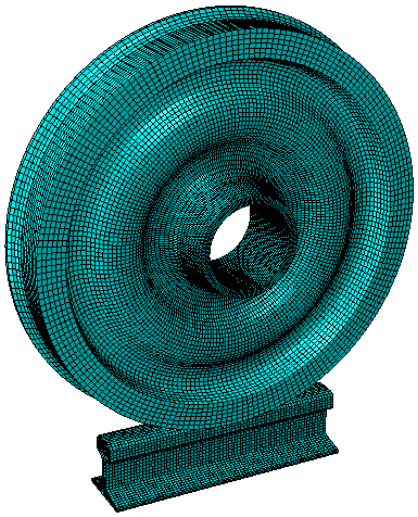

Figure 6.6 Rail-wheel assembly mesh for a global-model

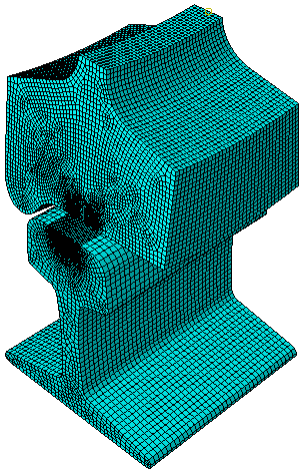

Figure 6.7 Rail-wheel assembly mesh for a sub-model

6.5 Finite Element Modelling of Sub-Surface Cracking

In this section, the sub-surface cracking in rail-wheel contact is modeled using a 3D FE model. In the same manner to normal and tangential contact problem analysis, the sub-surface cracking is modelled by using sub-modeling techniques. The results from the global model is applied as boundary conditions to the sub-model. In the FE sub model, the geometry of the rail wheel is more simplified for computational effectiveness. Figure 6.8 a)-c) show the 3D finite element model of a sub-modelling in which an elliptical crack (1 mm of major diameter and 0.75 mm of the minor diameter) is built in the wheel portion. A sub surface crack is assumed to be 3 mm below the surface of the wheel thread with an orientation of 20^{o} from horizontal plane. The vertical load

applied on the wheel of 85 kN is considered. XFEM ABAQUS was used to simulate the crack growth behaviour. Finally, the uni-modal stress intensity factors (KI, KII, and KIII) at a crack tip are determined from the sub model of the XFEM results. The equivalent stress intensity factor can be obtained from KI, KII, and KIII by using Eq. (5.14).

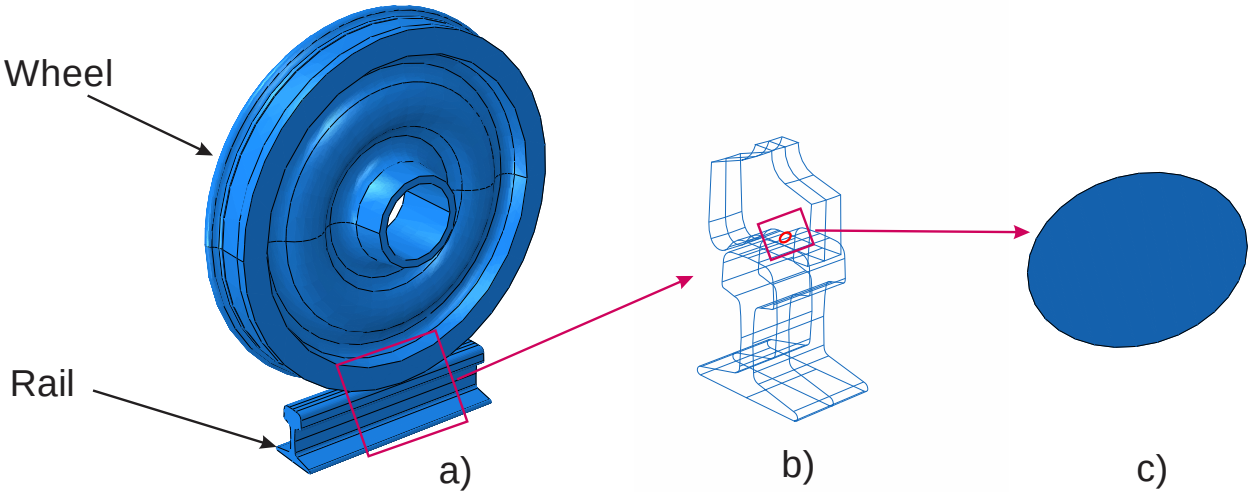

Figure 6.8 A sub-surface cracking in rail-wheel: (a) global model, (b) sub-model, (c) crack.

CHAPTER 7

RESULTS AND DISCUSSION

7.1 Analytical Results

7.1.1 Normal contact condition

The analytical approach (Hertzian elastic theory is considered in this study) of determining the rail wheel contact parameters under normal contact condition was discussed in Chapter 3. The results obtained from those equations are presented in this section.

a) Elliptical contact area

Considering the wheel with the rolling radius ($R_x^{(w)}$) = 430mm and the rail with the radius of the head ($R_y^{(r)}$) = 300 mm, $R_y^{(w)}$ =510 mm, $R_x^{(r)}$ is infinity (i.e. $\frac{1}{R_x^{(r)}} = 0$) since the rail is assumed to be straight. The whole dimensions of the rail and wheel are given in appendix A and B respectively. Substituting all these parameters in Eq. (3.14) and (3.15), $A+B$ and $B-A$ can be calculated as 0.00283 and 0.0005 respectively (i.e. A = 0.0038 and B = 0.00168). An intermediate parameter, angle 'θ' can be found by substituting A+B and B-A values into Eq.(3.13) and calculated as 63.76°. Then, by interpolating, the values of *m* and *n* can be determined by substituting the A and B values into Eq. (3.19) and (3.20). The values of m and n are 1.38 and 0.76 respectively. The same values of m and n could be obtained from the Table 3-1 at $\theta = 63.76°$.

Assuming the maximum load on a single wheel is approximately equal to F_n = 85 kN, and substituting all parameters into Eq. (3.9) and (3.10), the values of the contact patch 'a' and 'b' was found to be 7.11 mm and 4.12 mm, respectively.

b) Pressure distribution in the contact area

Substituting the values of F_n = 85 kN, a = 7.11 mm, and b = 4.12 mm into Eq. (3.25), the maximum normal contact pressure P_o, occurs at the center of the contact patch is 1386 MPa. From the Eq. (3.26), the semi ellipsoidal normal contact pressure distribution plotted along major and minor diameter of the contact ellipse, which are illustrated in Figure 7.1. The three-dimensional Hertzian pressure distribution in the wheel was also plotted from the Eq. (3.26) and illustrated in Figure 7.2.

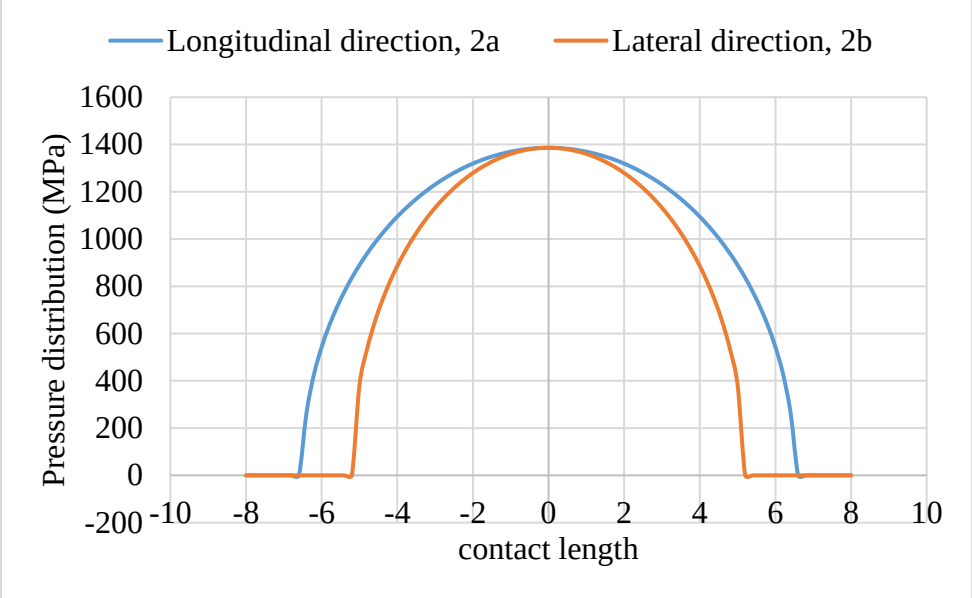

Figure 7.1 Semi-ellipsoidal contact pressure along the longitudinal and lateral direction

7.1.2 Tangential contact condition

Kalker's linear theory and Polach's tangential theory were discussed in Section 3.4. Their models are used for determining the rail wheel contact parameters under tangential contact condition. The results obtained from those equations are presented in this section. Three cases are considered to describe the relationship between the traction force and the longitudinal creepage.

Case 1. Grease lubricated condition, $\mu = 0.05$

Case 2. Water lubricated condition, $\mu = 0.2$

Case 3. Dry wheel-rail contact condition, $\mu = 0.45$: taken from (Vo, 2015)

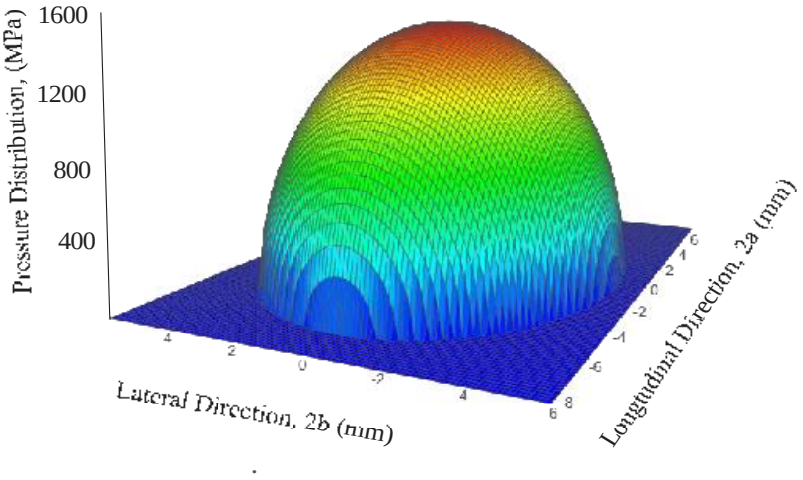

Figure 7.2 3-D ellipsoidal normal contact pressure

For the values of $a = 7.11$ mm, and $b = 4.12$ mm, c_{11} was determined from Eq. (4.22) and found to be 4.22. From Eq. (3.37), the traction force vs the longitudinal creepage was plotted in **Error! Reference source not found.** for the three above cases of rail-wheel contact conditions. For these contact conditions the applied wheel load is assumed to be 85 kN. Figure 7.3 shows that the traction force increases with the longitudinal creepage and also it can be observed that the traction force increases as the friction coefficient increases.

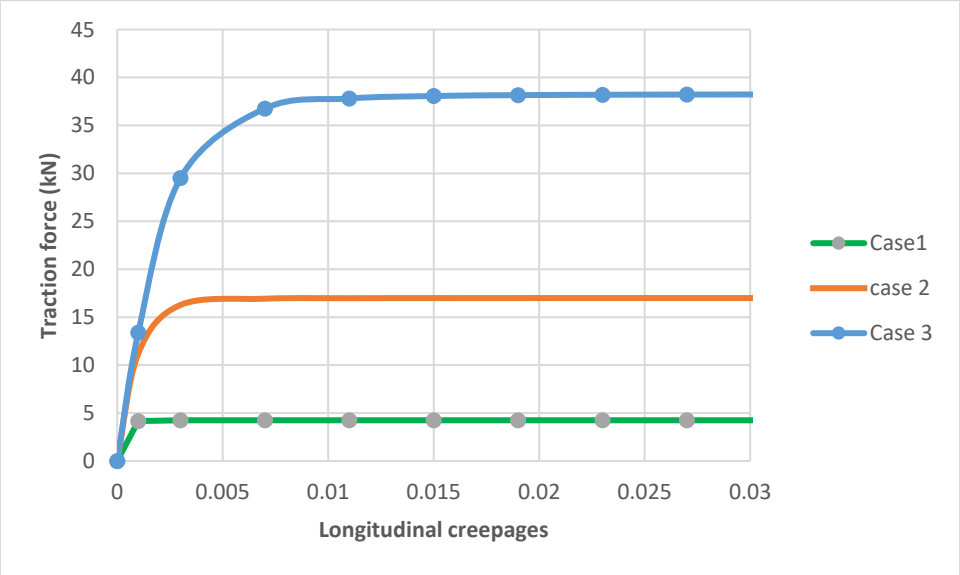

Figure 7.3 Traction vs longitudinal creepages for different contact conditions

7.2 Finite Element Results

7.2.1 Rail-wheel normal contact condition

a) Normal contact pressure distribution

In this finite element analysis, normal contact problem was solved at the first step. In the normal contact conditions, the coefficient of friction was not considered since there was no rolling motion. Therefore, the rail wheel quasi-static frictionless contact was analyzed. The linear elastic material properties, which are given in Table 6-1, were used for normal contact investigation. The maximum pressure distribution obtained from the FE global modelling was 1133 MPa and 1431 MPa for the rail and wheel respectively. Figure 7.4 and Figure 7.5 illustrate the normal contact pressure distribution obtained from the FE global model for the wheel and rail respectively. In the same manner Figure 7.6 and Figure 7.7 show the results of normal contact pressure distribution of the FE sub-model, for the wheel tread and rail head respectively. The maximum normal contact pressure is 1427 MPa and 1454 MPa for the rail and wheel respectively in case of the sub model. This shows that the pressure distribution results obtained from the FE sub-model are greater than the values obtained from the global model. This deviation is due to the finer mesh in case of the sub-model. Therefore, the sub-modelling technique is the efficient way of computing and the results obtained from the FE sub-model is more accurate.

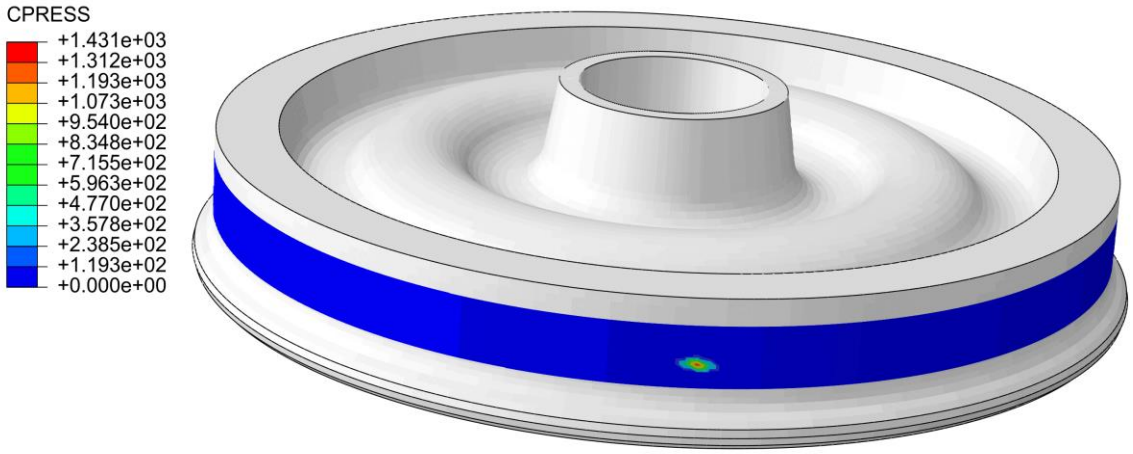

Figure 7.4 Normal contact pressure distribution of the wheel in case of the global model

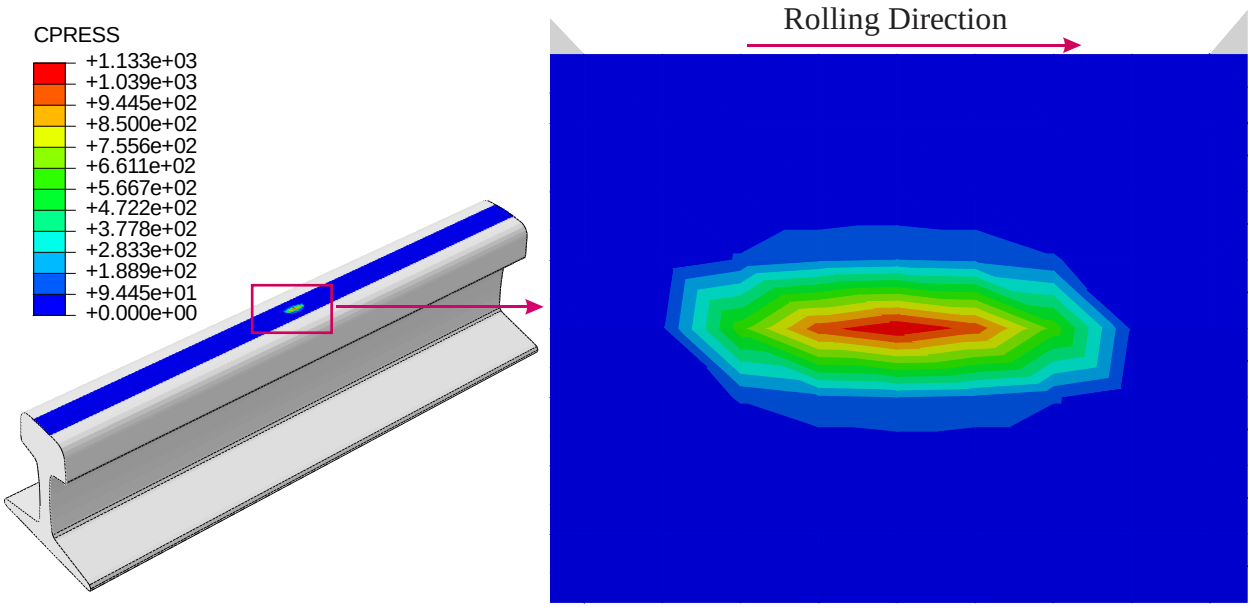

Figure 7.5 Normal contact pressure distribution of the rail in case of the global model

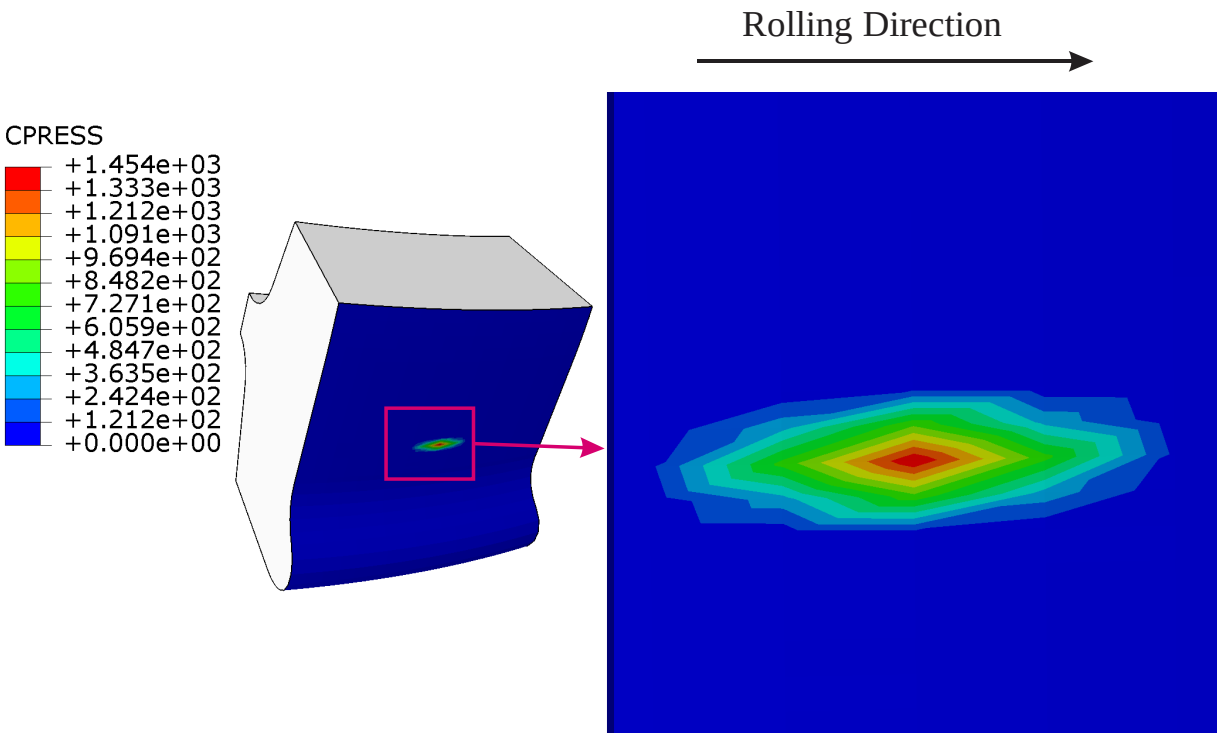

Figure 7.6 Contour plot of contact pressure distribution on the wheel

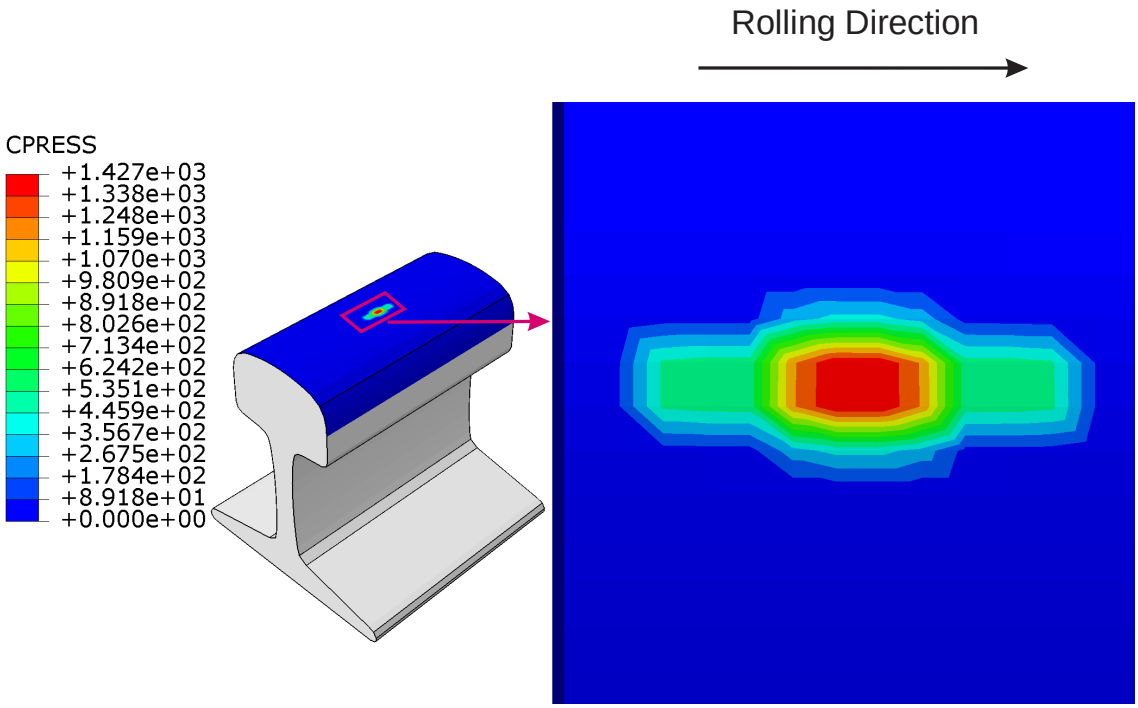

Figure 7.7 Contour plot of contact pressure distribution on the rail

Figure 7.8 shows the normal contact pressure distributions on the wheel tread along longitudinal and lateral directions in case of the FE sub model. From the numerical results, it can be seen that the pressure distribution is almost symmetric and the graph curve agree to the analytical result which was illustrated in Figure 7.1.

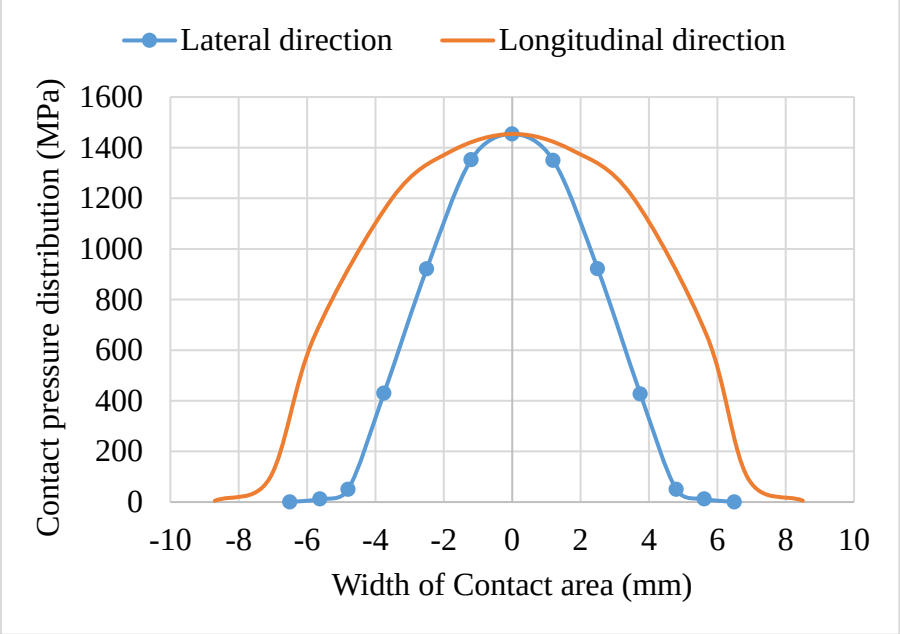

Figure 7.8 Pressure distribution along longitudinal and lateral distribution from FE result

7.2.2 von-Mises stress distributions

The von Mises stress distribution in the rail-wheel normal contact surface under the wheel load of 85 kN is illustrated in Figure 7.9. The maximum Von Mises stress value obtained is 8371 MPa. Figure 7.10 shows the Von Mises stress distribution along z direction from the center of contact surface. From this curve, it is clearly seen that the maximum Von-Mises stress distribution is occurred at the depth between 2 and 4 mm from the contact surface. This is the main cause for the sub-surface fatigue crack initiation, which later propagate to the surface and cause wheel failure.

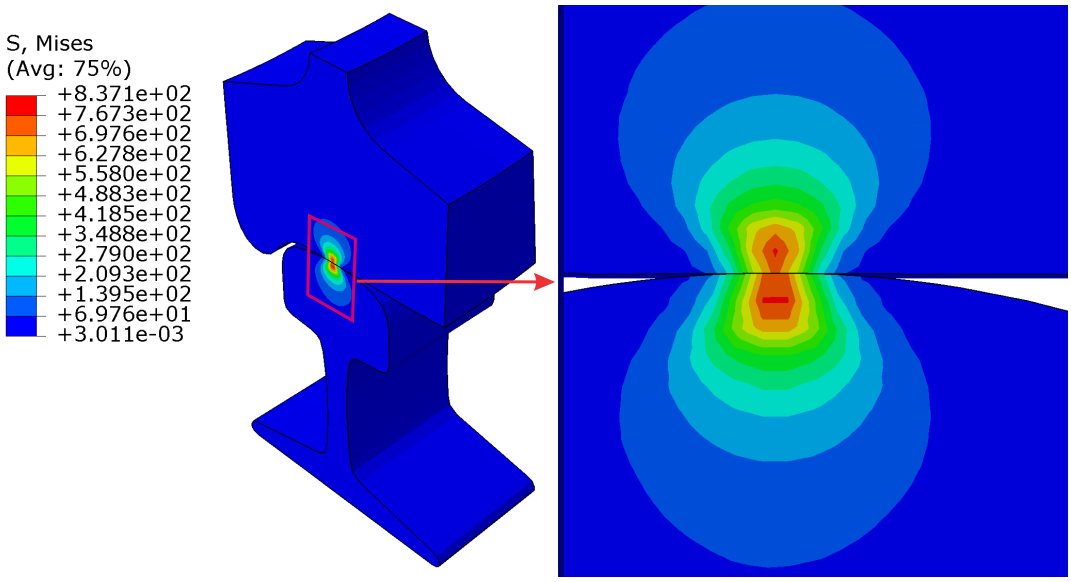

Figure 7.9 von-Mises stress distribution in the cross-section view rail and wheel

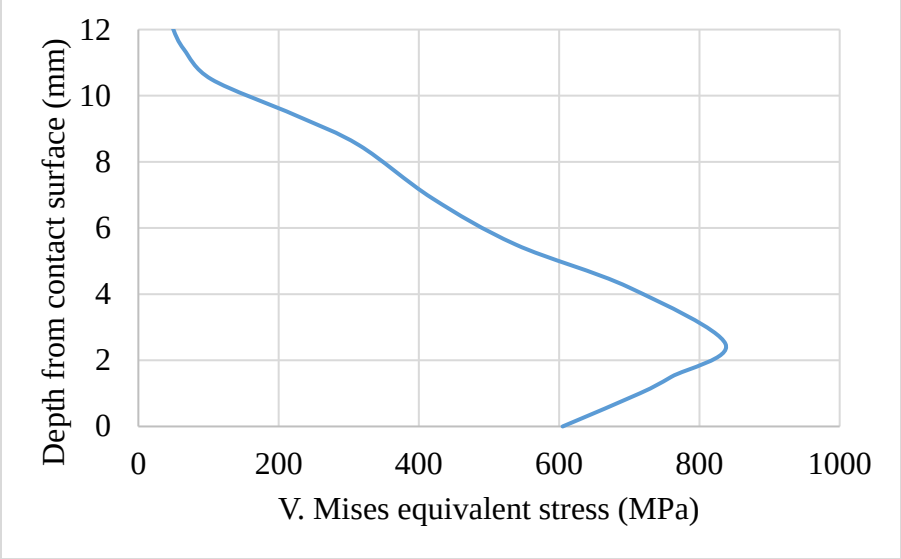

Figure 7.10 von-Mises stress distribution in the wheel along vertical direction

7.2.3 Rail-wheel tangential contact condition

Finite element analysis of the rail wheel tangential contact condition is discussed in this section. FE model was used to analyze two condition of the tangential contact problem: 1) Partial slip condition and 2) Full slip conditions. In tangential contact condition, both the normal pressure distribution and tangential traction distribution have to be applied. Since the track is assumed to be straight, the lateral (η) and spin creepages (φ) are ignored, and thus only longitudinal creepage (ξ) is considered in this study. Two values of longitudinal creepage (ξ) are taken from (Vo, 2015): 0.47% for partial slip and 1.2% for full slip in order to investigate the effect of the creepages on the contact stresses. Additionally, μ=0.2 frictional coefficient was applied between the rail and wheel.

The FEA of the pressure and the shear stress distribution along the moving direction in case of the partial slip is illustrated Figure 7.11. In this figure, it is clearly shown that the shear stress reaches the traction bound in the slip region only.

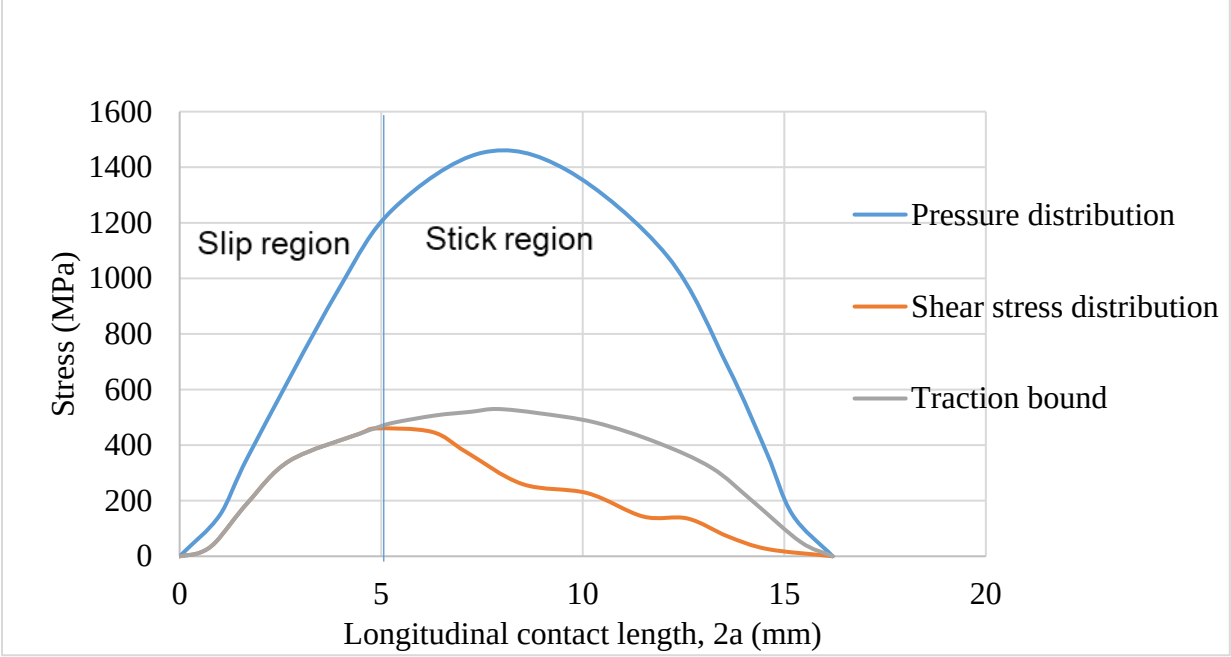

Figure 7.11 Pressure and shear stress distribution along moving direction for the partial slip

In case of the full slip condition, shear stress distribution reaches the traction bound over the contact area. Furthermore, the maximum shear stress occurred in full slip condition higher than the result of the partial slip condition. Results of the partial sliding and full sliding condition are

summarized in Table 7-1. Shear stress distribution of the full slip condition is given in Figure 7.12 and Figure 7.13.

Table 7-1 FE results of tangential contact conditions

	Partial sliding	Full sliding
Maximum shear stress, (MPa)	480	530
Maximum Pressure, (MPa)	1454	1454
Traction force, KN	34.2	38.2

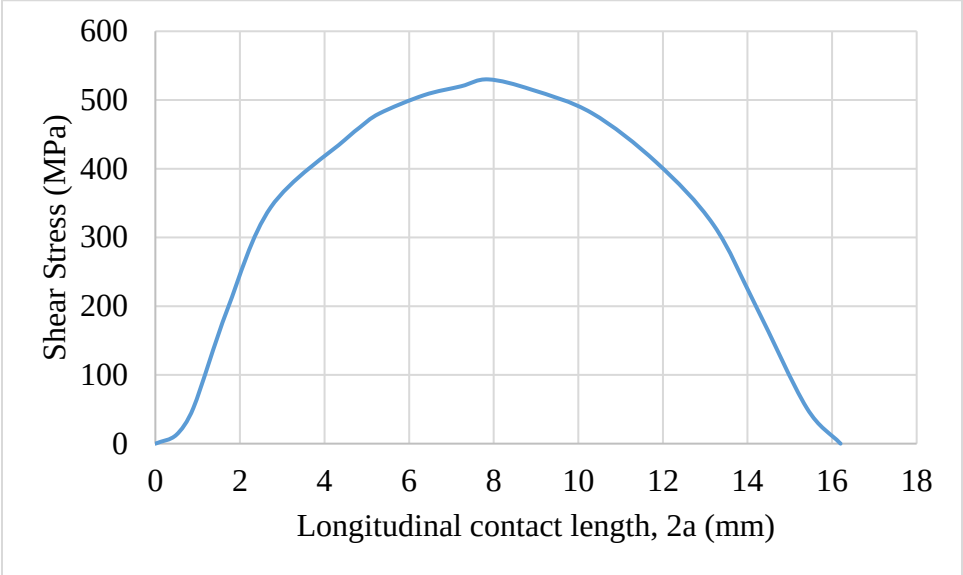

Figure 7.12 Shear stress distribution in full slip condition along longitudinal direction.

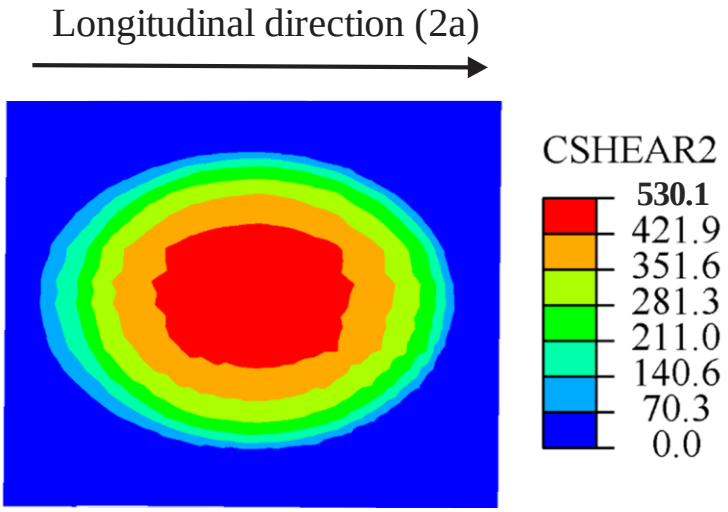

Figure 7.13 Shear stress distribution in full slip condition

7.3 XFEM Result

The STATUS XFEM output in the XFEM analysis is red for the stable crack surrounding the crack surface and different color spectrums for a growing crack and PHILSM and PSILSM are the two-level set values to represent the crack from the normal and tangent to show the crack growth behavior. Figure 7.14 shows the STATUSXFEM of the subsurface crack growth of the rail wheel and the spalling of the wheel from the field observation. The STATUSXFEM shows that the wheel was deformed in the form of spalling. Figure 7.15 and Figure 7.16 illustrate the PSILSM and PHILSM of the crack growth behaviour of the rail wheel respectively.

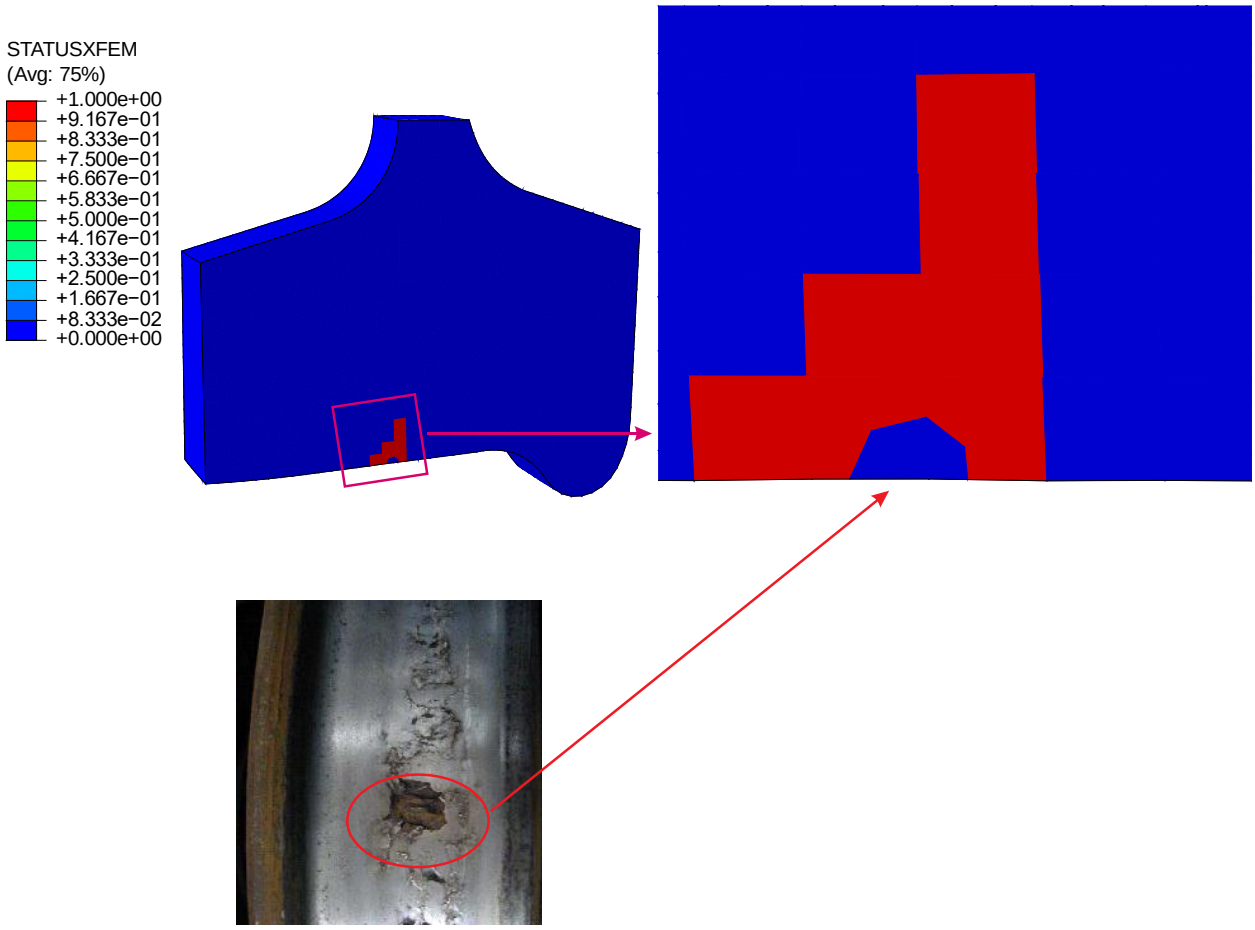

Figure 7.14 STATUSXFEM result of the wheel and spalling of the wheel from the field observation

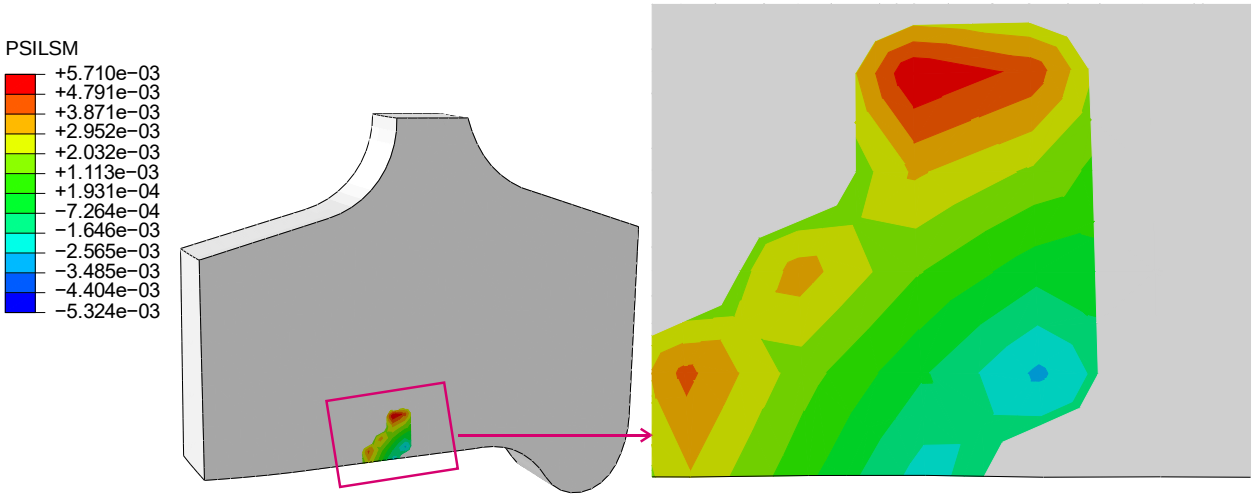

Figure 7.15 PSILSM result of the wheel

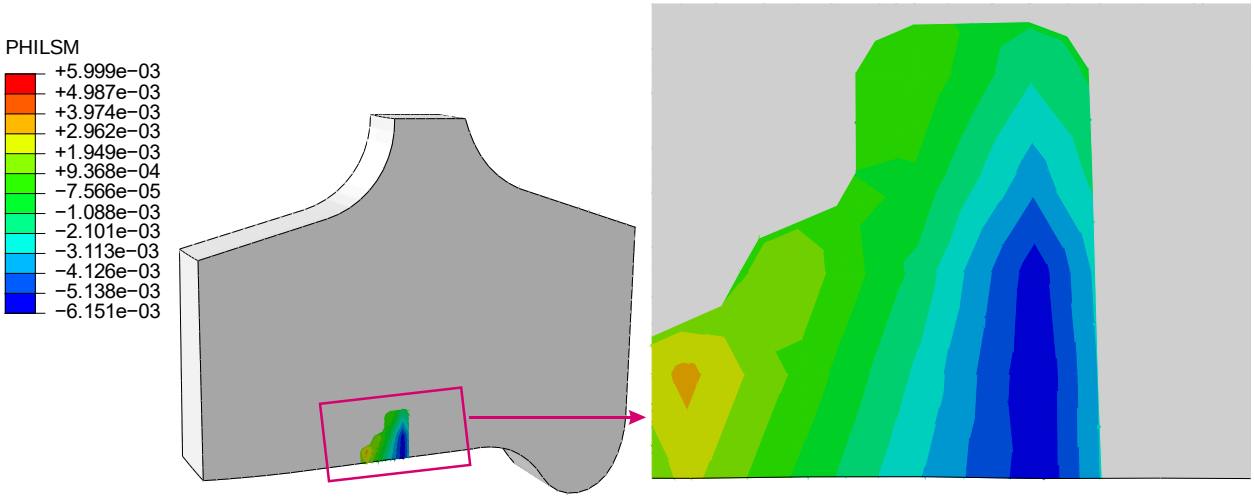

Figure 7.16 PHILSM result of the wheel

7.4 Comparison Between Analytical and FE results For Normal Contact Conditions

A. Contact patch and pressure distribution

In this section, analytical computation results are compared with finite element results. The values of half-length ‘a’ and half-width ‘b’ of the contact area as well as the maximum contact pressure are summarized in Table 7-2. Analytical and FE results of pressure distribution along the longitudinal direction and the lateral direction are illustrated in Figure 7.17 and Figure 7.18

respectively. These comparisons show that the results obtained from finite element analysis are almost approach to analytical (Hertz's approaches) results.

Table 7-2 Analytical and FEM results

Descriptions	Hertz analytical	FEM	Deviation in percent
Major contact width (a), in mm	7.0	8.1	13.5 %
Minor contact (b), in mm	4.1	4.4	6.8 %
Maximum Pressure, P_{max} in MPa	1386	1454	4.6 %

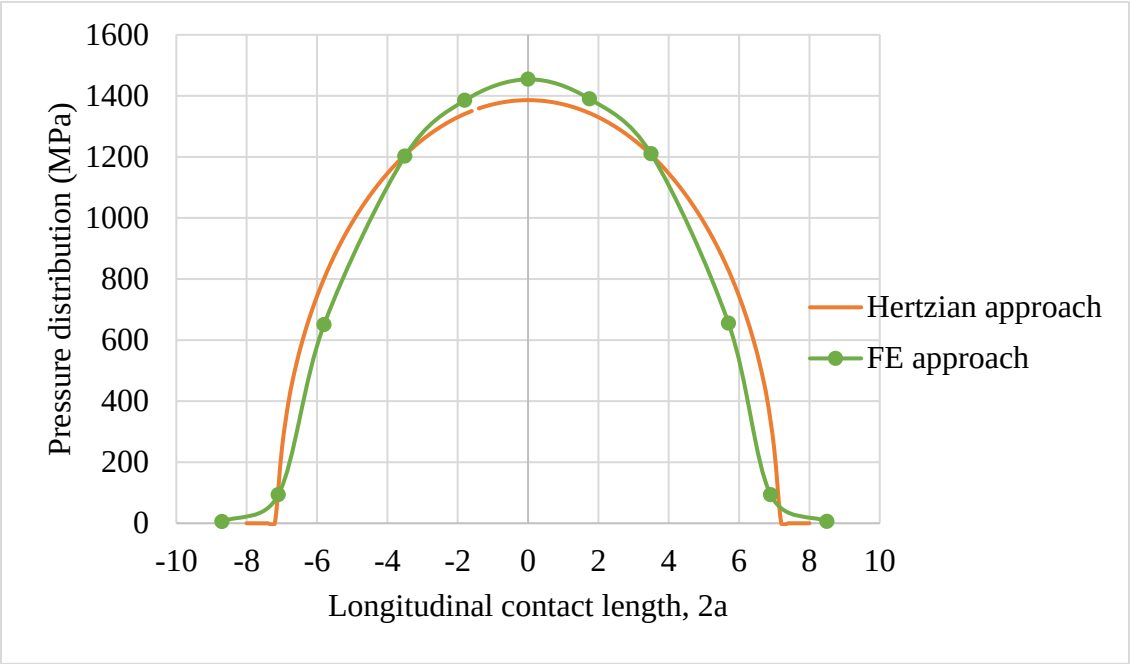

Figure 7.17 Contact pressure distribution along longitudinal direction (2a)

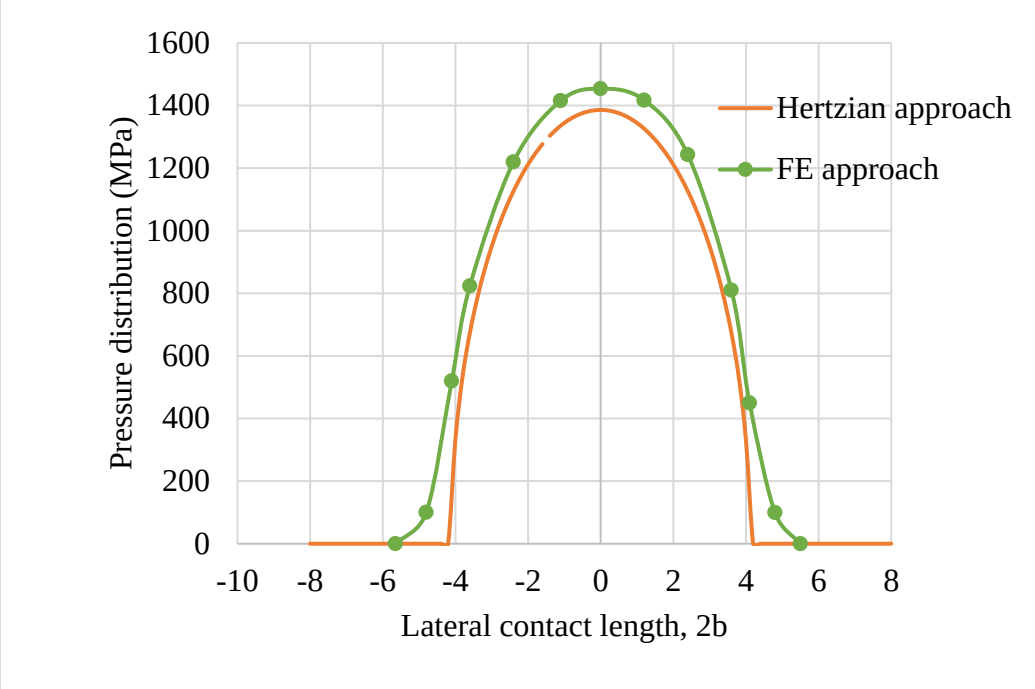

Figure 7.18 Contact pressure distribution along lateral direction (2b)

B. Effect of the wheel load and plastic deformations

In order to investigate the effect of different loading conditions and plastic deformation on both the rail and wheel, five different wheel loads (55 kN, 70 kN, 85 kN, 100 kN, 115 kN and 130 kN) were applied. The effect of these loads was evaluated for FE elastic material model, FE elasto-plastic material model and Hertz analytical results. Finally, the maximum normal contact pressure values obtained were compared. The critical value of the wheel load was estimated depending on the maximum normal contact pressure levels.

Figure 7.19 shows the numerical results of maximum normal contact pressure distribution on the wheel versus wheel load for both elastic and elasto plastic material model, and also for Hertzian theory. The results show that the maximum normal contact pressure (P_0) increases with the increasing wheel load, *L* in case of both elastic and elasto- plastic FE model as well as Hertzian theory. From the results, 85 kN can be considered as the critical values of the wheel load to deform plastically according to elastoplastic material model. When the wheel load is below the critical values (85 kN), the effect of the plastic deformation is not more visible from the numerical results.

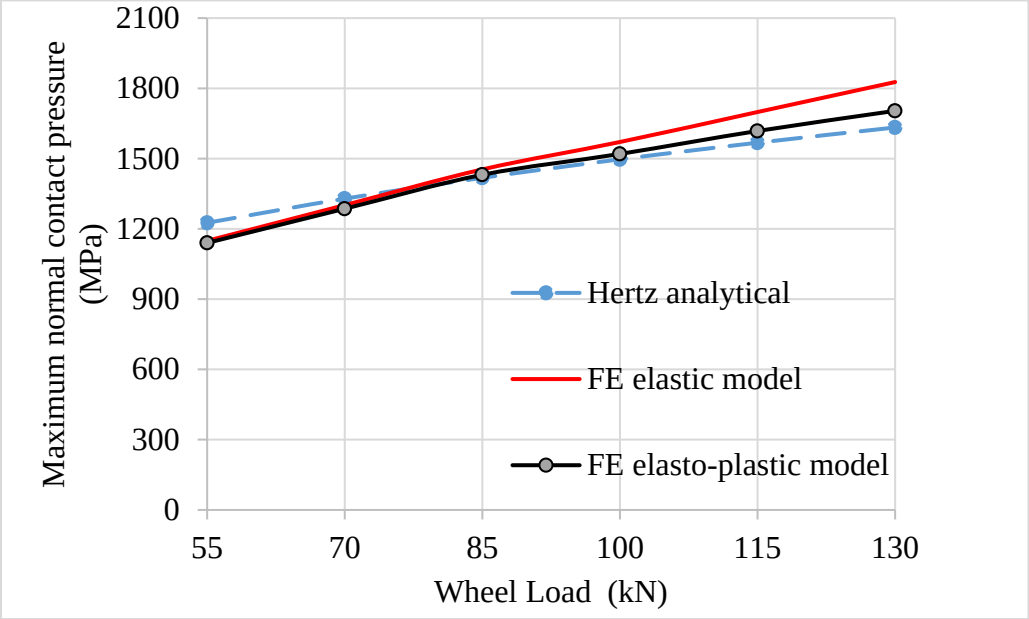

Figure 7.19 Maximum normal contact pressure (Po) levels versus the wheel loads levels

7.5 Comparison Between Analytical and FE Results For Tangential Contact Condition

a) **Traction force between wheel and rail**

The FE model results and analytical results are given in Table 7-3 when 85 kN of the wheel load was applied. The results show that the traction force obtained from both FE model and analytical calculations are almost approach to each other. As the levels of creepage increases, the traction force also increases. The maximum pressure obtained is 1232 MPa and 1229 MPa for the low and high adhesion, respectively.

Table 7-3 Tangential contact force between rail and wheel

Approaches	Traction force (kN)	
	Partial slips	Full slips
Polach	38.2	37.8
FEM	34.2	38.2
Deviation	10.7 %	1.2 %

b) The effect of creepage on traction force

The influence of creepage on traction forces was analyzed by Polach's approach and FE approach. For the wheel load of 85 kN and a rolling speed of 80 km/h, the relationship between traction force (or creep force) and creepage under dry contact ($\mu = 0.45$) is illustrated in Figure 7.20. It was also noticed that the FEM result was slightly lower than the Polach's result before the creepage reached the critical value.

When creepage was small, the traction force increased linearly with the creepage. Under dry rail-wheel contact conditions the critical traction force was 37.67 kN for a creepage of 1% (Figure 7.20).

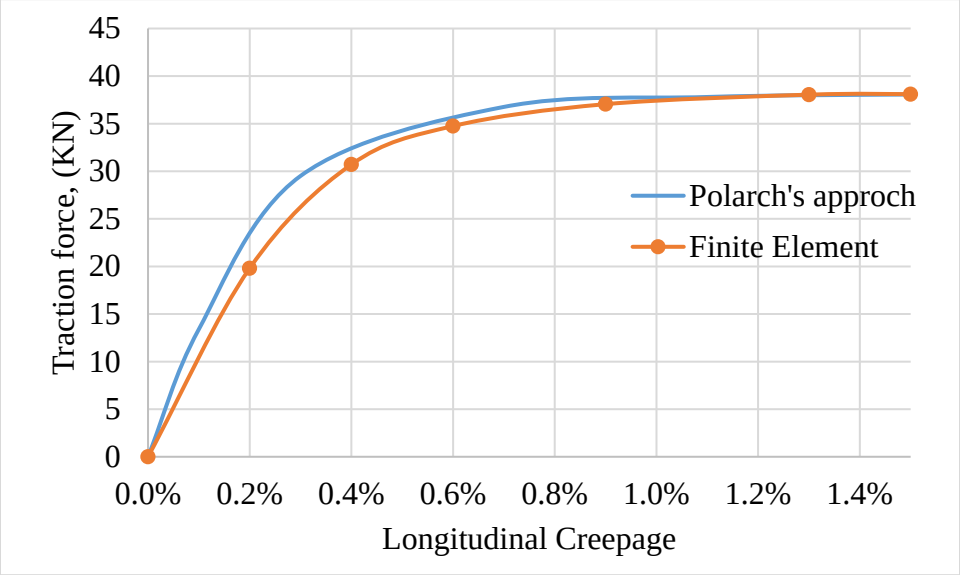

Figure 7.20 Traction curve for dry contact condition, (friction coefficient = 0.45, Fz = 85 kN)

In other words, full slip was obtained at this value of creepage. The curve of the coefficient of adhesion versus creepage for the same load condition is also shown in Figure 7.20. A maximum coefficient of adhesion of 0.45 at 1% creepage was obtained from a dry coefficient of friction of 0.45 in the FEM models and CONTACT models.

7.6 Crack Initiation Life

The mechanical properties used in fatigue calculations are presented in Table 7-4 (Ringsberg, 2001). Substituting these properties in Eq. (5.6) of the shear mode, the fatigue parameters vs number of cycles to crack initiation could be plotted, which is illustrated in Figure 7.21. The strain

and stress response of the rail wheel material from FEM are used to determine the magnitude of the three fatigue parameters used in this thesis (Jiang and Sehitoglu, Smith and co-worker, and Fatemi and Socie). After substituting the values of the stress and strain into their model, which was described in Section 5.3, the values of these fatigue model could be obtained. The values of these fatigue models are directly used to determine the number of cycles to crack initiation from the Figure 7.21. Therefore, the values of these fatigue parameters with respect to number of cycles to crack initiation is summarized in Table 7-5.

Table 7-4 Mechanical properties for the rail wheel steel

E (GPa)	v	σ_y (MPa)	b	c	ε_f' (%)	σ_f' (MPa)	ε_c	J
209.82	0.29	400.1	-0.089	-0.559	10.3	936	11.5	0.2

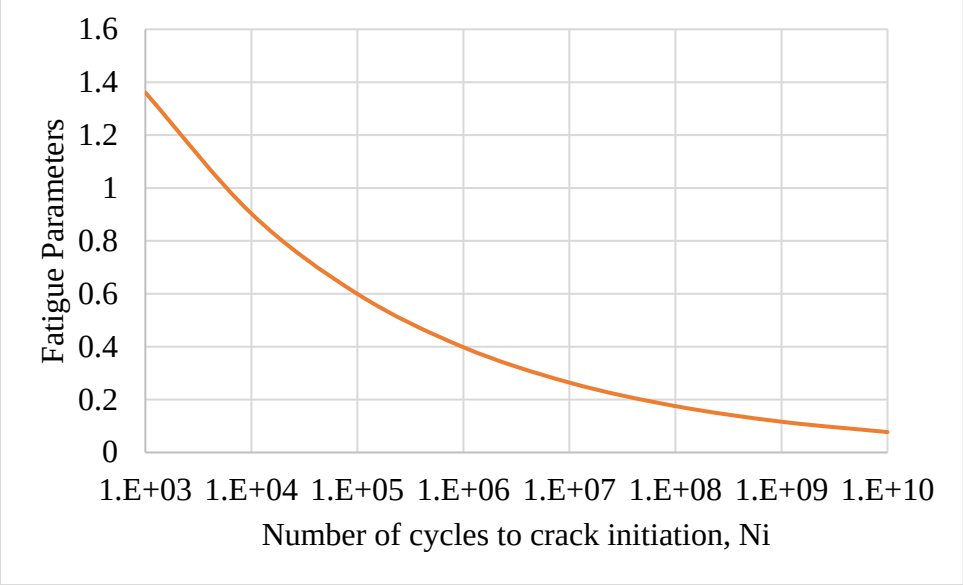

Figure 7.21 Fatigue crack initiation life Vs fatigue parameters

Table 7-5 Number of cycles to crack initiation (Ni) for different fatigue models

Fatigue Parameters	Maximum Damage Parameter	Ni
Jiang and Sehitoglu Model	0.6	1×10^5
Smith-Watson-Topper (SWT) model	0.54	5.78×10^5
Fatemi-Socie (FS) model	0.58	1.36 ×105

7.7 Effect of the loading on equivalent stress intensity factor

In order to investigate the effect of loading values on the mixed mode equivalent stress intensity factor, ΔK_{eq} ; 55kN, 70kN, 85 kN, 100 kN, 115 kN and 130 kN loads as well as 5 mm crack length are considered. Figure 7.22 shows the results of equivalent stress intensity factor versus loading values. The results show that stress intensity factor increases as the loading values increases.

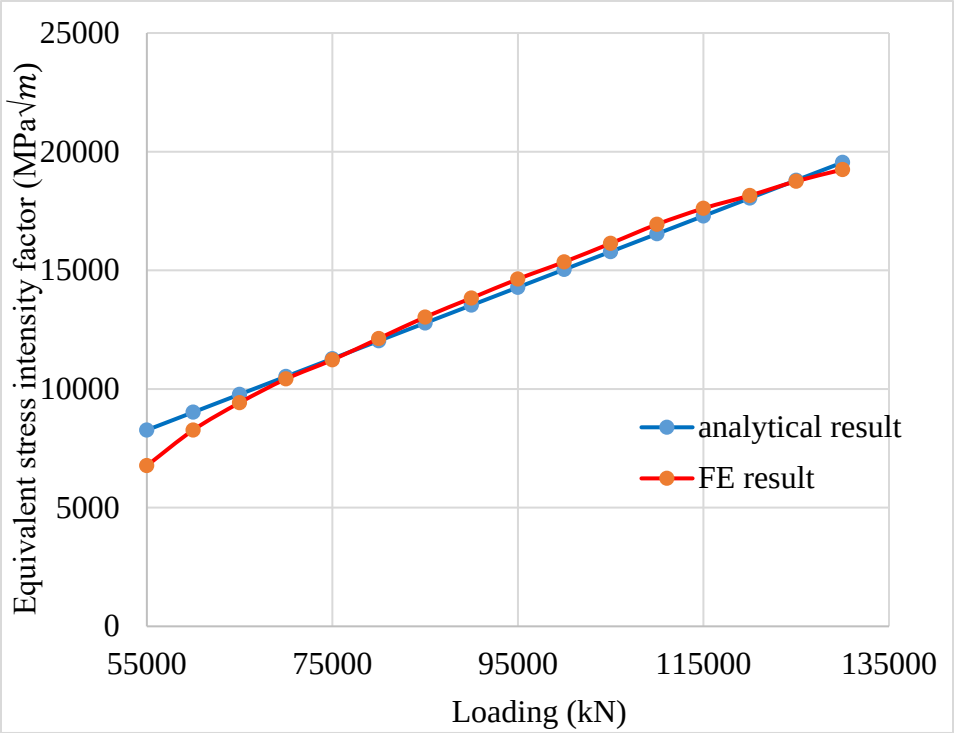

Figure 7.22 Equivalent stress intensity factor Vs different loading

7.8 The effect of the crack length on the stress intensity factors

In this section, the effects of different crack lengths are investigated. Figure 7.23 shows the effect of the crack length (0.01 mm to 5.1 mm with an increment of 0.5 mm) on stress intensity factors of mode I, mode II and mode III loading conditions, as well as on equivalent stress intensity factor from the analytical results. In this investigation, 85 kN was used as the maximum amount of the applied load on the wheel. For the applied load, stress intensity factors (KI, KII, KIII and ΔK_{eq}) increase as the crack length (a) increases. Figure 7.24 illustrates the equivalent stress intensity factor Vs crack length for both analytical (Eq. (5.8)-(5.10)) and FE analysis. The results from both analyses are almost agree to each other. The critical crack length obtained from the analytical and

FE analysis are 5.5 and 5.1 mm respectively. The deviation is around 7.8 %, which may be due to the geometric correction factor Y(a) which was ignored in analytical analysis.

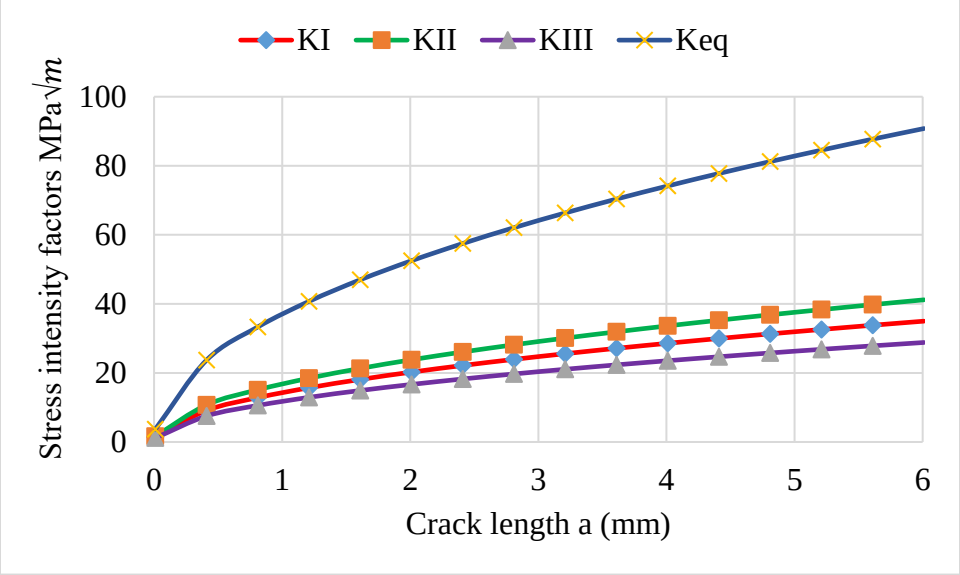

Figure 7.23 Crack length Vs stress intensity factors

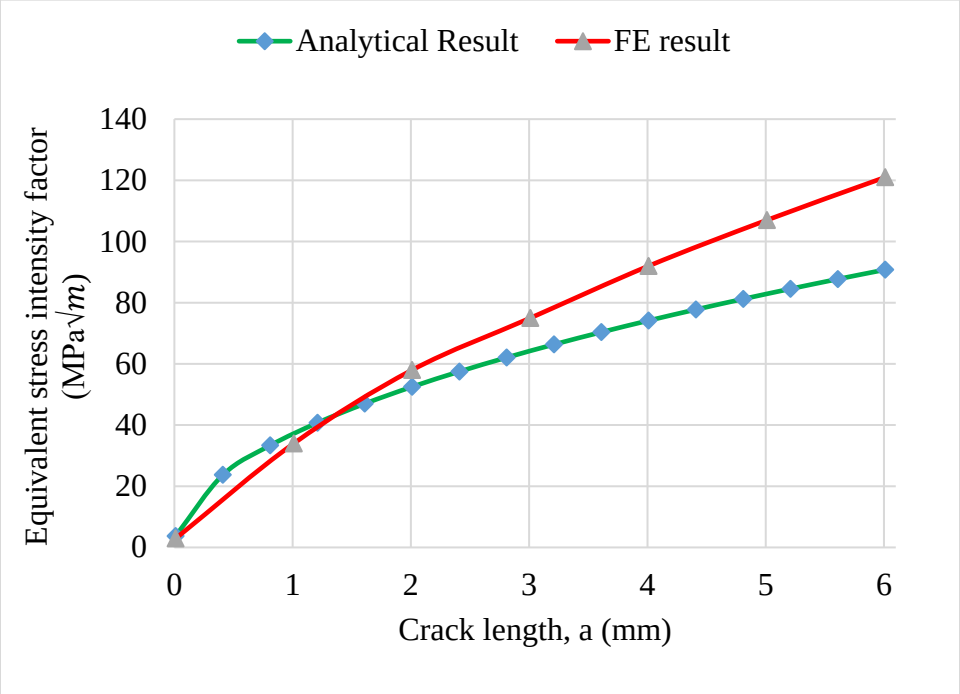

Figure 7.24 Crack length Vs equivalent stress intensity factor

7.9 Fatigue crack Propagation life

The crack propagation life was calculated by using both analytical and FE approaches. The crack length Vs Number of cycles is illustrated in Figure 7.25, which was plotted from Eq. (5.20). The critical crack length obtained from the analytical and FE result is 5.5 mm 5.1 mm respectively. The crack propagation life of the rail wheel was summarized in Table 7-6. However, this number of cycles are the life of the wheel from the initiated crack grow up to the critical length of the crack. After the critical length, the crack will propagate rapidly.

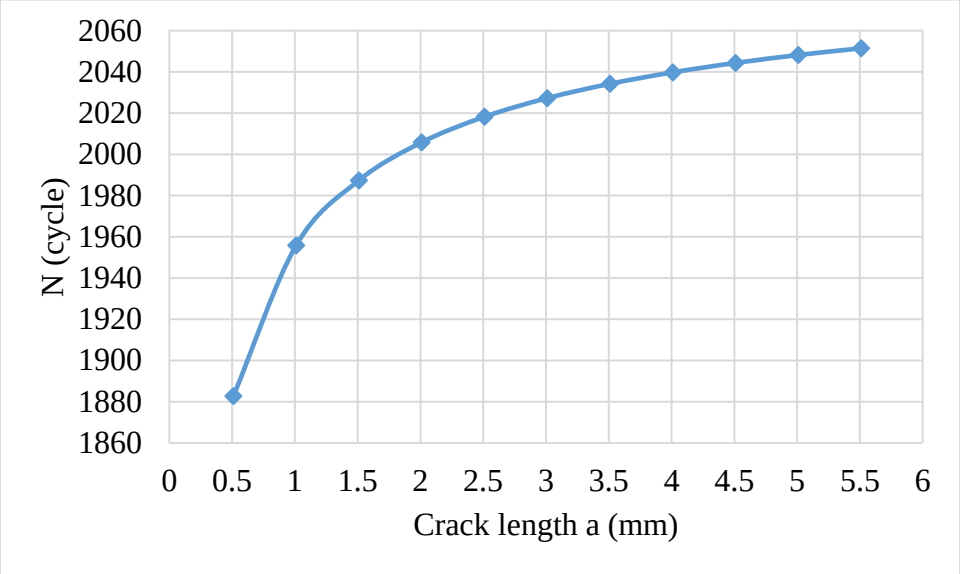

Figure 7.25 Fatigue life of the wheel

Table 7-6 Fatigue crack propagation life

	Analytical result	FE result
Critical crack length (a_{cr})	5.5 mm	3.8 mm
Fatigue life (Np)	2052	2020

CHAPTER 8

CONCLUSION AND SUGGESSTED FUTURE WORK

8.1 Conclusion

This thesis covers rolling contact modelling, cyclic plasticity modelling, crack initiation and propagation life of the rail-wheel. To cover all these mentioned topics, analytical and numerical approaches have been used.

The rail wheel contact problem has been investigated under two categories: 1) normal and 2) tangential contact problems. In normal contact problem; the normal pressure distribution, contact stresses, contact shape and size are determined. In tangential contact problem, creepages and creep forces are determined. In analytical approaches, Hertzian theory was used to determine these the normal contact parameters, and Kalker's and Polarch's model was used to analyze tangential contact problem. In numerical approaches, ABAQUS was used to analysis both normal and tangential contact problems. In order to reduce computation time, the sub-modelling system was used instead of full modelling. Additionally, to get more accurate results and reduce the computation time, fine mesh was applied to the parts of the rail-wheel near the contact, and course mesh was applied to other regions of the components.

In the rail wheel cyclic plasticity modelling, the constitutive model, which defines the stress-strain response of rail wheel material under cyclic load in mathematical ways, is discussed. From this equation the stress strain response of the rail wheel material can be easily understood depending on the amount of the axle load, which applied on the wheels.

In fatigue analysis, the life of the rail wheel was investigated under two categories: crack initiation life and propagation life. To determine the crack initiation life, two procedures have been used: the response quantities from the FE model such as stress and strain, and fatigue life models. In this study, three fatigue crack initiation models: 1, Sehitoglu and Jiang (Sehitoglu and Jiang, 1992), 2) Smith and co-workers (Smith et al., 1970), and 3) Fatemi and Socie (Fatemi and Socie, 1988)) have been used to determine the crack initiation life. In the same manner, the response from the FE model of the contact analysis is used as an input for determining the crack propagation life depending on the equivalent stress intensity factor. Liu and Mahadevan (Liu and Mahadevan, 2007) multiaxial fatigue model was used to determine the equivalent stress intensity factor, which used to determine the fatigue life of the rail wheel.

In other ways, the sub-surface cracking is modeled using 3D FEM and a mixed-mode crack model based on critical plane concepts. For computational efficiency, the finite element analysis is divided in to two stages: global model analysis and sub-model analysis. In the global model analysis, complete wheel geometry is considered and rolling contact analysis is performed. In the sub-model analysis, a small block with an embedded 3D fatigue crack is considered and elastic-plastic analysis is performed to estimate the uni-modal stress intensity factor ranges at the crack tip in ABAQUS XFEM. The results from the full model are applied as boundary conditions to the sub-model. A mixed-mode crack model based on critical plane concepts is used to compute the equivalent stress intensity factor range (ΔKeq) at the crack tip using the uni-modal values obtained from the finite element analysis. Finally, the life of the rail wheel was determined from the equivalent stress intensity factor range (ΔKeq), which was calculated from both analytical and FE results. The results obtained from the analytical and FE analysis agree to each other and the deviation is very small.

8.2 Future Work

In the present study, the rolling contact problem and fatigue behaviour of rail wheel are studied. The XFEM ABAQUS was used to study the subsurface crack propagation of the rail wheel. However, the current XFEM models doesn't recognize the situation that occurred before the crack nucleation. Only the rolling contact cycles from crack initiation to propagation was considered in the current XFEM ABAQUS model. The simulation could be done by considering the situation before the crack was initiated

Generally, anyone can consider the following suggestion for future work

- The work could be done by considering thermal stresses developed between rail and wheel
- The work could be done by changing the cross section of rail, wheel and contact length
- The residual stress could be considered
- Dynamic effect could be considered for the crack modelling.
- The work could be done by considering the effect of turning
- The work could be verified with the experimental results

REFERENCES

Alemi, A., Corman, F., Lodewijks, G., 2017. Condition monitoring approaches for the detection of railway wheel defects. Proceedings of the Institution of Mechanical Engineers, Part F: Journal of Rail and Rapid Transit 231, 961–981.

Athukorala, A.C., 2016. Investigation of Wear and Ratcheting Response of Head-Hardened Australian Rail Steel under Conditions of Rolling Contact Fatigue. Queensland University of Technology.

Athukoralaa, A.C., De. Pellegrin, D.V., Kourousis, K.I., 2017. A unified material model to predict ratcheting response in head-hardened rail steel due to non-uniform hardness distributions. Tribology International 111, 26–38.

Ayasse, J.-B., Chollet, H., 2006. Chapter 4 - Wheel–Rail Contact, in: Handbook of Railway Vehicle Dynamics. CRC Press LLC/Taylor & Francis, NW, Suite 300, Boca Raton, FL 33487, USA.

Barber, J., 2018a. Contact mechanics, solid mechanics and its applications. Springer, New York. ISBN.

Barber, J., 2018b. Contact mechanics, solid mechanics and its applications. Springer, New York. ISBN.

Barros, C.B. de, 2018. Fatigue and cyclic plasticity of 304L stainless steel under axial, torsional and proportional axial-torsional loading.

Basan, R., 2016. CONSTITUTIVE MODELING AND MATERIAL BEHAVIOR. UNIVERSITY OF RIJEKA, RIJEKA.

Bayissa, W., Dhanasekar, M., 2011. High-Speed Detection of Broken Rails, Rail Cracks and Surface Faults. CRC for Rail Innovation, Brisbane, Australia, Project 116.

Behravesh, S.B., 2013. Fatigue Characterization and Cyclic Plasticity Modeling of Magnesium Spot-Welds. University of Waterloo.

Bosso, N., Spiryagin, M., Gugliotta, A., Somà, A., 2013. Review of Wheel-Rail Contact Models, in: Mechatronic Modeling of Real-Time Wheel-Rail Contact. Springer Berlin Heidelberg, Berlin, Heidelberg, pp. 5–19. https://doi.org/10.1007/978-3-642-36246-0_2

Brown, M.W., Miller, K., 1973. A theory for fatigue failure under multiaxial stress-strain conditions. Proceedings of the Institution of Mechanical Engineers 187, 745–755.

Burgelman, N., 2016. The Wheel-Rail Contact Problem in Vehicle Dynamic Simulation: Modeling of Train-Turnout Interaction. Chalmers University of Technology, Sweden.

Chaboche, J.-L., 1991. On some modifications of kinematic hardening to improve the description of ratchetting effects. International journal of plasticity 7, 661–678.

Chu, C.-C., 1995. Fatigue damage calculation using the critical plane approach. Journal of Engineering Materials and Technology 117, 41–49.

Clayton, P., 1996. Tribological aspects of wheel-rail contact: a review of recent experimental research. Wear 191, 170–183.

Cvetkovski, K., 2012. Influence of thermal loading on mechanical properties of railway wheel steels. CHALMERS UNIVERSITY OF TECHNOLOGY, Gothenburg, Sweden.

Daves, W., Fischer, F.D., 2002. Modelling of the plastification near the rough surface of a rail by the wheel–rail contact. Wear 253, 241–246.

Divya Bharathi, K., 2015. Fatigue-Ratcheting Interaction Behavior of AISI 4340 Steel (PhD Thesis).

Dunne, F., Petrinic, N., 2005. Introduction to Computational Plasticity. Oxford Univesity Press.
Ekberg, A., 2000. Rolling contact fatigue of railway wheels: towards tread life prediction through numerical modelling considering material imperfections, probabilistic loading and operational data, Doktorsavhandlingar vid Chalmers Tekniska Högskola. Chalmers Univ. of Technology, Göteborg.
Ekberg, A., Sotkovszki, P., 2001. Anisotropy and rolling contact fatigue of railway wheels. International Journal of Fatigue 23, 29–43.
El Haddad, M.H., Topper, T.H., Smith, K.N., 1979. Prediction of non propagating cracks. Engineering fracture mechanics 11, 573–584.
El-sayed, H.M., Lotfy, M., Zohny, H.E., Riad, H.S., 2017. Prediction of fatigue crack initiation life in railheads using finite element analysis. Ain Shams Engineering Journal.
Everaerts, J., 2017. Fatigue Crack Initiation and Facet Formation in Ti-6Al-4V Wires.
Facheris, G., 2014. Cyclic plastic material behavior leading to crack initiation in stainless steel under complex fatigue loading conditions (PhD Thesis). ETH Zurich.
Fajdiga, G., Sraml, M., 2009. Fatigue crack initiation and propagation under cyclic contact loading. Engineering Fracture Mechanics 76, 1320–1335.
Fatemi, A., Socie, D.F., 1988. A critical plane approach to multiaxial fatigue damage including out-of-phase loading. Fatigue & Fracture of Engineering Materials & Structures 11, 149–165.
Forman, R.G., Kearney, V., Engle, R., 1967. Numerical analysis of crack propagation in cyclic-loaded structures. Journal of basic Engineering 89, 459–463.
Guagliano, M., Vergani, L., 2005. Experimental and numerical analysis of sub-surface cracks in railway wheels. Engineering fracture Mechanics 72, 255–269.
Haidari, A., Heidari, M., 2017. Study of Surface Crack Growth in Railway Wheels With Fairly Small Plasticity. AJER 6, 97–105.
Haidari, A., Heidari, M., 2017. Study of Surface Crack Growth in Railway Wheels With Fairly Small Plasticity. American Journal of Engineering Research (AJER) 6, 97–105.
Haidari, A., Tehrani, P.H., 2015. Thermal load effects on fatigue life of a cracked railway wheel. Latin American Journal of Solids and Structures 12, 1144–1157.
Halama, R., Sedlák, J., Šofer, M., 2012. Phenomenological modelling of cyclic plasticity, in: Numerical Modelling. InTech.
Ivan Y., S., 2008. Wheel/Rail Interface Optimisation. Dnipropetrovsk State University, Netherlands.
Jerome Pun, C.L., 2014. Plastic Deformation Behaviour of High Strength Rail Steels in Heavy Haul Railway Systems. Monash University, Clayton, Australia.
Johnson, K., 1974. Contact mechanics, 1985. Cambridge University Press, Cambridge.
Kalker, J.J., 1990. Three-Dimensional Elastic Bodies in Rolling Contact.
Kang, G., Gao, Q., 2002. Uniaxial and non-proportionally multiaxial ratcheting of U71Mn rail steel: experiments and simulations. Mechanics of Materials 34, 809–820.
Kang, G., Kan, Q., 2017. Cyclic Plasticity of Engineering Materials : Experiments and Models. John Wiley & Sons Ltd, China.
Keylin, A., 2012. Analytical Evaluation of the Accuracy of Roller Rig Data for Studying Creepage in Rail Vehicles. Pittsburgh, Blacksburg, VA.
Khoa Duy, V., 2015. Damage analysis of wheel/rail contact associated to high adhesion condition. University of Wollongong.

Kim, J.-K., Kim, C.-S., 2002. Fatigue crack growth behavior of rail steel under mode I and mixed mode loadings. Materials Science and Engineering: A 338, 191–201.
Kotoula, M., 2015. Crack path modelling in railway wheel under rolling contact fatigue. Applied and Computational Mechanics 9, 103–126.
Lewis, R., 2009. Basic tribology of the wheel-rail contact, in: Wheel-Rail Interface Handbook. Woodhead Publishing Limited.
Lewis, R., Olofsson, U., 2009a. Basic tribology of the wheel–rail contact, in: Wheel–Rail Interface Handbook. Elsevier, pp. 34–57.
Lewis, R., Olofsson, U., 2009b. Wheel-rail interface handbook. Woodhead Publishing Limited.
Liu, Y., Liu, L., Mahadevan, S., 2007. Analysis of subsurface crack propagation under rolling contact loading in railroad wheels using FEM. Engineering fracture mechanics 74, 2659–2674.
Liu, Y., Mahadevan, S., 2007. Threshold stress intensity factor and crack growth rate prediction under mixed-mode loading. Engineering fracture mechanics 74, 332–345.
Liu, Y., Stratman, B., Mahadevan, S., 2006. Fatigue crack initiation life prediction of railroad wheels. International journal of fatigue 28, 747–756.
Ma, Y., Markine, V., 2015. A numerical procedure for analysis of w/r contact using explicit finite element methods, in: CM2015: 10th International Conference on Contact Mechanics, Colorado Springs, USA, 30 August-3 September 2015.
Moës, N., Dolbow, J., Belytschko, T., 1999. A finite element method for crack growth without remeshing. International journal for numerical methods in engineering 46, 131–150.
Munidasa, W., Pathiranage, I., Udara, W., 2013. INVESTIGATION OF SURFACE RATCHETTING DUE TO RAIL/WHEEL CONTACT. Queensland University of Technology.
Orvnäs, A., 2005. Simulation of rail wear on the swedish light rail line Tvärbanan.
Özdemir, Y., 2016. Analysis of Normal and Tangential Wheel-Rail Contact Problem with Nonlinear Material Behaviour. University of Pardubice.
Paris, P.C., 1961. A rational analytic theory of fatigue. The trend in engineering 13, 9.
Patel, S., Kumar, V., Nareliya, R., 2013. Fatigue analysis of rail joint using finite element method. IJRET 02, 80–84.
Peng, D., Jones, R., 2013. Finite Element Method Study on the Squats Growth Simulation. Applied Mathematics 04, 29–38. https://doi.org/10.4236/am.2013.45A004
Polach, O., 1999. A fast wheel-rail forces calculation computer code. Vehicle System Dynamics 33, 728–739.
Prager, W., 1956. A new methods of analyzing stresses and strains in work hardening plastic solids. J. Appl. Mech.(ASME) 23, 493–496.
Pun, C.L.J., 2014. Plastic Deformation Behaviour of High Strength Rail Steels in Heavy Haul Railway Systems (PhD Thesis). Monash University.
Ramazan, Ö., 2017. Numerical and Theoretical Investigation of Wheel-Rail Contact. SJIF 4, 1204–1209.
Ringsberg, J., 2000. Cyclic ratchetting and failure of a pearlitic rail steel. Fatigue & Fracture of Engineering Materials & Structures 23, 747–758.
Ringsberg, J.W., 2001. Life prediction of rolling contact fatigue crack initiation. International Journal of Fatigue 23, 575–586.

Roundi, W., Gharad, A.E., 2014. Fatigue Behavior and Damage Modeling Of Train Wheels in Different Cases Of Loading. International Journal of Scientific & Technology Research 3, 296–301.
Schleinzer, G., Fischer, F., 2001. Residual stress formation during the roller straightening of railway rails. International Journal of Mechanical Sciences 43, 2281–2295.
Sehitoglu, H., Jiang, Y., 1992. Fatigue and stress analyses of rolling contact. College of Engineering, University of Illinois at Urbana-Champaign, Technical Report 161.
Shabana, A.A., Zaazaa, K.E., Sugiyama, H., 2007. Railroad vehicle dynamics: a computational approach. CRC press.
Shackleton, P.A., 2009. An Optimised Wheel-Rail Contact Model for Vehicle Dynamics Simulation. Manchester Metropolitan University.
Shahzamanian Sichani, M., 2016. On Efficient Modelling of Wheel-Rail Contact in Vehicle Dynamics Simulation. KTH Royal Institute of Technology, Stockholm.
Shantz, C.R., 2010. Uncertainty quantification in crack growth modeling under multi-axial variable amplitude loading (PhD Thesis). Vanderbilt University.
Shevtsov, I., 2008. Wheel/rail interface optimisation (PhD Thesis). TU Delft, Delft University of Technology.
Sladkowski, A., Sitarz, M., 2005. Analysis of wheel–rail interaction using FE software. Wear 258, 1217–1223.
Smith, Kn., Watson, P., Topper, T., 1970. â A Stress-Strain Function for the Fatigue of Metals, â J. Mater 5, 767â–778.
Srivastava, J.P., Sarkar, P.K., Meesala, V., Ranjan, V., 2017. Rolling Contact Fatigue Life of Rail for Different Slip Conditions. Latin American Journal of Solids and Structures 14, 2243–2264.
Srivastava, J.P., Sarkar, P.K., Ranjan, V., 2014. Contact Stress Analysis in Wheel–Rail by Hertzian Method and Finite Element Method. J. Inst. Eng. India Ser. C, Journal of The Institution of Engineers (India): Series C.
Sura, V., 2011. Failure modeling and life prediction of railroad wheels. Vanderbilt University, Tennessee.
Systèmes, D., 2007. Abaqus analysis user's manual. Simulia Corp. Providence, RI, USA.
Tangtragulwong, P., 2012. Optimal railroad rail grinding for fatigue mitigation (PhD Thesis). Texas A & M University.
Tao, G., Wen, Z., Zhao, X., Jin, X., 2016. Effects of wheel–rail contact modelling on wheel wear simulation. Wear 146–156.
Telliskivi, T., Olofsson, U., 2004. Wheel–rail wear simulation. Wear 257, 1145–1153. https://doi.org/10.1016/j.wear.2004.07.017
Tresca, H., 1869. Mémoires sur l'écoulement des corps solides. Imprimerie impériale.
Ulrich, S., 2016. Reduction of rolling contact fatigue through the control of the wheel wear shape. University of Pretoria, Pretoria.
Verma, P., 2011. Ratcheting Fatigue Behaviour and Post-fatigue Tensile Properties of Commercial Aluminium. National Institute of Technology, Rourkela.
Vo, K.D., 2015. Damage analysis of wheel/rail contact associated to high adhesion condition.
Von Mises, R., 1913. Mechanik der Festen Körper im Plastisch Deformablen Zustand. Nachr. Math. Phys 1, 582–592.

Walker, K., 1970. The effect of stress ratio during crack propagation and fatigue for 2024-T3 and 7075-T6 aluminum, in: Effects of Environment and Complex Load History on Fatigue Life. ASTM International.

Wirtu, Bayissa, L., Dhanaseka, M., 2011. High speed detection of broken rails, rail cracks and surface faults.

Yan, W., Fischer, F., 2000. Applicability of the Hertz contact theory to rail-wheel contact problems. Archive of applied mechanics 70, 255–268.

APPENDEX

A) **UIC 60 Rail Profile**

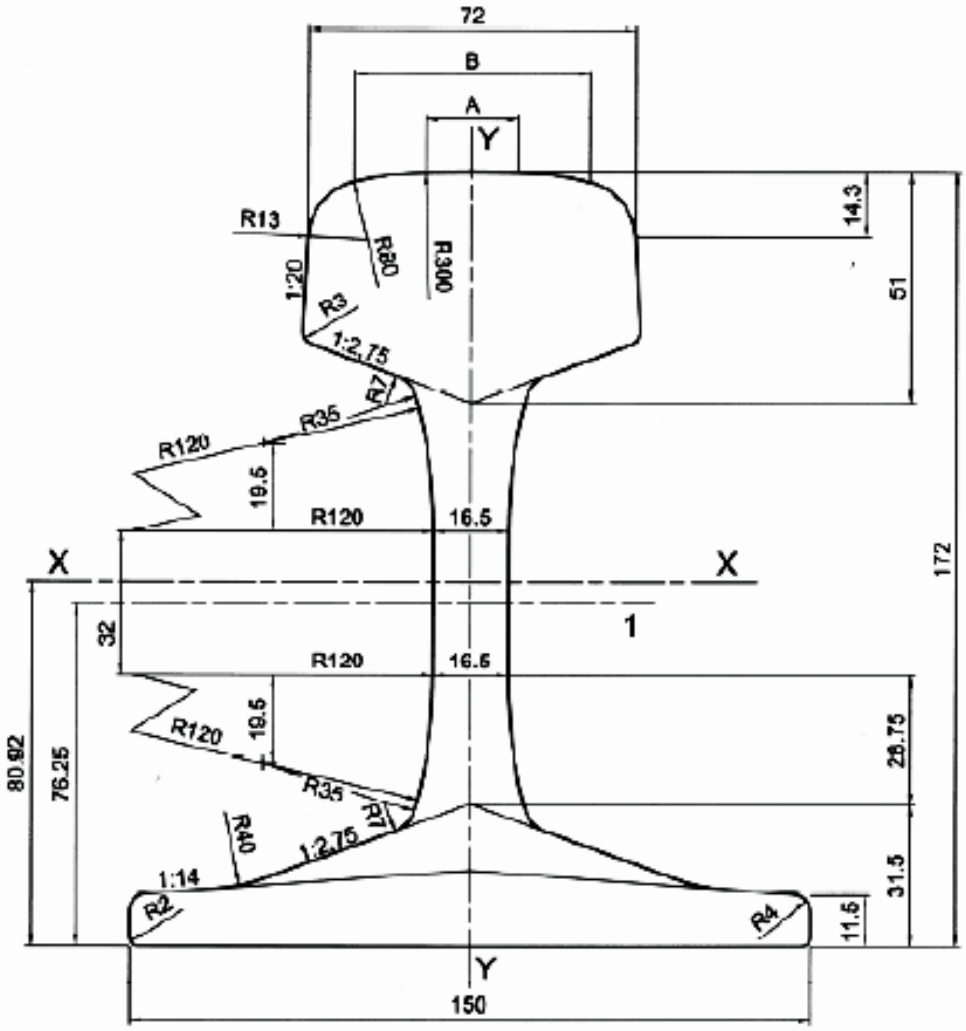

Key

1 centre line of branding

cross-sectional area	:	76,70	cm^2
mass per metre	:	60,21	kg/m
moment of inertia x-x axis	:	3 038,3	cm^4
section modulus - Head	:	333,6	cm^3
section modulus - Base	:	375,5	cm^3
moment of inertia y-y axis	:	512,3	cm^4
section modulus y-y axis	:	68,3	cm^3

B) UIC S1002 Wheel Profile

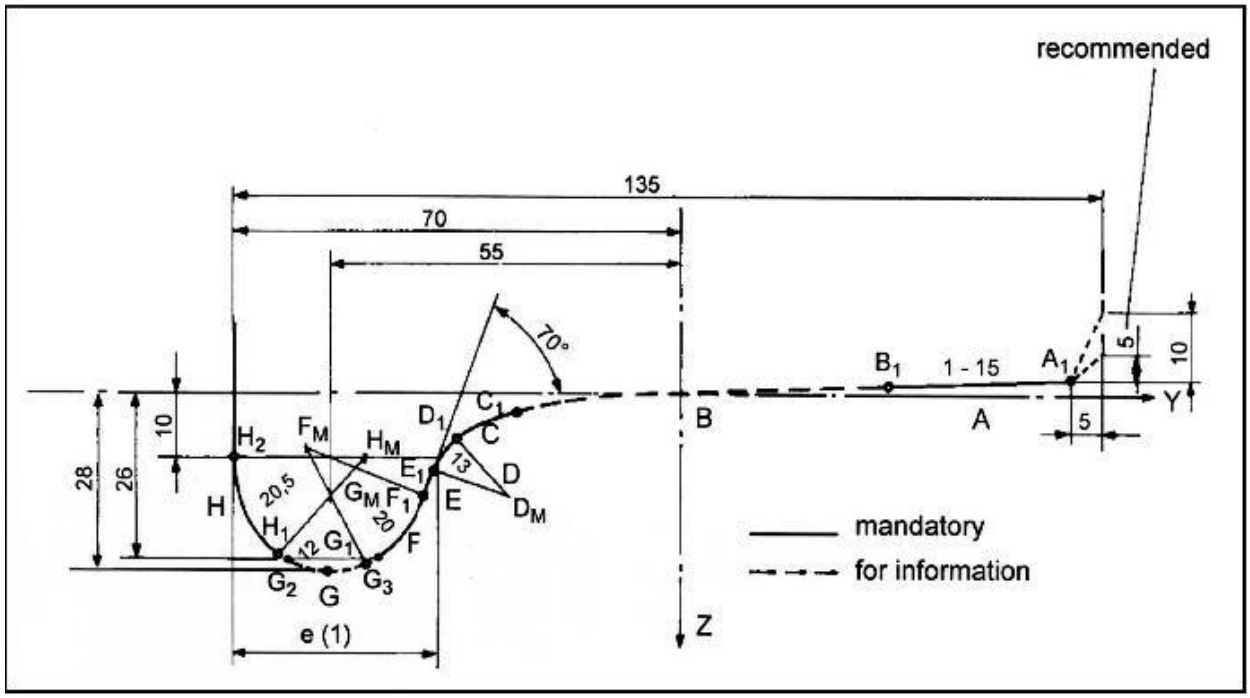

C) Crack length Vs Number of cycles for wheel

a_i	Δa	a_f	ΔN	N
0.01	0.5	0.51	1882.72	1882.72
0.51	0.5	1.01	73.13	1955.85
1.01	0.5	1.51	31.5291	1987.38
1.51	0.5	2.01	18.4363	2005.82
2.01	0.5	2.51	12.3955	2018.21
2.51	0.5	3.01	9.03965	2027.25
3.01	0.5	3.51	6.95402	2034.21
3.51	0.5	4.01	5.55602	2039.76
4.01	0.5	4.51	4.56633	2044.33
4.51	0.5	5.01	3.8361	2048.17
5.01	0.5	5.51	3.27954	2051.45